HOKKAIDO UNIVERSITY

Title	Application of X-ray CT to the study of microstructure and diffusivity in cementitious materials
Author(s)	Darma, Ivan Sandi
Citation	. ( ) 11452
Issue Date	2014-03-25
DOI	10.14943/doctoral.k11452
Doc URL	http://hdl.handle.net/2115/55523
Type	theses (doctoral)
File Information	Ivan_Sandi_Darma.pdf

Instructions for use

APPLICATION OF X-RAY CT TO THE STUDY OF MICROSTRUCTURE AND DIFFUSIVITY IN CEMENTITIOUS MATERIALS

X 線 CT を用いたセメント硬化体の微細構造と拡散性状に関する研究

Ivan Sandi Darma

DIVISON OF FIELD ENGINEERING FOR THE ENVIRONMENT

GRADUATE SCHOOL OF ENGINEERING

HOKKAIDO UNIVERSITY

March, 2014

APPLICATION OF X-RAY CT TO THE STUDY OF MICROSTRUCTURE AND DIFFUSIVITY IN CEMENTITIOUS MATERIALS

X 線 CT を用いたセメント硬化体の微細構造と拡散性状に関する研究

Ivan Sandi Darma

A THESIS SUBMITTED IN PARTIAL FULFILLMENT OF THE REQUIREMENTS
FOR THE DEGREE OF DOCTOR OF PHILOSOPHY

Examination Committee
Prof. Takafumi Sugiyama
Prof. Tamon Ueda
Prof. Toyoharu Nawa

DIVISON OF FIELD ENGINEERING FOR THE ENVIRONMENT
GRADUATE SCHOOL OF ENGINEERING
HOKKAIDO UNIVERSITY
March, 2014

ABSTRACT

At the beginning of its development, the X-ray CT technique originally was developed for medical analysis. However, along with the advances in technology, the ability of X-ray CT continues to increase. Therefore, the use of X-ray CT is no longer intended for medical application but has expanded to other fields such as civil engineering especially for material science. Related to construction materials, there are many experimental methods that can be used to study the microstructure of cementitious materials such as scanning electron microscope (SEM), backscattered electron (BSE), mercury intrusion porosimetry (MIP) and permeability test. However, each of those experimental methods generally only provides a few aspects related to the microstructure of cementitious materials. On the other hand, there are many aspects which can be obtained from the microstructure of cementitious materials just through the use of X-ray CT technique. This present study describes the versatility of the application of X-ray CT technique to study the microstructure and diffusivity of cementitious materials. In this research, there are two types of X-ray CT systems used to acquire the 3D image of the internal structure of cementitious materials i.e. synchrotron X-ray CT with spatial resolution of 0.5 μm and micro-focus X-ray CT with lower resolution (>10 μm/pixel).

The first and arguably the most important in the use of X-ray CT is the observation of the three-dimensional pore structure of the hardened cementitious materials. The application of X-ray CT certainly can be expanded through the use of different types of cementitious materials as well as its curing period. In this case, cement paste specimen mixed with silica fume and fly ash (low alkali binder) was used and Ordinary Portland Cement (OPC) cement paste was prepared as a comparison. The pore structure parameters such ash total porosity, connectivity, and pore size distribution were obtained through the analysis of 3D microtomographic images. Furthermore, Random Walk Simulation (RWS) was performed to quantify the diffusion tortuosity in the pore structure. It is found that the diffusion tortuosity of percolated porosity of OPC cement paste was higher than that of low alkali cement paste at the same curing periods.

On the other hand, despite having a lower resolution, the use of micro-focus X-ray CT was intended to identify the larger void space in cementitious materials such as cracks and air voids and also allows us to use the specimens with larger size. Micro-focus X-ray CT was employed to observe cracked mortar specimens due to mechanical loading. The cracks in beam specimens of the size of 10 x 20 x 60 mm and cylinder specimens of the size of 20 mm in diameter and 40 mm in height were induced by flexural test and splitting tensile test, respectively. Subsequently, the 3D crack geometry was obtained from microtomographic images. Through the analysis of 3D crack geometry, the crack geometry parameters such as tortuosity and constrictivity were obtained. The tortuosity of flexural crack and splitting tensile crack in the mortar specimen with maximum size of aggregate of 1.7 mm were found to be around 1.13 and 1.25, respectively, and it was independent to the crack opening width and whether fly ash was added or not. Meanwhile, it is found that the type of cracks and the presence of void play an important role on the constrictivity of the crack. The constrictivity increased for fly ash mortar having roughly the equivalent crack opening width of OPC mortar.

The scope of the observation using X-ray CT was expanded even further. The application of micro-focus X-ray CT coupled with in-situ tracer diffusion test was conducted to clarify the transport mechanism in cracked mortar specimens. Diffusivity in the crack was controlled by following factors: the crack opening width, as well as, by its constrictivity. The diffusive transport was also restricted due to the presence of air pockets in the crack. In this regard, a diffusion-accessible path factor was proposed to account for the degree of water

saturation within the crack space. In addition, it was confirmed that the addition of fly ash could reduce the diffusivity through the uncracked body as compared with normal OPC mortar of equivalent diffusion coefficient along the crack.

Furthermore, the variations in cementitious materials were added. In this regard, deteriorated specimens were used in X-ray CT observation. There were three types of deterioration applied in the specimen namely leaching, mechanical loading and high temperature exposure followed by re-curing. X-ray CT technique was used to observe the change in microstructure in cementitious materials as the effect of deterioration. As for leaching, after the observation using synchrotron X-ray CT and image analysis, the total porosity and percolated porosity of normal cement paste specimen significantly increased after leaching test as compared to that of cement paste specimen with low alkali binder. Dissolution of hydration product in normal cement paste specimen dramatically reduced the diffusion tortuosity in the percolated porosity of normal cement paste specimen. On the other hand, although there was a reduction in the diffusion tortuosity for percolated porosity of cement paste specimen with low alkali binder, however, it was not dramatically when compared with that of normal cement paste specimen.

In the study of deteriorated cementitious materials due to mechanical loading, synchrotron X-ray CT was combined with micro-tensile instrument and the observation during the application of load was conducted in-situ inside synchrotron X-ray CT chamber. Although there was no definite result of this experiment, however, by improving the quality both sample preparation and loading instrument, the behavior of microstructure under external load can be observed through the application of synchrotron X-ray CT combined with other mechanical tests.

Using micro-focus X-ray CT, concrete specimen in three different conditions, namely before heating, after heating and re-curing was examined. It was observed that cracks occurred in the concrete specimen due to heating can be categorized into three types of cracks, namely interfacial cracks between mortar and coarse aggregates, bridging cracks between aggregates and bridging cracks between aggregates and air voids. Therefore, the volume of total and percolated porosity of heated specimen increased due to the presence of these cracks. Furthermore, we observed that water re-curing is more effective in the recovery of microstructure of concrete after high temperature exposure as compared with that of air re-curing.

Through the application of X-ray CT technique this research could provide better understanding of the microstructure change in cementitious materials. In addition, with the proposed X-ray CT technique coupled with in-situ tracer diffusion test, the transport mechanism of diffusion inside crack and through the uncracked matrix would be further understood. Therefore, this research can contribute to the clarification of durability aspect and to more accurate prediction of service life for concrete structures.

Dedication

To my beloved family

Acknowledgement

Table of Contents

List of Figures

Listof Tables

CHAPTER 1
INTRODUCTION

1.1. GENERAL

X-ray CT, at the beginning of its development, X-ray CT technique originally was developed for medical analysis. The first X-ray CT scanner was developed in England by Sir Godfrey Hounsfiled. This X-ray CT was used to scan human brains with a maximum resolution of 80×80 pixels [1]. In this regard, X-ray CT is the first imaging modality that allows accurate non-destructive interior image reconstruction of an object from a sufficient number of X-ray projections. Hounsfield's X-ray CT prototype immediately generated a tremendous excitement in the medical community and inspired a rapid technical development with an ever strong momentum. Also, X-ray CT as the first trans-axial tomography model promoted the development of other tomographic modalities for biomedical applications and beyond, such as magnetic resonance imaging, ultrasound tomography, nuclear tomography, optical tomography, molecular tomography, and so on [2].

Then, this technique is attracting increasing interest for its applicability as a tool in non-destructive testing in engineering especially for non-living specimens such as cementitious materials. Morgan et al [3] was one of the first used of CT for the evaluation of concrete by using X-ray CT technique even though it was limited to only visual inspection. However, it has opened our eyes that the X-ray CT can be used not only in the medical field but can also be used in other fields such as civil engineering.

Along with the advances in technology, the ability of X-ray CT continues to increase. The X-ray CT can be used not only for visual inspection but also to observe more details in the three-dimensional microstructure of cementitious materials. In general, there are two type of X-ray CT system used in the microstructure observation of cementitious materials. The first is synchrotron X-ray CT and the second is micro-focus X-ray CT. Synchrotron X-ray CT has already been applied by various researchers to study the microstructure as well as its evolution with increasing age of cementitious materials [4-11]. Synchrotron X-ray CT also has been employed to characterize the microstructure in deteriorated cementitious material such as leaching [12,13]. Based on those literatures, considering all the specimens used in the experiment using synchrotron X-ray CT were cement pastes, it can be said that the synchrotron X-ray generally used to study microstructure of cementitious materials at cement paste level due to higher resolution.

Meanwhile, although the micro-focus X-ray CT has a lower resolution than that of synchrotron X-ray CT, however, the use of micro-focus X-ray CT was intended to identify the larger void space in concrete specimens such as cracks and air voids and also allows us to use the specimens with higher level such as mortar and concrete. Using micro-focus X-ray CT system, Naik et al [14] monitored the sulfate attack in the concrete specimens. Furthermore, Micro-focus X-ray CT system has been used by Elaqra et al [15] to observe the damage evolution in mortar during compressive loading. Recently, Promentilla and Sugiyama [16] characterized the internal structure of mortars that were exposed to freezing-thawing action by using micro-focus X-ray CT in Hokkaido University, Japan. Kikkawa et al [17] also used this X-ray CT to visualize three-dimensional image of flexural cracks in mortar beam with size of $10 \times 20 \times 60$ mm. Based on the explanation above, now we already have an overview of the ability of X-ray CT technique in the study of the internal structure of the cementitious material. However, still there are many things that are able to be explored in microstructure of cementitious materials through the application of X-ray CT as compared with other conventional techniques.

1.2. LITERATURE REVIEW
1.2.1. Microstructure of hydrated cement system

At a microscopic level, the complexities of concrete microstructure are evident. This is because it is neither homogeneously distributed with respect to each phase present in the structure nor they themselves homogeneous. In order to develop new cementitious materials the roles of each different phase present in the microstructure of concrete subjected to either external or internal forces must be clarified. However, without quantitative evaluation with respect of volume and area fraction of each phase at a microscopic level the behavior of concrete under study is hardly discussed in details.

In general there are four principal solid phases in the hydrated cement paste. They are calcium silicate hydrated (C-S-H), calcium hydroxide (CH), calcium sulfoaluminates hydrates, and unhydrated clinker grains. Calcium silicate hydrated (C-S-H) makes up 50 to 60 percent of the volume of solids in a hydrated Portland cement paste and is, therefore, the most important phase determining the properties of the paste [18]. The morphology of C-H-S also varies from poorly crystalline fibers to reticular network and it was assumed to resemble the natural mineral of tobermorite and that is why C-S-H sometimes called tobermorite gel [18].

Calcium hydroxide crystals (Portlandite) constitute 20 to 25 percent of the volume of solids [18]. It tends to form large crystals with distinctive hexagonal-prism morphology. The morphology usually varies from nondescript to stacks of large plates. Compared with C-S-H, the strength-contribution potential of calcium hydroxide is limited as a result of considerably lower surface area. Calcium sulfoaluminates hydrates occupy 15 to 20 percent of the solid volume in the hydrated paste and, therefore, play only a minor role in the microstructure-property relationship [18]. Depending on the particle size distribution of the anhydrous cement and degree of hydration, some unhydrated clinker grains may be found in the microstructure of hydrated cement pastes, even long after hydration process [18].

The scanning electron microscope (SEM) is one of instruments available for the examination and analysis of the microstructural characteristics of the solid objects. The primary reason for the SEM's usefulness is the high resolution than can be obtained when the objects are examined. SEM has been employed to investigate both fractured and polished surface of cementitious materials, allowing individual phases within hydrated cement to be identified [19-24]. Until now, SEM technique is still employed to study microstructure of concrete and even with various inclusions therein. However, the use of SEM is only intended to identify solid phases present in the microstructure of concrete, it cannot be used to determine the quantity of each phase. In fact, the percentage (fraction) of each phase contributed to the characteristic of the concrete. In this regard, backscattered electron (BSE) imaging was developed to overcome the said shortcoming of SEM technique.

During the last 20 years, backscattered electron imaging of polished surfaces has become well established as a method for the study of cement and concrete microstructures. The technique has many advantages, including the visualization of representative cross-sections over a wide range of magnifications and reproducible contrast dependent on atomic number. Scrivener and Pratt [25] processed BSE images of polished section to analyze the distribution of phases. Anhydrous phase, calcium hydroxide, calcium silicate hydrate, and porosity were differentiated on the basis of grey level. Kjellsen et al [26] used BSE imaging to quantify phase distribution as a function of curing temperature. Nevertheless the limitations of observing a two-dimensional section of a three-dimensional structure must be borne in mind. One way to overcome these limitations is to use X-ray microtomography to examine directly the three-dimensional internal microstructure of the material in a non-invasive manner without requiring any specimen preparation typical of the other mentioned experimental techniques. Image analysis technique coupled with analysis of linear attenuation coefficient (LAC) has proven to be able to identify and analyze each phase present in the

materials as well as its volume fraction [27].

1.2.2. Pore structure

Porosity is arguably the most important component of microstructure of cementitious material that affects important engineering properties such as strength and permeability. It is known that total porosity has a strong link to strength, shrinkage, elastic modulus, and toughness. The structure of porosity is also important. It is playing a fundamental role in governing transport process that influences the durability-based performance of these materials [28,29]. For example, the pore connectivity and the tortuosity of pore space are important variables to understand and model the diffusion whereby aggressive species (e.g., chlorides, sulfates, etc).

There are a number of tools that have been applied to the problem of microstructural characterization with respect to pore structure, but most of our information comes from three methods: mercury intrusion porosimetry (MIP), nitrogen adsorption/desorption (NAD), and scanning electron microscopy (SEM).

SEM is capable of observing the microstructural scale that includes the capillary porosity. In conjunction with a backscatter electron (BSE) detector, the chemical composition of microstructural is represented in the images by gray level variation. Pores appear very dark, which allow them to be distinguished and quantified by image analysis of the 2-D section [30]. However, SEM can only provide two-dimensional information. Information about 3-D pore network or connectivity cannot be directly observed.

The MIP measurement remains still the preferred method for pore structure evaluation due to its large range of pore size measurement and easy operation [31], although the measurement loses its accuracy for "ink-bottle" pores and fractures can be possibly induced in samples under high intrusion pressure [32-34]. In addition, because mercury must past through the narrowest pores connecting pore network, MIP cannot provide a true pore size distribution of pore structure [35,36].

The gas adsorption method has also been used to identify the pore structure of cement-based materials for decades [36-40]. On the basis of the adsorbed gas quantity, the internal surface area of pores can be evaluated from the Langmuir monomolecular layer theory or the BET multilayer adsorption theory. Furthermore, the pore size distribution can be obtained using Barret-Joyner-helenda (BHJ) interpretation based on the capillary condensation [36]. In this regard, gas adsorption technique provides indirect measurement of pore structure.

Synchrotron-based microtomography has been used to study pore structure in a cement-based materials by various researchers [10,11,13,41]. The significant of this technique as compared with those three techniques is in its ability to capture true three-dimensional internal structure at relative high resolution. It is desirable to know the three-dimensional pore structure from direct observation, especially of the pore distribution, because this would be enable the properties and potential improvement of cement-based materials to be quantified.

1.2.3. Crack geometry

Structural concrete is a typical quasi-brittle material and prone to cracks due to internal shrinkages or external loading [42-44]. For concrete structures during its service life, the degradation of mechanical and durability properties is related intimately to the initiation and propagation of cracks. Cracks turn concrete material from continuous media to discrete ones and significantly changing the mass transport process [44-46]. Thus, quantitative investigation of the crack geometry can provide insight into the durability performance of structural concrete in service condition [44, 46-50].

The most widely used techniques for studying cracks in concrete are optical microscopy

and scanning electron microscopy (SEM). The microscope has been a powerful tool in the study of concrete in the early development of this material. As reported by Nemati [51], Le Chattelier [52] was among the first to apply the microscope to the study of cementitious materials. He used it to investigate the chemical and physical aspect of hydrations and setting, rather than to study cracks. His efforts undoubtedly influenced later workers in their use of a microscope. Tavasci [53] successfully used the microscope to study the composition and structure of concrete, but not of cracks essentially. His work, however, set the stage for studies of cracks on the interior surfaces of specimens [44,54].

The Scanning electron microscope (SEM) has been used with backscattered electron imaging [55,56] to identify and measure microcracks and more recently, SEM has been used to characterize the cracks in sections of mortar or concrete [57-59]. However, the limitations of observing a two-dimensional section of a three-dimensional structure from such 2D microscopy must be borne in mind. The crack geometry that could be derived using both of these techniques limited to the surface of observed crack such as crack width, crack density and surface tortuosity of crack instead of 3D crack network. It is, then, difficult to access the relationship between these crack geometry and its diffusivity due to the process of mass transport inside the crack largely contributed from both surface and internal crack structure rather than crack in the surface itself.

Considering that whole crack structure play important role in mass transport process, the need of instrument that is able to provide description about 3D crack is very urgent in order to allow more accurate prediction of the durability and service life of concrete structure. In this regard, X-ray CT technique arises as a solution in providing such information. X-ray CT technique has been employed by numerous researchers to investigate the three-dimensional of internal crack. Using microfocus X-ray CT, Promentilla and Sugiyama [16] characterize the crack system of the mortars that were exposed to the freezing-thawing action. Kikkawa et al [17] also used this X-ray CT to visualize three-dimensional image of flexural cracks in mortar beams. Recently, Fukuda et al [60] investigate the self-healing phenomena in high strength and ultra-low-permeability concrete. However, all the mentioned investigations using X-ray CT limited to the qualitative analysis instead of quantitative analysis. Though, there are several crack geometries that could be derived from 3D microtomographic images such as crack width distribution, 3D crack tortuosity, constrictivity, which have influences on the mass transport inside the cracks.

1.2.4. Diffusivity in crack

For structure exposed to sea water and/or deicing salt, chloride penetration is a common cause of deterioration of reinforced concrete. In order to predict the service life of such structure, it is necessary to quantify the chloride transport in cementitious materials. The previous researches have been concerned with modeling the diffusion of chloride ion through uncracked concrete based on Fick's second law.

However, in the real environment, concrete structures are not always crack-free. Concrete cracking can be caused by various factors such as; mechanical loading, temperature and moisture gradients, expansive chemical reaction, and drying shrinkage. The formation of cracks increases the transport properties of concrete because cracks space can act as preferential channels so that the transportation of chloride ions by water or moisture movement may take only a few hours to reach the steel, while penetration of ions through the uncracked concrete would take a longer time.

In recent years the effect of cracking on the penetration of concrete has been the subject of numerous investigations. All of these studies have clearly indicated that the presence of cracks could contribute to an increase in the diffusion coefficient. Aldea et al [61] examined the effect of cracking on chloride permeability of concrete. Crack widths under loading

ranging from 50 to 250 μm, were obtained using a splitting tensile test. The chloride permeability was evaluated using a rapid chloride permeability test [62]. The results showed that the chloride permeability increased with the increasing crack width.

Djerbi et al [63] examined the effects of traversing cracks of concrete on chloride diffusion. Three different concretes were used: one ordinary concrete and two high performance concretes with two different mix designs to show the influence of water to cement ratio and addition of mineral admixture. Crack with the average widths ranging from 30 to 250 μm, were induced using a splitting tensile test. Chloride diffusion coefficients of concrete were evaluated using a steady-state migration test [64,65]. The results showed that the diffusion coefficient through the crack was not dependent of material parameters and becomes constant when the crack width is higher than 80 μm, where the value obtained was the diffusion coefficient in free bulk water.

Based on the similar test method, Kato et al [47] concluded that the diffusion coefficients in the crack space increased with the increases in the crack width and was almost constant when the crack width became wider that approximately 75 μm, but this constant diffusion coefficient was about 100 ~ 1000 times higher than that in free water. Ismail et al [66] reported an experimental study on chloride penetration in cracked mortar specimen. The cracks were induced using a mechanical expansive core. Chloride penetration tests were carried out on mortars by using chloride penetration cell. The results obtained for crack opening lower than 30 μm indicate that no chloride diffusion occurred along the crack path.

However, transport phenomena of solute in the crack space of concrete are not clearly understood. Solute can be transported in crack by either capillary absorption, diffusion or both. It is thought that the absorption takes place in air-filled crack in concrete. Hence, the transport of solute by the absorption would be faster than that of diffusion. On the other hand, for solute to diffuse in the crack, the crack space in concrete needs to be saturated with water. Meanwhile, the degree of saturation inside crack space is difficult to measure with certainty. This means that solute diffusion in the crack is controlled by the presence of liquid phase and the diffusion coefficient depends not only on the crack geometry but also on the level of saturation. In this regard, it is therefore necessary to clarify the transport mechanism in cracked concrete.

Nowadays, X-ray CT can be used not only to acquire and determine the three-dimensional crack geometry factors such as tortuosity and constrictivity, but also to visualize the diffusion phenomena in uncracked concrete and inside the cracks or both. To visualize the diffusion phenomena in materials using X-ray CT, it is necessary to give enough contrast through density change using solute as a tracer. In recent years, this technique has been applied in numerous investigations to evaluate the diffusion in rocks. Among the several types of tracer being used, Iodide is one of the most commonly used tracers in diffusion test for rock. Polak et al [67] were able to track and quantify tracer (NaI) diffusion from a fracture into and within the surrounding rock matrix over time using computed tomography (CT). Recently, through diffusion experiment using Potassium Iodide solution (KI) as a tracer, the 3D diffusion-accessible porosity and the distribution of concentration in dolostone has been reported [68].

Solutions containing cesium have also been found to be an appropriate tracer to study diffusion in porous material. For example, diffusion of cesium as a tracer in sedimentary rock was investigated based from the concentration profiles calibrated with CT number as a function of transport distance [69]. In addition, cesium carbonate solution has been used as a tracer in cracked concrete because of its relatively large contrast in CT images obtained from microfocus X-ray CT [17,70]. Investigations that specifically intended to obtain the diffusion coefficient of cesium in cement paste have also been done by several researchers. Kumar et al [71] presented the values of the cesium effective diffusion coefficient by measuring the flux

of ions across hardened cement pastes. Bucur et al [72] evaluated cesium apparent diffusion coefficient in mortar specimen using diffusion cell experiment. With the X-ray CT technique coupled with in-situ cesium tracer diffusion test, the transport phenomena of solute particularly its diffusion inside the crack and through the mortar perpendicular to the crack wall would be further understood.

1.3. RESEARCH OBJECTIVES

Considering the versatility of X-ray CT to study the microstructure of cementitious material, this thesis has four main objectives.

1) To investigate the microstructure of cementitious materials with increasing curing periods by employing synchrotron X-ray CT
2) To characterize the change in microstructure in deteriorated cementitious material due to leaching and mechanical loading using synchrotron X-ray CT and high temperature exposure using microfocus X-ray CT
3) To determine the geometry of crack that is induced by mechanical loading using microfocus X-ray CT
4) To investigate transport phenomena inside the crack using microfocus X-ray CT

1.4. THESIS STRUCTURE

This thesis is divided into seven chapters as shown in Figure 1.1. Chapter 1 provides an overview of the issues and the context in which this research was performed, literature reviews, and introduces the objective of the research works. Chapter 2 introduces the techniques of X-ray computed tomography and explains the theory behind image reconstruction from X-ray CT data. The types of X-ray CT system used in this study are also presented. In chapter 3, details of specimens and experimental procedures used to achieve the target of this study were explained. In addition, the image analysis methods of the microtomographic images derived from X-ray CT scan are also described.

Chapter 4 visualizes the observation results using X-ray CT techniques. There are three major items presented in this chapter; First, the pore structure evolution of cementitious materials with increasing curing periods; Second, change of pore structure in cementitious materials due to leaching mechanism and fire exposure; and finally, three-dimensional crack network in the cracked specimen. Chapter 5 discusses the determination results of solid phases in microtomography images of microstructure of cementitious materials on the basis of linear attenuation coefficient. Chapter 6 discusses the transport phenomena of solute particularly its diffusion inside the crack and through the mortar perpendicular to the crack wall. Chapter 7, the last chapter, draws conclusions from this study.
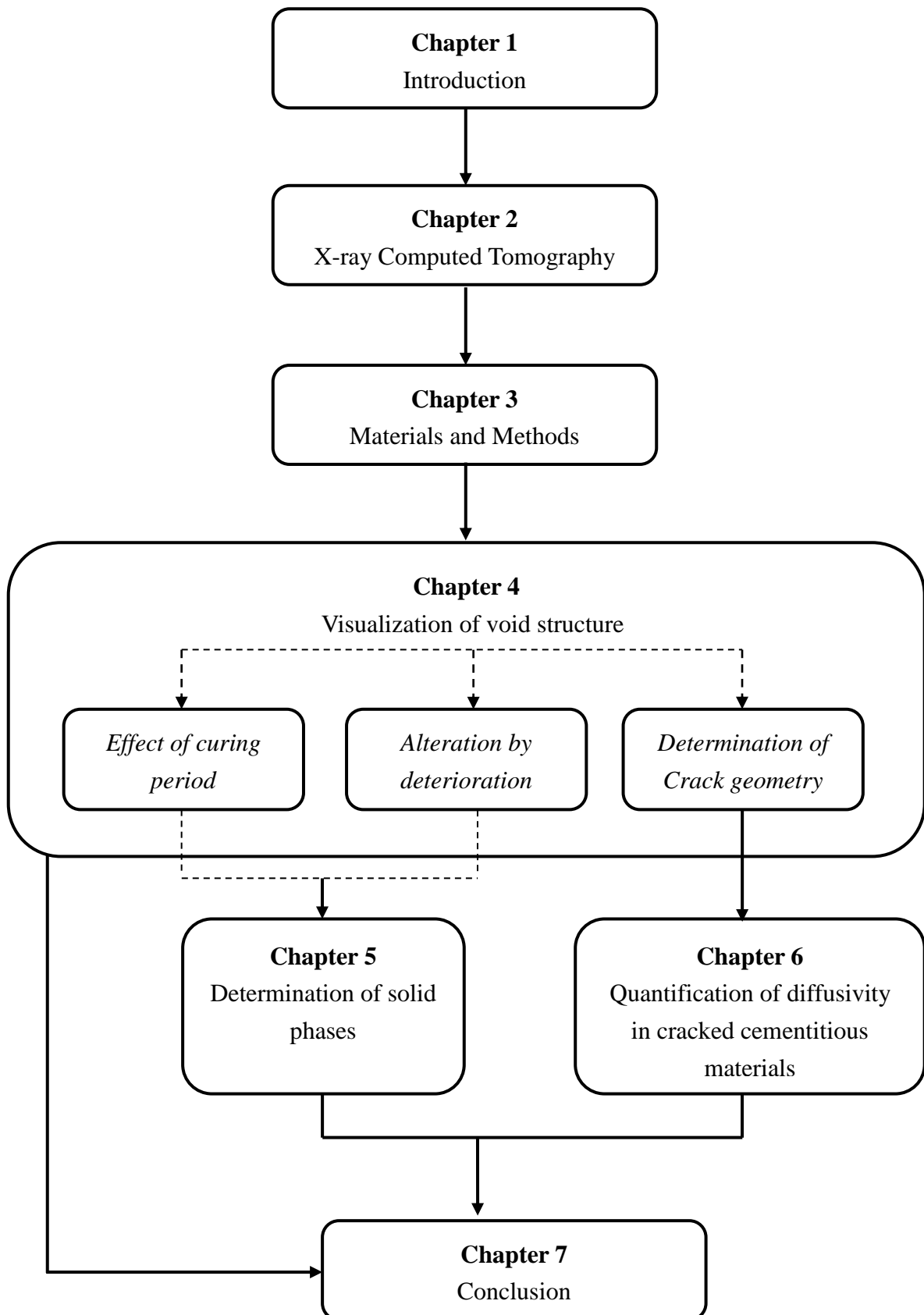
Figure 1.1 Flow of thesis chapters.

CHAPTER 2
X-RAY COMPUTED TOMOGRAPHY

2.1. INTRODUCTION

This chapter provides an overview of X-ray computed tomography (X-ray CT). Specifics of the imaging process, including the acquisition of X-ray data and image reconstruction are presented. In addition, the types of X-ray CT system used in this study are also described.

2.2. X-RAY COMPUTED TOMOGRAPHY

Tomography derives from the Greek word "tomos" which mean "section" or "slice" and "graphia" which mean "to write" or "to draw". As a technique, tomography is a method of digitally cutting open a physical object to reveal its interior details, and can be used to reconstruct full three-dimensional images by collecting two-dimensional slices. In principle, collecting images with X-ray CT requires three main components. These are: (1) an X-ray source and its configuration, (2) a specimen to be imaged, and (3) a detector. CT creates cross section images by projecting X-ray through an object from defined angle positions.

Figure 2.1 shows the illustrative of X-ray transmission measurements through an object. As the X-rays pass through the object, some of them are absorbed and scattered in the object as shown in yellow lines, and some are transmitted and detected by detector as shown in red lines. The process of X-ray intensity reduction, involving just those X-ray which are scattered or absorbed, is called attenuation. X-rays which are attenuated due to the interactions with the object do not reach X-ray detector. X-ray transmitted through the object at each angle are collected on the detector and visualized by computer, creating a complete reconstruction of the scanned image (CT image).

2.3. CT IMAGE RECONSTRUCTION

As shown in Figure 2.1, the objective of CT image reconstruction is to determine how much attenuation of the X-ray beam occurs in each voxel of the reconstruction matrix. These calculated attenuation values are then represented as grey levels in 2-dimensional image of the slice [73]. Techniques to calculate the cross-sectional distribution of attenuation coefficient are based on a well-known law of radiation physics (Lamber-Beer's Law [74]) that states when a monoenergetic X-ray beam (i.e a beam with a single X-ray wavelength) passes
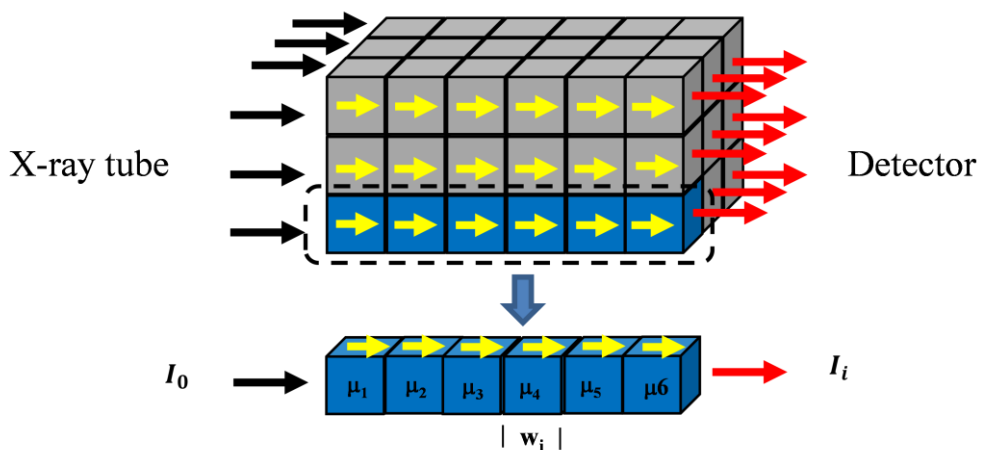
Figure 2.1 X-ray transmission measurements.

through an object of varying densities; it is attenuated according to the exponential relationship [75]:

$$I_i = I_0 e^{-\int \mu \, dl} \tag{2.1}$$

where I_0 is X-ray intensity entering the object, I_i is the detector-measured intensity, dl is the differential length of the path of the beam through the object, and μ are the different attenuation coefficient in the object along the beam path.

In computed tomography, I_0 and I_i are measured from many different angles of view by X-ray detector. These measurements give multiple equations in the same unknown which are solved by various mathematical approaches called image reconstruction. To carry out reconstruction, consider the row of voxels through which a particular ray passes during data collection.

As reported by Goldman [73], the intensity I_1 exiting the first voxel (attenuation μ_1) can be calculated using the expression for exponential attenuation,

$$I_1 = I_0 e^{-(w_1 \mu_1)} \tag{2.2}$$

where w is the voxel width and is equal for all voxels. Similarly, given that the intensity I_1 enters the second voxel, the intensity exiting the second voxel is given by the following equation:

$$I_2 = I_1 e^{-(w_2 \mu_2)} = I_0 e^{-(w_1 \mu_1)} e^{-(w_2 \mu_2)} \tag{2.3}$$

Given that I_2 enters the third voxel, the intensity exiting the third voxel is calculated as follows:

$$I_3 = I_2 e^{-(w_3 \mu_3)} = I_0 e^{-(w_1 \mu_1)} e^{-(w_2 \mu_2)} e^{-(w_3 \mu_3)} \tag{2.4}$$

Proceeding in this fashion through the last voxel,

$$I_i = I_0 e^{-(w_1 \mu_1)} e^{-(w_2 \mu_2)} e^{-(w_3 \mu_3)} \dots \dots e^{-(w_i \mu_i)} \tag{2.5}$$

Dividing both sides by I_0, taking the natural logarithm of each side, and dividing by -1 yield the following equation:

$$-\ln\left(I_i / I_0\right) = w_1 \mu_1 + w_2 \mu_2 + w_3 \mu_3 + \dots\dots + w_i \mu_i \tag{2.6}$$

The left side of Eq.2.6 is designated the processed data point I_i'. Each term $w_i \mu_i$ represent the attenuation occurring within voxel i-, which is designated u_i, yielding the following equation:

$$I_i' = u_1 + u_2 + u_3 + \dots\dots + u_i \tag{2.7}$$

Similarly, measurement for all rays at all positions and angles can be expressed as sum of the attenuation values in voxel through which each ray pas. Note that the quantity I_i' is known, it is calculated from each detector measurement I_i with the known X and Y voxel dimension and the known X-ray intensity entering the object (I_0).

9

2.3.1. Algebraic Reconstruction Technique (ART)

Figure 2.2 illustrates the relationship between the measured views and the corresponding image. Each sample in the view (intensity profile) acquired in a CT system is equal to the sum of the image values along the ray that points to that sample. For example, view 1 (0 degree) is found by adding all the pixels in each row. Likewise, view 3 (90 degree) is found by adding all the pixels in each column. The other views, such as view 2 (45 degree) and view 4 (135 degree), sum the pixels along rays that are at an angle.

There are several main approaches to calculate the slice image given the set of its views. These are called CT reconstruction algorithms. The first method is Algebraic Reconstruction Technique (ART). As reported by Smith [76], to start the ART algorithm, all the pixels in the image array set to the some arbitrary value. An iterative procedure is then used to gradually change the image array to correspond to the profiles. An iteration cycle consists of looping through each of the measured data points. The measured sample is compared with the sum of the image pixel along the ray pointing to the sample. If the ray sum is lower than the measured sample, all the pixels along the ray are increased in value. Likewise, if the ray sum is higher than the measured sample, all of the pixel values along the ray are decreased.

Following the step by step in the calculation of attenuation values in a simple 2-row by 2-column reconstruction matrix as described by Goldman [73], we try to determine the attenuation values in 5-row by 5-column reconstruction matrix (Figure 2.2). A view is collected at 4 angles, 0° (left to right), 45° (diagonal), 90° (top to bottom), and 135° (diagonal), and each measurement is expressed as the sum of the voxel attenuation values along each ray. As shown in Figure 2.3, the process begins by taking measurement of the first view (0 degree), and assuming that these attenuation values occurred uniformly along the rays, yielding the first image estimation (Figure 2.3(a)). Next, measurements of the second view are taken and these values are compared with the summed attenuation values that would have occurred if
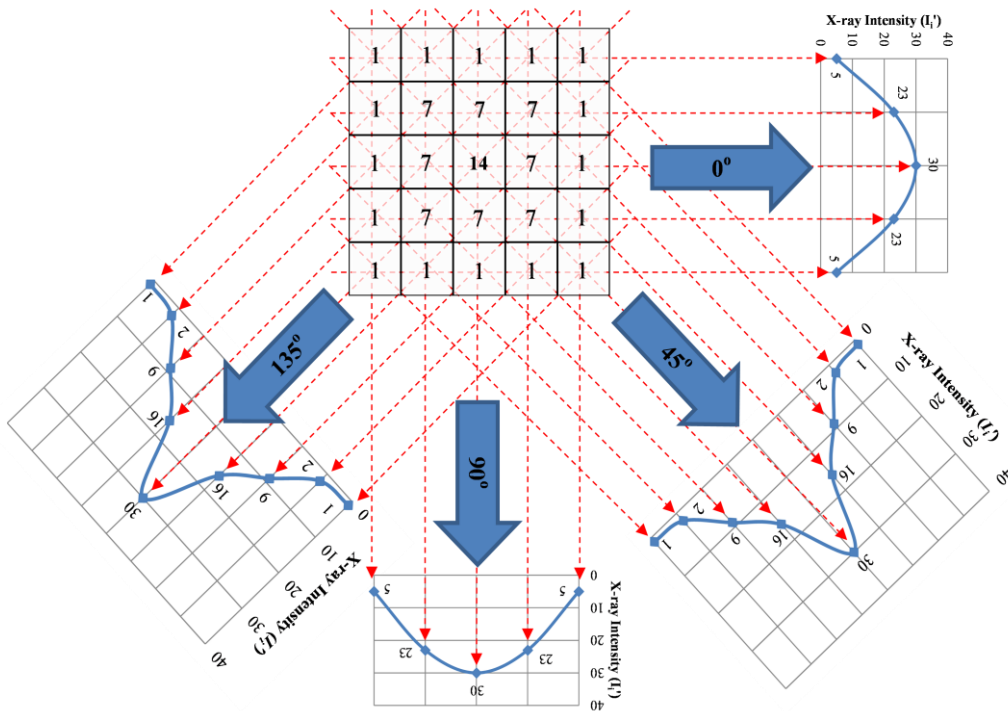
Figure 2.2 CT views. Intensity profile for 4 angles, 0° (left to right), 45° (diagonal), 90° (top to bottom), and 135° (diagonal).

the first estimation were correct. Next, the first estimation is adjusted to make it match the actual values of the second view. An adjustment for each measurement of the second view is calculated by subtracting the value predicted for it by the first estimation from its actual value (Figure 2.3(b)). Next, these adjustments are divided equally along the ray, yielding the second estimation (Figure 2.3(c)). The process continues in this manner, with the actual values for each view being compared in turn with the values predicted by the latest estimation (Figure 2.3(d), (e), (f)). Because the attenuation values predicted by the last estimation match all actual measurements (Figure 2.3), the image is accepted as the true reconstructed image (Figure 2.3(g)).

(a) First estimation from first view (0 degree)

(b) Adjustment to the second views

(c) Second estimation

(d) Adjustment to the third views
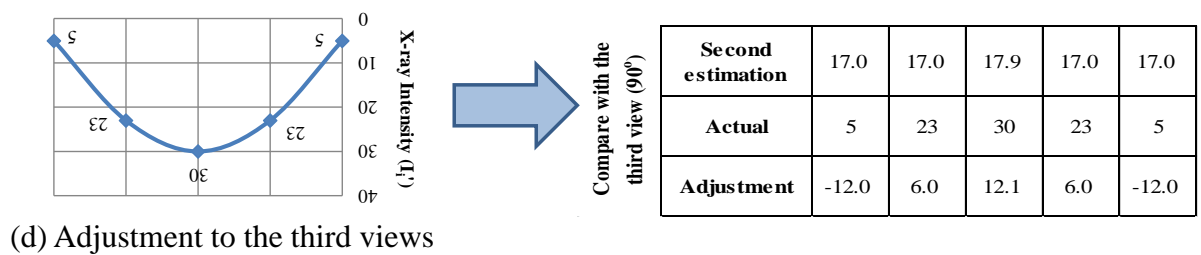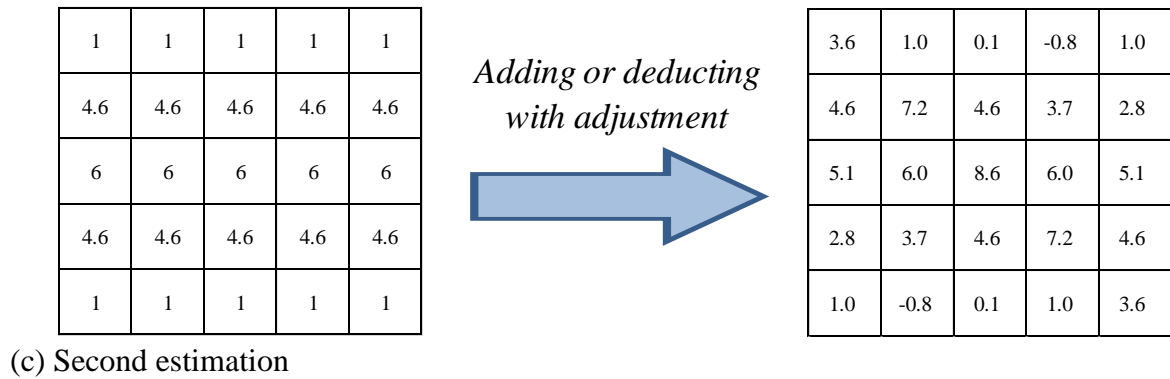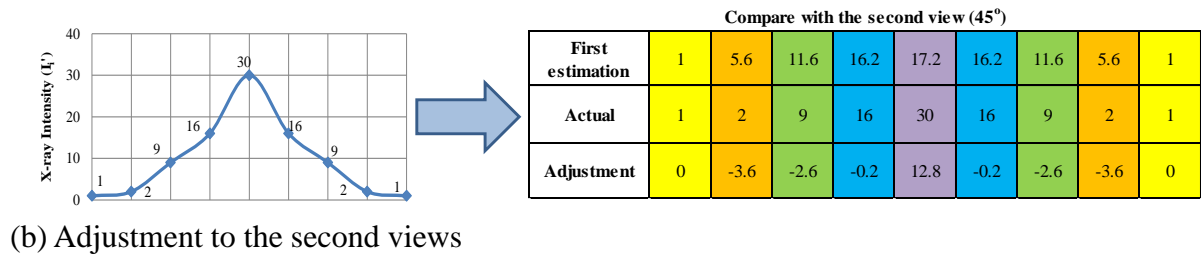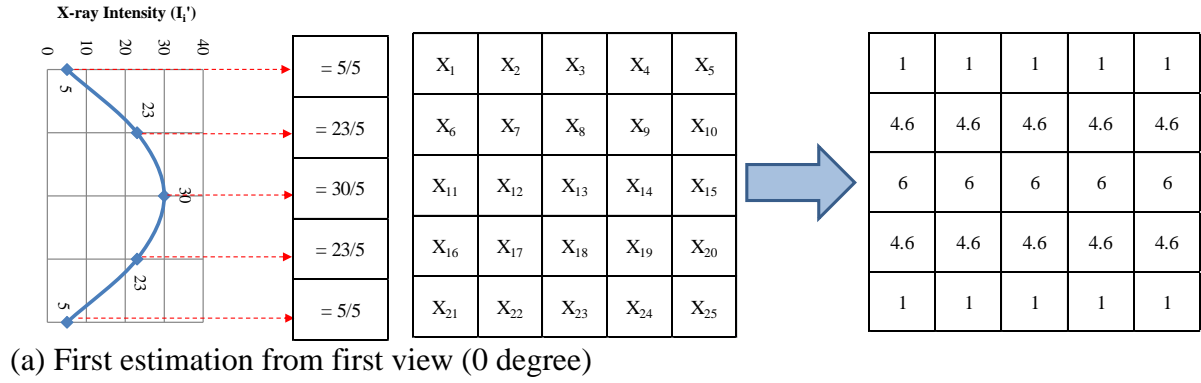
Figure 2.3 ART algorithm for 25 voxels reconstruction matrix.

3.6	1.0	0.1	-0.8	1.0
4.6	7.2	4.6	3.7	2.8
5.1	6.0	8.6	6.0	5.1
2.8	3.7	4.6	7.2	4.6
1.0	-0.8	0.1	1.0	3.6

Adding or deducting with adjustment →

1.2	2.2	2.5	0.4	-1.4
2.1	8.4	7.0	4.9	0.4
2.7	7.2	11.0	7.2	2.7
0.4	4.9	7.0	8.4	2.1
-1.4	0.4	2.5	2.2	1.2

(e) Third estimation
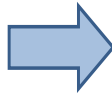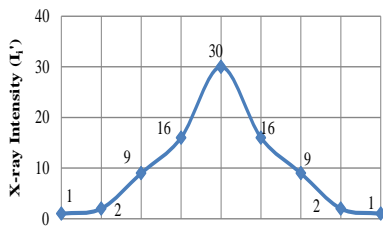
Compare with the fourth view (135°)

Fouth estimation	1.2	4.3	13.6	14.9	18.0	14.9	13.6	4.3	1.2
Actual	1	2	9	16	30	16	9	2	1
Adjustment	-0.2	-2.3	-4.6	1.1	12.0	1.1	-4.6	-2.3	-0.2

(f) Adjustment to the fourth views

1.2	2.2	2.5	0.4	-1.4
2.1	8.4	7.0	4.9	0.4
2.7	7.2	11.0	7.2	2.7
0.4	4.9	7.0	8.4	2.1
-1.4	0.4	2.5	2.2	1.2

Adding or deducting with adjustment →

1	1	1	1	1
1	7	7	7	1
1	7	14	7	1
1	7	7	7	1
1	1	1	1	1

(g) Final estimation

Figure 2.3 ART algorithm for 25 voxels (continue).

However, no estimation that ART results will ever match all measurement exactly, because the measurements include random errors. Thus, ART must be discontinued after an estimation that matches all measurement only within some tolerance is found; however, that tolerance may not be met even after many iterations for higher size of reconstruction matrix [73].

2.3.2. Backprojection Technique

Considering the problem arises from the ART method, another techniques was developed for a better reconstruction algorithm based on the idea of backprojection. An individual sample in Figure 2.2 is backprojected by setting all the image pixels along the ray pointing to the sample to the same value. In other words, a backprojection is formed by smearing each view back through the image in the direction it was originally acquired. The final backprojected image is then taken as the sum of all the back projected views [76].

(a) Backprojected first view

(b) Backprojected second view

(c) Backprojected Third view

(d) Backprojected fourth view

(e) Summing backprojected views from all angles

Figure 2.4 Backprojection technique. (a) Backprojected first view. (b) Backprojected second view. (c) Backprojected third view. (d) Backprojected fourth view. (e) Summing backprojected views from all angles.

Using the same example shown in the Figure 2.2, the backprojection is then applied in order to reconstruct the corresponding image based on the a set of views which were acquired from CT. Similarly with the ART, the process begins by taking measurement of the first view and the attenuation measurement of this view are simply divided evenly along the path of the ray, yielding the attenuation values of 1, 4.6, 6, 4.6 and 1 for row number 1, 2, 3, 4 and 5 respectively (Figure 2.4(a)). Next, from second view to fourth view each projection was backprojected as shown in Figure 2.4(b) to (d) in which attenuation values are divided evenly according to the number of pixels traversed by the ray. Subsequently, each backprojected view summed according to the order of rows and columns (Figure 2.4(e)). Finally, the summed attenuation values from all angles in each pixel were divided by 4 (according to contribution of attenuation measurement from each view), yielding the reconstructed image shown in Figure 2.5.

From Figure 2.5 (a) and (b), it can be seen that there is a significant difference of the attenuation values in each pixel between reconstructed matrix resulting from backprojection technique and original image. This problem is due to the fact that during the backprojection process, each intensity value is attributed to all pixels along the path of the ray and not only to the attenuated pixels because the attenuated pixels locations are unknown [77]. In the real case, the reconstructed images using backprojection technique may cause blurring (less sharp) in reconstructing an image considering all backprojected projection. This blurring is a natural result of the scanning and backprojection process, but there is a solution: The blurring can be

1	1	1	1	1
1	7	7	7	1
1	7	14	7	1
1	7	7	7	1
1	1	1	1	1

(a) Original data

2	3	3	3	2
3	5	5	5	3
3	5	6	5	3
3	5	5	5	3
2	3	3	3	2

(b) Backprojection technique
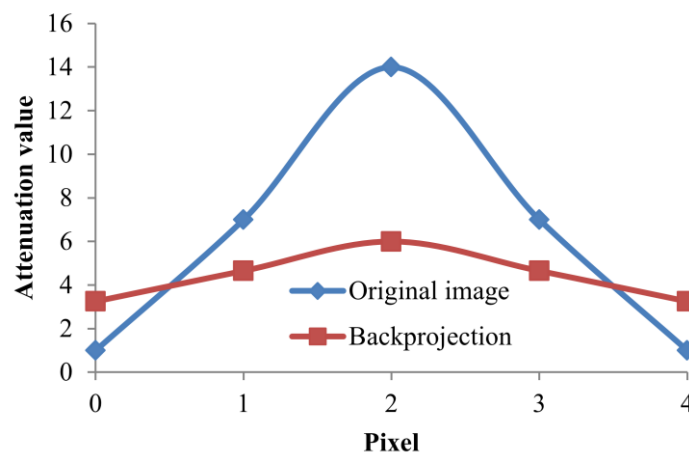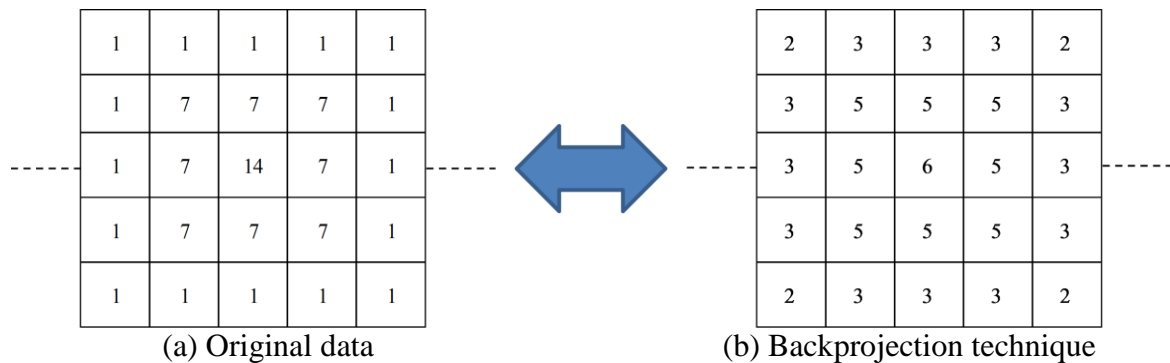
(c)Activity profile drawn along dashed line

Figure 2.5 Comparison of original data (a) and reconstructed matrix from backprojection technique (b). (c) Activity profile drawn along dashed line in (a) and (b). More gentle curve after backprojection is illustration of blur.

solved by a mathematic process known as filtering. In this regard, the following question is frequently asked: *why do we apply a filter?* Technically, backprojection method without filter produces a widely spread out point object. However, when a filter is applied in the projection, it will cancel the vicinity of the object. Thus, the result is a shaper reconstructed image. This reconstruction algorithm is known as filtered backprojection. Filtered backprojection (FBP) reconstructs an image by filtering each view before backprojection. This removes the blurring seen in the simple backprojection, and results in a mathematically exact reconstruction of the image.

2.3.3. Micro-focus X-ray CT and synchrotron X-ray CT

In micro-focus X-ray CT system, after the computer calculates the linear attenuation coefficient for each voxel via filtered back projection, the values are normalized to the value for water as reference, scaled and presented as a Hounsfield or CT Number which is defined as [73]:

$$\text{CT Number} = 1000 \frac{\mu_m - \mu_{water}}{\mu_{water}} \qquad (2.8)$$

where μ_m and μ_{water} are the linear attenuation coefficients for tissue material and for water, respectively. The reason for calculating CT Numbers relative to the water is due to linear attenuation of water will always be approximately 0 but not necessarily exactly 0 because of some noise.

Nowadays, the CT Number has been applied to the majority of industrial CT or laboratory instead of attenuation value. This is because the independence of CT Number to the X-ray beam energy. In this regard, the same material has a similar CT Number although it has been measured by different X-ray CT with a different X-ray beam energy. It is certainly facilitating in identification analysis as some researches have suggested CT Number for some of interest materials.

Subsequently, the image is presented on a computer monitor using a grey scale. The grey scale is chosen to encompass all or some part of the entire range of CT Number by selecting a suitable window level (WL) and window width (WW). The window width is the range of CT Number selected for display and the window level is the central CT Number about which the window is chosen. Typically, the highest number is assigned to white and the lowest number to black with all intervening numbers assigned intensities on a linear scale. WL of 250 and WW of 500 are generally used for the case of concrete materials, which have range of interest of 0 to 500 (Figure 2.6) as shown in Figure 2.7.
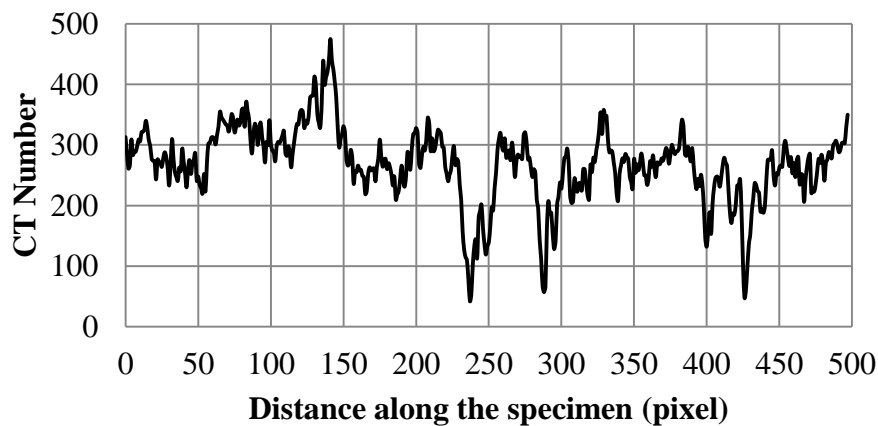
Figure 2.6 CT Number profile of concrete.
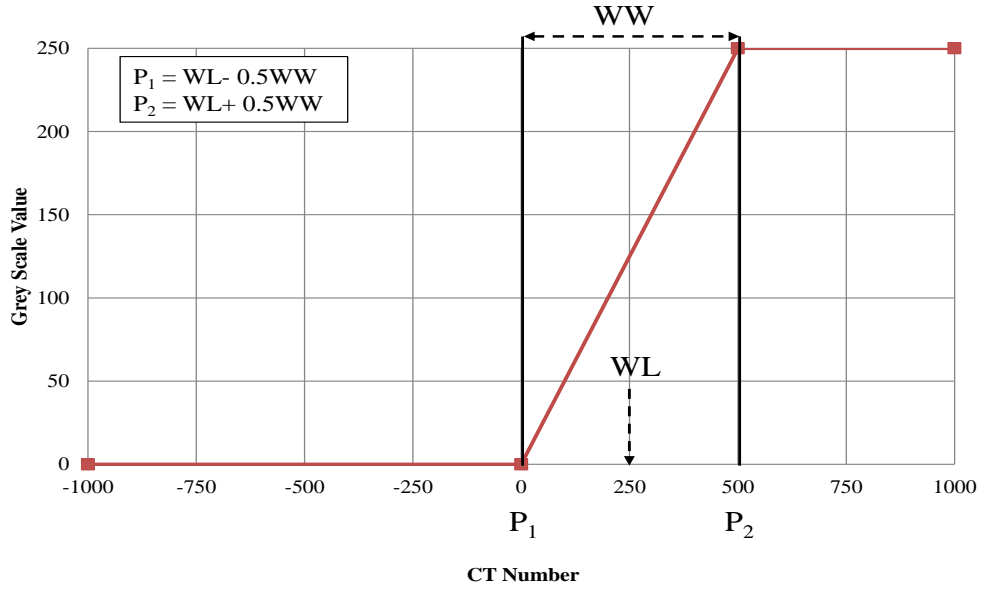
Figure 2.7 Windowing the range of CT Number.

On the other hand, as for synchrotron X-ray CT, after the computer calculates the linear attenuation coefficient for each voxel via filtered back projection, the measured linear attenuation coefficients were directly converted to the color intensity values. Figure 2.8 illustrates the conversion method of measured linear attenuation coefficient range from -20 to 100 cm^{-1} (general in normal cement paste specimen with beam energy of 15 keV) to the color intensity range from 0 to 65535 to produced 16-bit image in which the value between maximum and minimum of linear attenuation coefficient was divided linearly to the value of 65535. In this regard, the images have a lower contrast because linear attenuation coefficient of each voxel was represented with color intensity range from 0 to 65535.
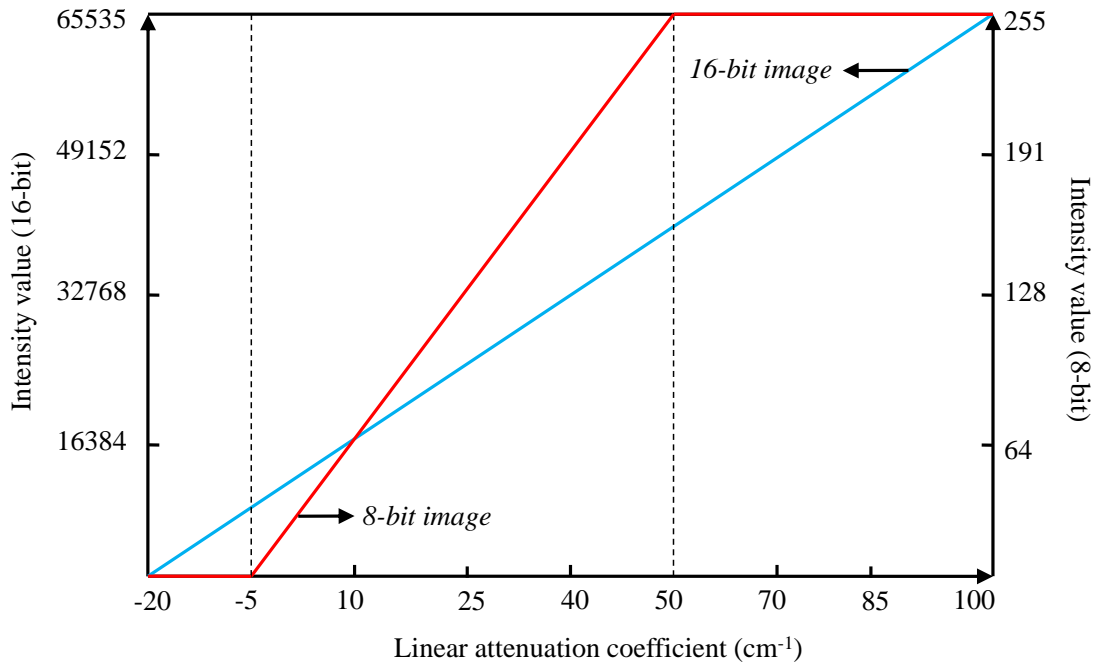
Figure 2.8 Example reconstruction image before and after normalization process

Considering a lower level of image contrast and also consumed a lot of memory during image analyzing process using 16-bit image, generally, the images were normalized. Image normalization process was intended to improve the contrast in the image by scaling the measured linear attenuation coefficient and converting to an 8-bit gray scale image with intensity value range from 0 to 255. As shown in Figure 2.8, minimum cut-off and maximum cut-off was set to a specific value, in this illustration are -5 and 50 cm^{-1}, respectively. Furthermore, the value between maximum and minimum of normalized linear attenuation coefficient was divided linearly to the value of 255.

2.4. X-RAY CT SYSTEM USED IN THIS STUDY

In this study, two types of X-ray CT were used to acquire the 3D image of internal structure of cementitious materials as shown in Table 2.1. The first was X-ray CT with synchrotron radiation (synchrotron X-ray CT) and the second was cone beam X-ray CT with μ-focus tube (micro-focus X-ray CT). For micro-focus X-ray CT, we used a desktop micro-focus CT system at Hokkaido University, Japan. (TOSCANER-30000μhd, Toshiba IT & Control System Corporation, Japan). A schematic illustration of X-ray CT system at Hokkaido University is shown in Figure 2.9. The microfocus X-ray CT scanner consists of a microfocus X-ray source, a specimen manipulator, an image intensifier (II) detector coupled to a CCD camera and an image processing unit [16]. A power setting of 130 kV and 124 μA was used for a full (360^0) cone-beam scan with 1500 projection views. The specimen was set in the holder mounted on a precision rotation table, and then the table position was adjusted to fit the image within the field-of-view (Figure 2.9). Furthermore, the position of FCD (focus chamber distance), FID (focus image distance) and X-ray CT chamber condition were adjusted to obtain high resolution images as well as to reduce the noise and artifacts in the images during acquisition. The image acquisition time for each specimen that includes both scanning and reconstruction time was about one and a half hours.

For synchrotron X-ray CT, BL20XU beamline at SPring-8, which is the world's largest third generation synchrotron radiation facility, was used to obtain set of CT slices/images. A schematic illustration of X-Ray imaging system at SPring-8 is shown in Figure 2.10. The system consists of an X-Ray light source from the beam line, double crystal monochromator, high-precision rotation stage, and high-resolution X-Ray image detector. The transmitted intensities are detected by X-Ray imaged detector that consists of a thin scintillator, optic system and CCD camera [78]. Moreover, the beam energy was set to a value of either 15 keV or 25 keV. Using a high precision rotating stage, 1500 projection image were taken at different views with an exposure time of 0.3 s per projection and angle step of 0.12^0 through the 180^0 rotation.

Table 2.1 Details information of Micro-focus X-ray CT and synchrotron X-ray CT used in this study

Items	Micro-focus X-ray CT	Synchrotron X-ray CT
X-ray source	130 kV m-focus tube	15 and 25 keV
Image reconstruction algorithm	Filtered back projection	Filtered back projection
Cross-section image size	1024×1024	2000×2000
Voxel size	> 10μm^3	0.5 μm^3
Specimen	Cement paste, mortar and concrete	Cement paste, mortar
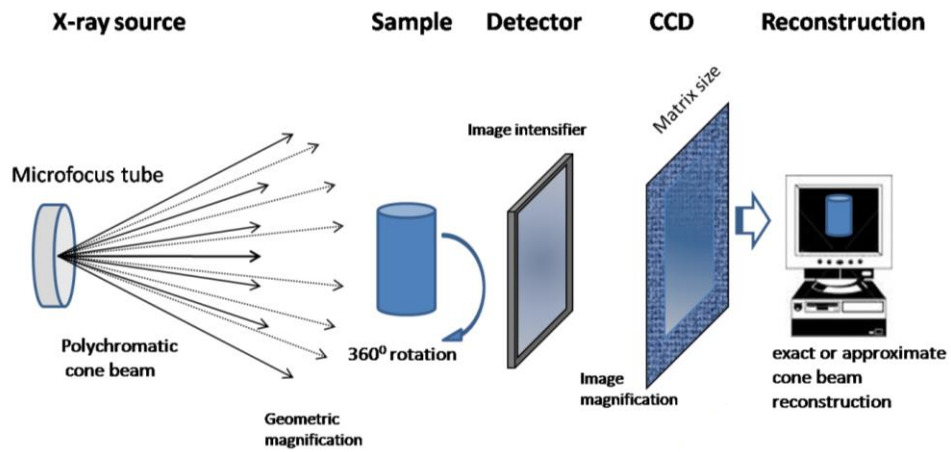
(a)
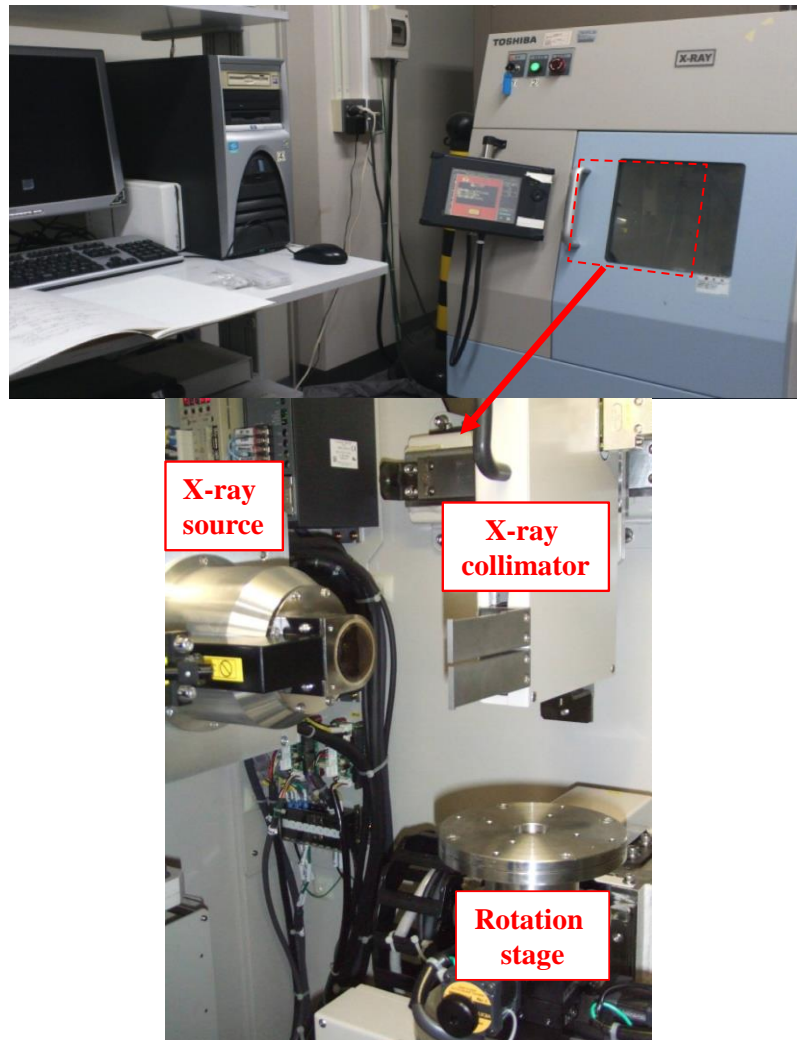
(b)

Figure 2.9 Micro-focus X-ray CT (a) an illustrative of X-ray CT system [16] (b) TOSCANER-30000µhdX-ray CT at Hokkaido University.

X-ray source   **Sample**   **Detector**   **CCD**   **Reconstruction**

(a)

(b)
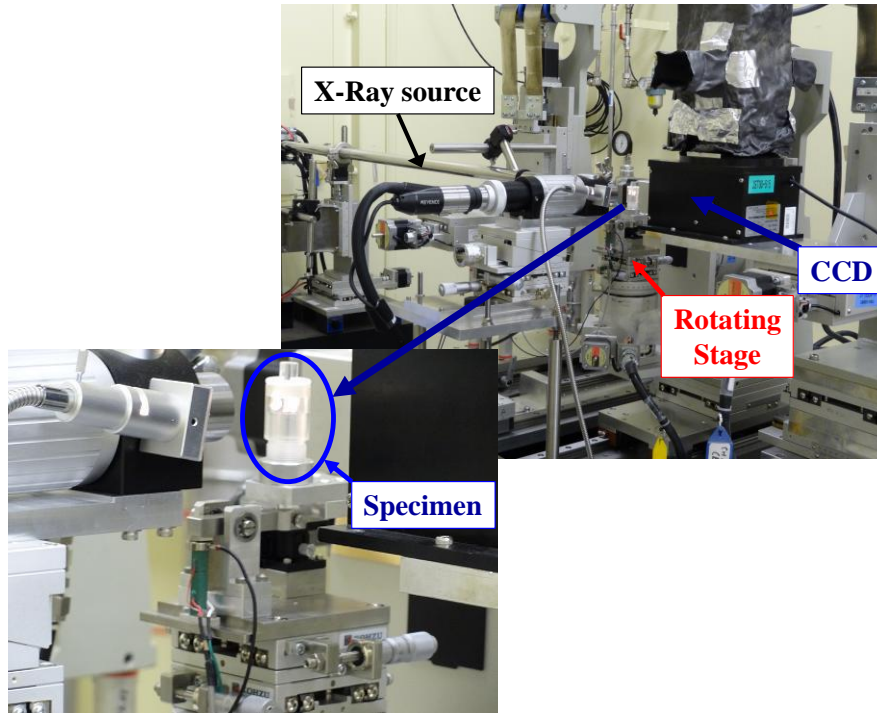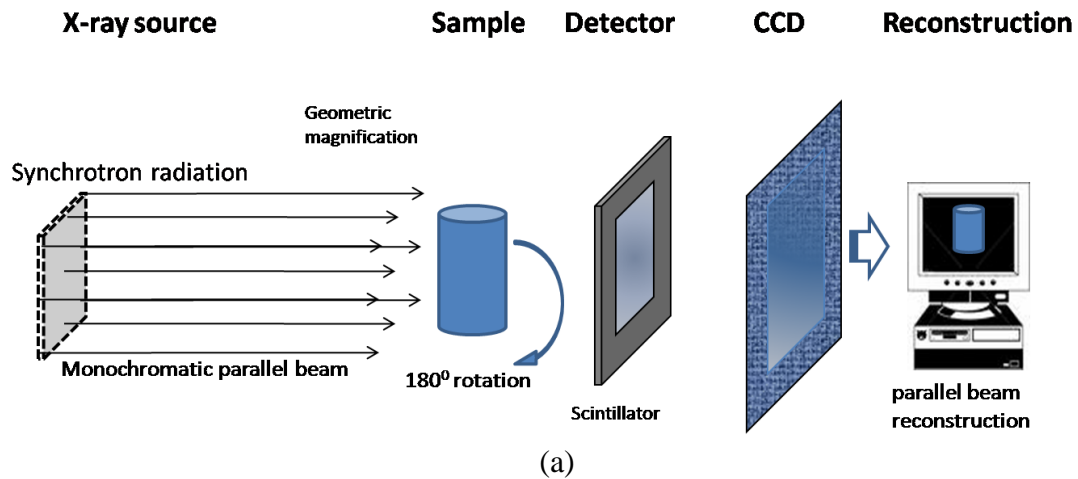
Figure 2.10 Synchrotron X-ray CT (a) an illustrative of synchrotron X-ray CT system [10] (b) BL20XU beamline at SPring-8, Japan.

2.5. SUMMARY

In principle, the idea of CT image reconstruction is to determine the attenuation of X-ray intensity occurs in each voxel of the reconstruction matrix. There are three methods that can be used to determined X-ray CT attenuation namely Algebraic Reconstruction Technique (ART), backprojection technique and filtered backprojection technique. Considering filtered backprojection technique results in a mathematically exact reconstruction of the image, thus this method widely applied in most the X-ray CT system.

In this study, two types of X-ray CT were used to acquire the 3D image of internal

structure of cementitious materials. The first was X-ray CT with synchrotron radiation (synchrotron X-ray CT) at SPring-8, Japan, and the second was cone beam X-ray CT with μ-focus tube (micro-focus X-ray CT) at Hokkaido University, Japan. The primary difference between synchrotron and micro-focus X-ray CT is measurement. The synchrotron X-ray CT can provide Linear Attenuation Coefficient (LAC) while micro-focus X-ray CT gives CT values. LAC provided by synchrotron X-ray CT allows us to identify different phase in the cementitious materials whereas CT number produced by micro-focus X-ray CT allows us to detect the change in the density in cementitious materials.

CHAPTER 3
MATERIALS AND METHODS

3.1. SPECIMEN PREPARATION AND EXPERIMENTAL PROCEDURE
3.1.1. Evolution of pore structure

There are two types of cement paste specimens used to evaluate the evolution of pore structure in cementitious material with increasing curing periods as shown in Table 3.1. The first was the ordinary Portland cement (OPC) paste with water to binder ratio of 0.5 (hereinafter OPC-CP-05). The second was cement paste with a low alkali binder under similar water to binder ratio of OPC paste specimen. A mixture of OPC, silica fume and fly ash (hereinafter HFSC-CP-05) was used as a low alkali binder with a composition of 40% OPC, 20% silica fume (Micron-silica 640U) and 40% type II fly ash specified in JIS A6201. The physical properties and chemical composition of OPC and fly ash are given in Table 3.2.

After mixing the cement pastes, it was sealed for one day followed by curing in water until predetermined ages of 2, 7, 28 and 146 days, respectively. In this way, the total of cement paste specimens was 8 specimens as shown in Table 3.1. Details of specimen preparation for X-ray CT scan are described elsewhere [7,10]. Each specimen, then, was crushed and the crushed pieces were soaked with acetone to suspend its hydration process. A fragment of about 1 mm at its greatest width and 1 mm in length was prepared from the crushed sample to examine the internal pore structure with synchrotron-based microtomography. In the study of pore evolution with increasing curing periods, BL20XU beamline at SPring-8 was used to obtain set of CT slices/images of each specimen. The beam energy was set to a value of 15 keV to obtain 1300 contiguous grayscale images, in which each slice image contained 2000 x 2000 voxel. The dimension of a voxel is a 0.5 x 0.5 micrometer-sized pixel with a thickness of 0.5 μm. Thus, the effective size of the cubic voxel is 0.5 μm in the CT image.

Table 3.1 Details specimens used in the study of the evolution pore structure with increasing curing periods

Specimen ID		W/B	Curing period (days)	Binder (B) composition		
				OPC	FA	SF
OPC paste	OPC-CP-50-2d	0.5	2	1	-	-
	OPC-CP-50-7d		7		-	-
	OPC-CP-50-28d		28		-	-
	OPC-CP-50-146d		146		-	-
Low alkali cement paste	HFSC-CP-50-2d	0.5	2	0.4	0.4	0.2
	HFSC-CP-50-7d		7			
	HFSC-CP-50-28d		28			
	HFSC-CP-50-146d		146			

Table 3.2 Physical properties and chemical composition of OPC and fly ash

Specimen	Density (g/cm^3)	Blaine (cm^2/g)	LOI (%)	Chemical composition (%)									
				SiO2	Al_2O_3	Fe_2O_3	TiO_2	MnO	CaO	MgO	SO_3	Na_2O	K_2O
OPC	3.17	3340	0.53	21.40	5.38	2.83	0.28	0.08	64.44	1.66	1.92	0.32	0.46
FA	2.16	3610	2.40	66.42	18.88	3.63	0.82	0.03	0.90	0.54	0.15	0.04	1.23

3.1.2. Pore structure in deteriorated cementitious materials

a. Leaching

Using the same mix proportion used in the study of the evolution of pore structure in cementitious materials as shown in Table 3.1, two cylinders of cement paste specimen with size of 50 mm in diameter and 100 mm in length were prepared. These specimens were cured in water for 146 days prior to the accelerated leaching test. For electrically accelerated leaching test, the size of specimen prepared was 50 mm in diameter and 10 mm in length (Figure 3.1). Details of this experimental set-up are described elsewhere [79,80]. After a curing period of 146 days the disc-shaped specimen was placed between two Acryl-made compartments, each containing 1L of ion-exchanged water. One compartment has an anode made of platinum (Pt) and the other has a stainless steel (SUS) cathode. These two electrodes are connected via an electrical DC power source to provide a potential gradient of 10 volt across the specimen. The application of electrical field accelerates the transport of Ca^{2+} to the cathode side. In this study, cement paste specimen was subjected to accelerated leaching test for 13 weeks prior to the X-ray CT measurement. Details of specimen preparation for X-ray CT scan are described elsewhere [13]. For the microtomographic studies, a portion that was cut 2 mm from the surface layer of the specimen that was exposed in the cathode side was prepared (Figure 3.1). From each cut portion, a shard of about 1 mm at its greatest width and 1 mm length was obtained to examine the change in the internal pore structure due to leaching with synchrotron-based microtomography at SPring-8, Japan.

b. High temperature exposure and re-curing

Figure 3.2 shows an overview of the experimental program of the study of change in the pore structure of concrete due to fire exposure. Concrete specimen (hereinafter OPC-C-30) was prepared with a water-cement ratio (W/C) of 0.30, a very low W/C typical of high strength cementitious materials. The complete concrete mix proportions are given in Table 3.3. Ordinary Portland cement (C) was used as the binder, along with fine (S) and coarse (G)
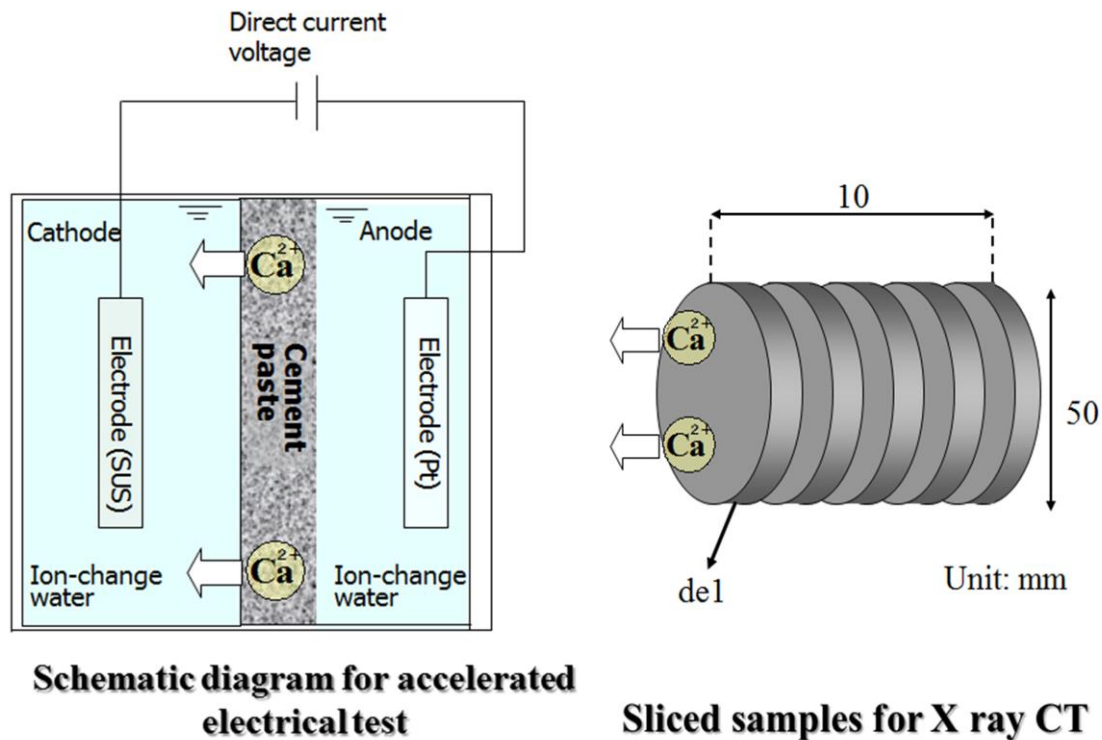
Figure 3.1 Electrochemical acceleration test [13].

aggregates from the Shizunai River and super plasticizer (SP) and anti-foaming (AF) admixtures for meeting workability requirements. The workability of the fresh concrete was evaluated using the slump flow and air content, which were measured following the (Japanese Industrial Standard) JIS A 1150 and JIS A 1128, respectively. The target slump flow was 45 cm and the target air content was 5%.

After casting, four cylinders (100 x 200 mm) were sealed and cured in the molds for 24 hours, then removed and placed in water curing at 20ºC for four weeks. A single cylinder was then removed from water curing and a 20 mm core was extracted from the center of the

Table 3.3 Mix proportion of concrete for high temperature exposure

| W/C | s/a | Max. agg. size (mm) | Unit content (kg/m^3) | | | | Chemical admixture (%) | | Slump flow (cm) | Air (%) | 91-day comp. strength (MPa) |
			W	C	S	G	SP	AF			
0.30	0.5	25	159	530	796	903	0.9	0.006	46.7	5.1	67.5

Specimens → Concrete specimen W/C = 0.3

Curing → 13 weeks in water

Heating → 10° C / min. 600^oC for 1 hour

X-Ray CT → After heating

Re-curing → 1 and 4 weeks in water and air

X-Ray CT → After re-curing
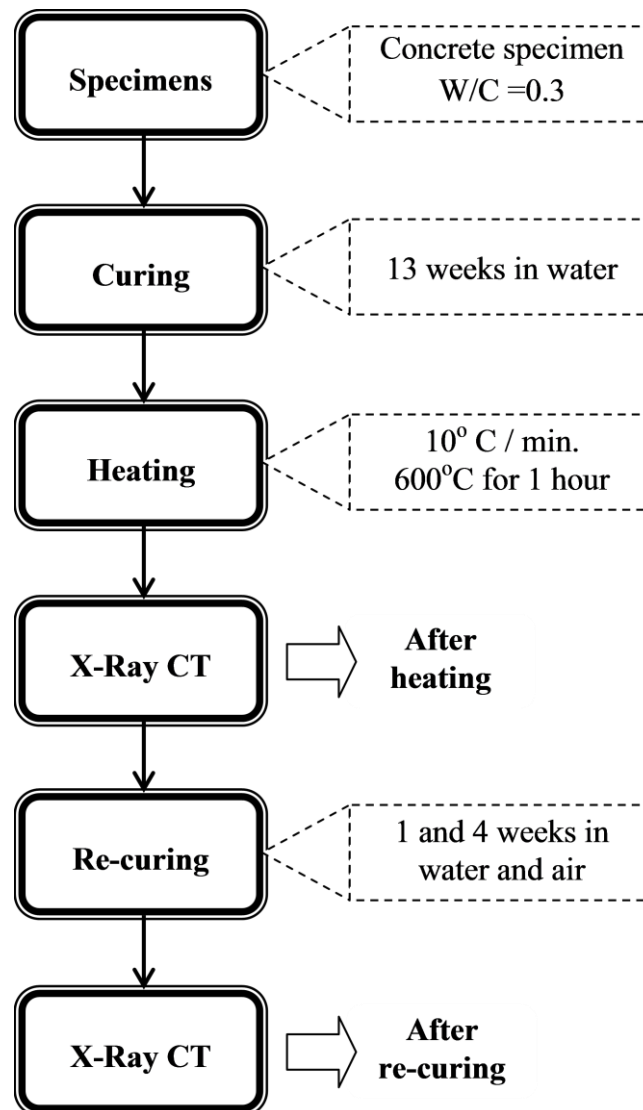
Figure 3.2 Overview of the experimental program of the study of change in pore structure due to high temperature exposure.

cylinder. This core was cut into two 20 mm segments, which were then returned to water curing for another nine weeks. Total curing time from casting to heating was 13 weeks (91 days) in order to achieve a high degree of hydration similar to that of concrete structures in service. The 91-day compressive strength, which was measured using three standard cylinders from the same concrete mix, was 67.5 MPa.

Fire exposure was simulated using an electric furnace with a temperature control program. The rate of heat increase was set at 10ºC per minute until the target exposure temperature of 600ºC was reached, after which it was maintained for one hour. The target exposure temperature of 600ºC was selected because the dehydration of calcium hydroxide occurs between 450ºC and 550ºC and produces calcium oxide [18], the rehydration of which has been shown to contribute to the recovery of strength and durability performance under re-curing [81]. Therefore, this temperature enabled the examination of the case in which high degrees of both dehydration and rehydration would occur.

After the conclusion of the high temperature exposure, the door of the furnace was opened and the specimens were allowed to cool in the furnace until the internal furnace temperature dropped below 100ºC. Specimens were then removed from the furnace and cooled at room temperature for approximately one hour before being placed in one of two re-curing conditions. Air re-cured specimens were placed in a temperature-controlled environment at 20ºC, whereas water re-cured specimens were placed in conditions similar to the initial curing period. Re-curing was carried out for one and four weeks.

In this research, a desktop micro-focus CT system at Hokkaido University was used for acquiring the slice images. Image acquisition was carried after heating, and after one and four weeks of re-curing in water and air. The focus area for data acquisition was approximately 11.5 mm in height, 20.0 mm in diameter, and roughly centered on the specimen. In this area, 351 slices were obtained. Each slice was 1024 by 1024 pixels in size, with each pixel 22 microns by 22 microns. After image processing and scaling, the voxel size was 22 by 22 by 22 microns.

c.   Tensional force

Table 3.4 shows a set of mixture proportion used for microtomography study. Ordinary Portland Cement (OPC) and JIS type II fly ash are used as a binder material. Replacement of fly ash for OPC ratio is 0.15 by mass, while water to binder ratio (W/B) was fixed at 0.5. Fresh mortar was placed into the mold in a size of 40 x 40 x 160 mm and cured in water for 28 days. After 28 days curing periods, mortar is cut to obtain a sample size of 1 mm x 1 mm no less than 15 mm in length as shown in Figure 3.3(a). Aggregates with a diameter of less than 0.5 mm are utilized to avoid the possibility of cross section along the specimen is dominated by the aggregate.

Figure 3.3(b) shows the instrument used in the application of tensile force. Electrical energy that flows into the piezoelectric actuator is converted into a force that propels the lever above it. Furthermore, due to the movement of the tip of the lever toward the top, then the other end of the lever moves downward. Downward movement of the lever becomes the tensile force which is applied to the specimen. The amount of force applied is read by a load cell which is above the piezoelectric.

Table 3.4 Mix proportion of mortar for micro-tensile test

Specimen ID	W/B	S/B	FA/(OPC+FA)	28 days compressive strength (MPa)
FA-MR-μT	0.5	1.5	0.15	49.3

<div align="center">(a)   (b)</div>
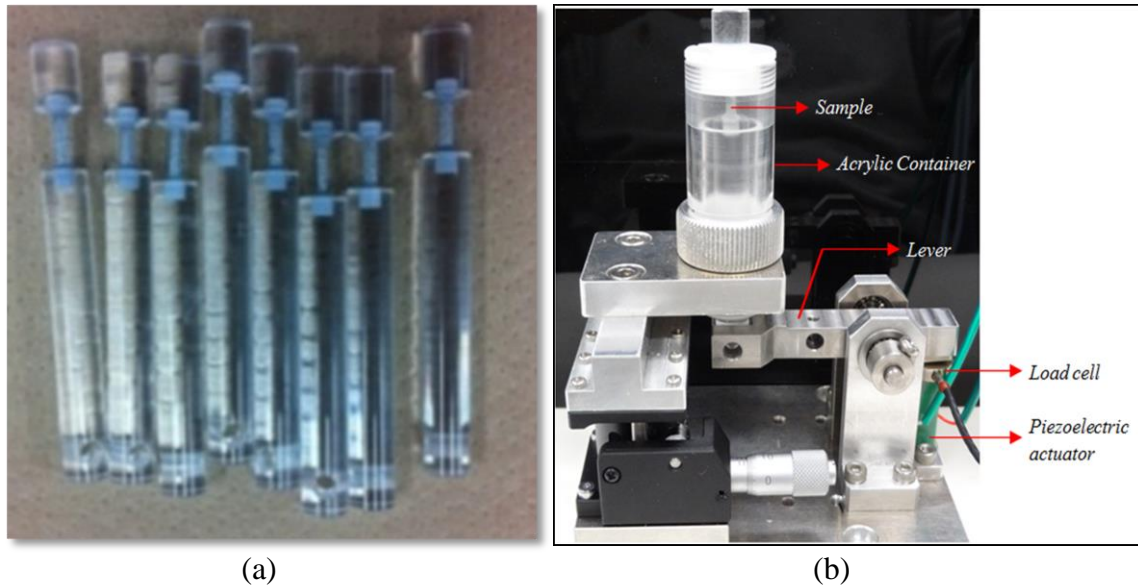
Figure 3.3 Preparation of mortar specimen. (a) A set of sample for micro-tensile test, (b) Micro-tensile test instrument.

3.1.3. Pre-cracking and its effect on diffusion test

Table 3.5 summarizes the mix proportion of the mortar specimens used in the study of three-dimensional crack geometry of cracked mortar due to the mechanical loading and its diffusivity. The Ordinary Portland Cement (OPC) and Type II fly ash specified in the JIS A6201 were used in this experiment. The water to binder ratio was fixed at 0.5 for flexural crack specimens and 0.6 for the crack that was induced by splitting tensile test. The maximum aggregate size for all specimens was 1.7 mm with a density and absorption rate of 2.71 kg/m^3 and 2.5%, respectively. Fresh mortar was placed in steel molds with a size of 40 x 40 x 160 mm and then cured in water for 28 days for specimens with flexural crack and 3 months for specimens with splitting tensile crack.

Table 3.5 Mix proportion of cracked mortar specimens

Specimen ID	Max. Agg. size (mm)	W/B	S/B	FA/(OPC+FA)	28 days compressive strength (N/mm^2)	91 days compressive strength (N/mm^2)
Flexural test						
OPC-MR-50	1.7	0.5	2.5	0	45.7	-
FA-MR-50	1.7	0.5	2.5	0.3	31.8	-
Splitting tensile test						
OPC-MR-60	1.7	0.6	2	0	19.77	21.2
FA-MR-60	1.7	0.6	2	0.3	21.48	28.7

a. Flexural cracked specimen and diffusion test of oven-dried cracked specimen

In this specific study, the observation using micro-focus X-ray CT at Hokkaido University was performed in stages namely after generating the crack and after cesium tracer diffusion test. As shown in Figure 3.4, the mortar beam specimens with size of $10 \times 20 \times 60$ mm were prepared for the flexural test in order to induce crack in the specimen. Figure 3.5(a) shows the illustration of flexural test to generate the crack in the mortar beam specimens (OPC-MR-50 and FA-MR-50). FRP sheet was applied in order to avoid sudden break during the application of load. The residual crack widths (hereinafter crack opening width) in the specimens were planned to be around less than 50 μm. After unloaded, the cracked mortar beam specimens of OPC-MR-50 and FA-MR-50 were scanned by using micro-focus X-ray CT to obtain microtomographic images of the 3D crack. Furthermore, the specimens were oven dried before cesium tracer diffusion test.

Figure 3.5(b) shows the illustration of cesium tracer diffusion test. Cesium carbonate solution (Cs_2CO_3) with the solution concentration of 1.84 mol/L (40% mass concentration) as a tracer was prepared. The properties of Cesium carbonate solution (Cs_2CO_3) are shown in Table 3.6. These values were obtained through laboratory test of 1.84 mol/L cesium carbonate solution. Cesium carbonate solution (Cs_2CO_3) was considered feasible as the source of a tracer transport in crack space. This is due to the fact that cesium tracer exhibits relatively larger atomic number among an alkali metal family. Then, the presence of cesium can be traced by its larger CT numbers as compared with those of cement paste and aggregate in concrete. In order to prevent diffusion in lateral direction, side-surfaces of the specimens were sealed by using ordinary insulation tape. Subsequently, after 24 hours of cesium tracer diffusion test, the specimens were removed and scanned by using micro-focus X-ray CT.

Table 3.6 Properties of cesium carbonate solution (Cs_2CO_3) of 1.84 mol/L

Properties of Cs_2CO_3	
Density of powder	4.07 g/cm^3
Solubility in water	2605 g/L
Contact angle	26.5^o
Surface tension	72.6 dyn/cm
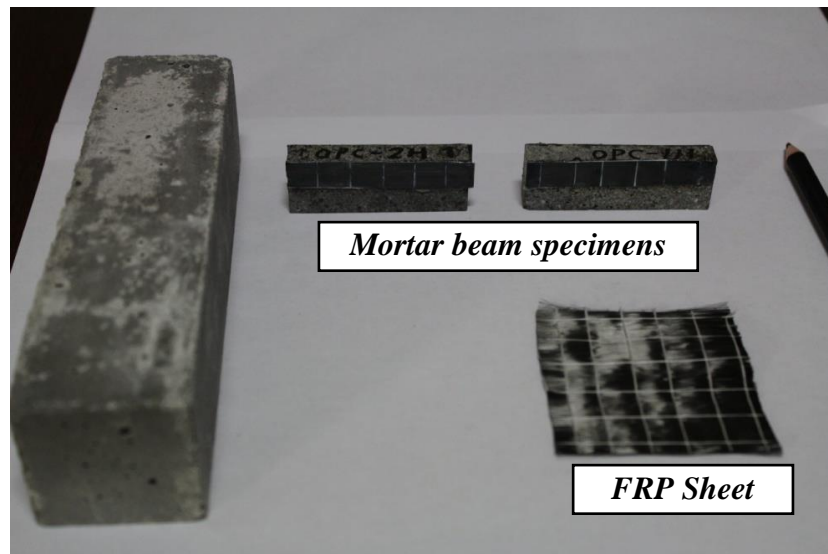
Figure 3.4 Preparation of mortar beam for flexural test.
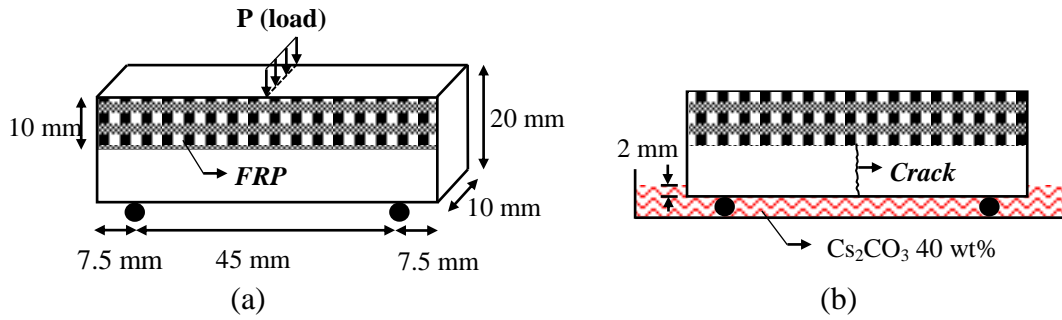
Figure 3.5 Experiment set-up (a) Flexural test to generate the crack in mortar beam specimen (b) Cesium tracer diffusion test.

b.   Splitting tensile cracked specimen and diffusion test of partially saturated cracked specimen

As shown in Figure 3.6, cylindrical specimens of 20 mm in diameter and 40 mm in length were obtained from mortar blocks (OPC-MR-60 and FA-MR-60) after 3 months of curing periods for splitting tensile cracked specimens. For diffusion test, the diffusion of tracer was planned to occur in one of the cutting faces of the specimen, heat-shrinkable tube, therefore, was used to cover the lateral surface of the cylindrical specimen. Heat-shrinkable tube was used not only to prevent initial diffusion from the surface in the lateral direction but also to avoid sudden failure during the splitting tensile test.

Controlled splitting tensile tests were then used to induce cracks in the specimen of OPC-MR-60 and FA-MR-60 (see Figure 3.7). A clip gauge was installed on one of the cutting face of the specimen. When the crack opening displacement (COD) reached a certain specified value, the specimens were then unloaded. As the crack tends to close to a certain extent after unloading, repetitive tests were performed to obtain the target COD. Finally, residual crack widths (crack opening width) of 51, 127 and 152 μm were obtained at unloaded state as shown in Figure 3.8. Furthermore, the specimens were immersed in water for 24 hours after generating the crack to acquire saturated condition inside the crack space.
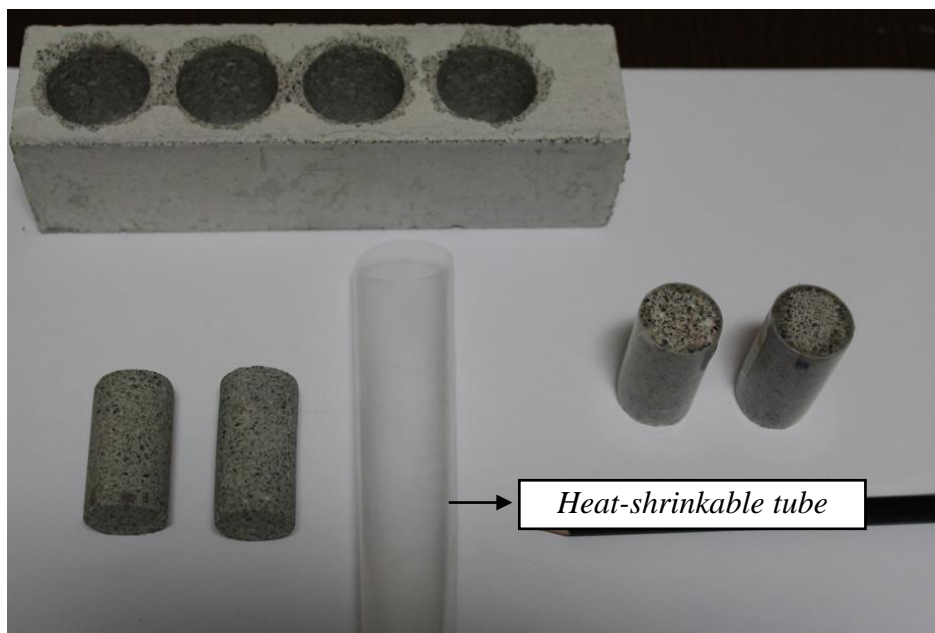
Figure 3.6 Preparation of cylinder mortar specimen.
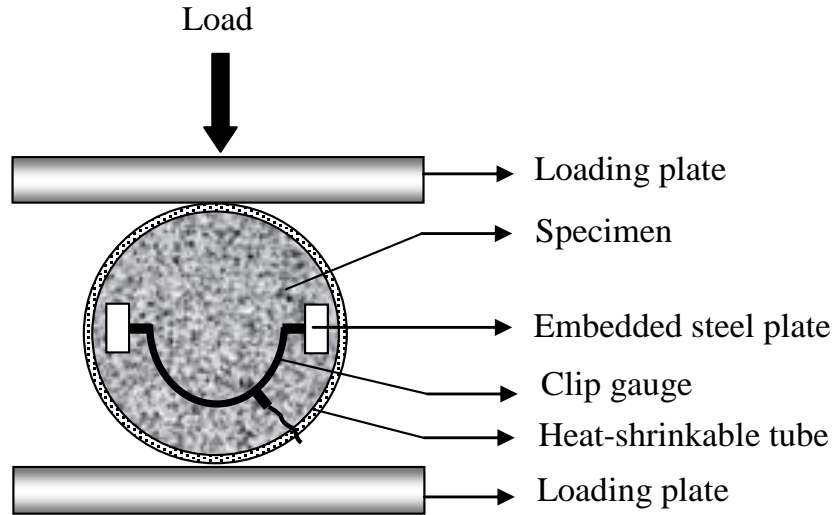
Figure 3.7 Splitting tensile test to induce the crack in the cylinder mortar specimen
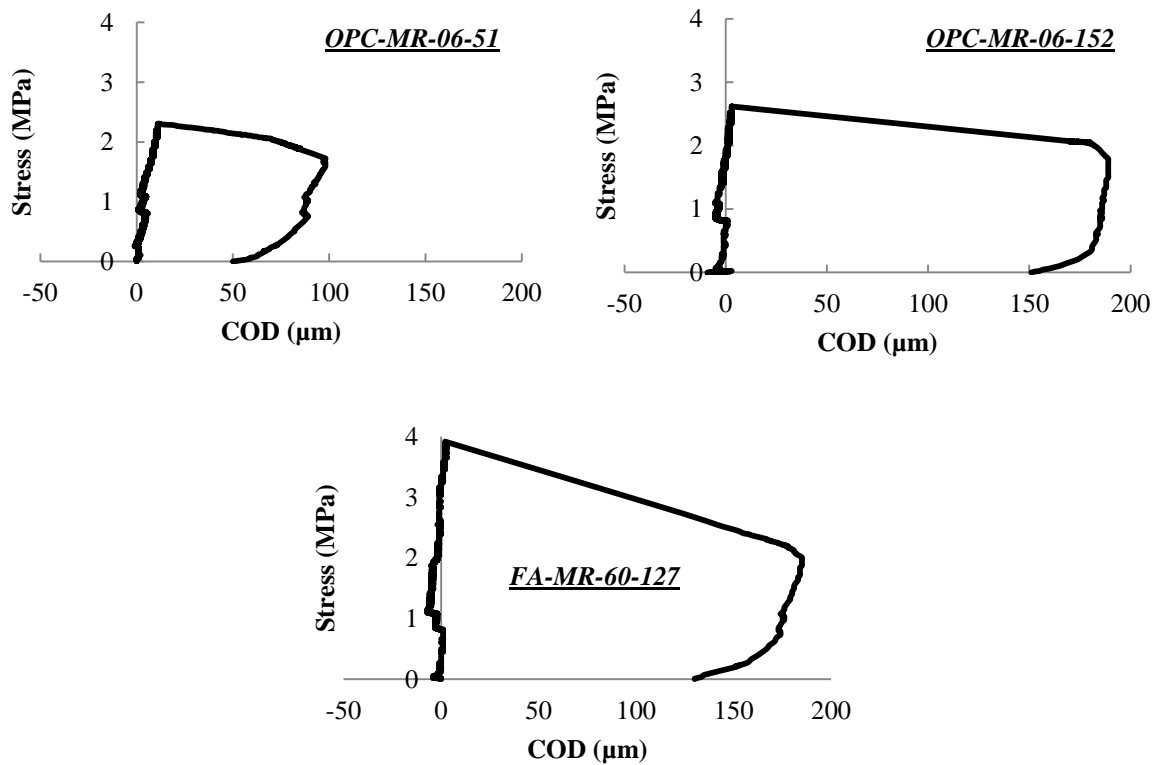
Figure 3.8 Tensile stress-COD curves of each specimen

After immersing in water for 24 hours, the cracked specimen was scanned by microfocus X-ray CT to obtain a set of the microtomographic images of the 3D crack. To prevent the water loss from the crack space during X-ray CT test, experimental set-up shown in Figure 3.9(a) was performed in which the bottom region in the specimen was continuously exposed to water. In addition, the cesium tracer diffusion tests were conducted in-situ inside the X-ray CT machine. Then, the focus area for data acquisition was adjusted to the focus area in solution-exposed specimen as far as 2 mm to 18 mm from the surface that was exposed to the solution.
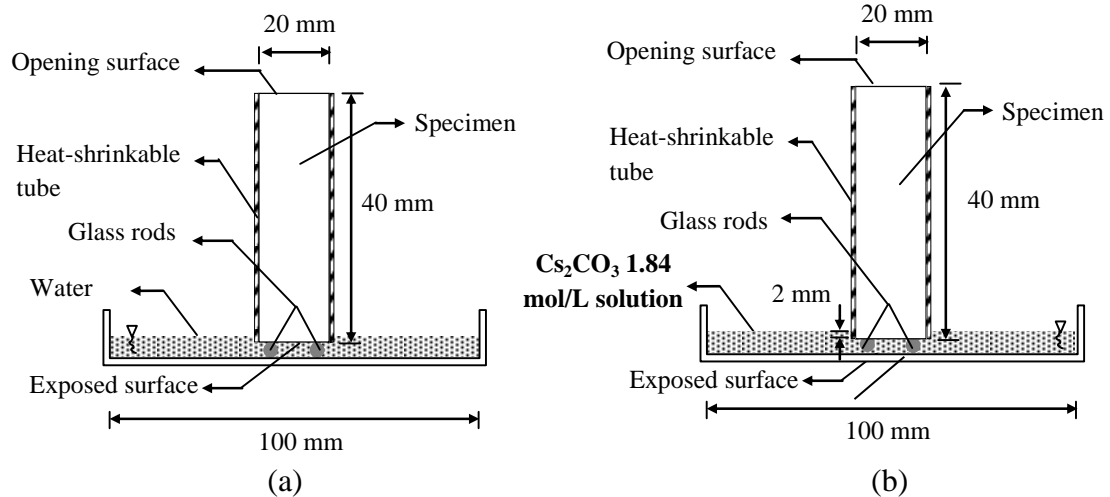
Figure 3.9 Schematics of diffusion test set-up (a) initial condition (b) diffusion test.

After scanning the specimen of its initial condition (OPC-MR-06-51, OPC-MR-152, and FA-MR-06-127); water was removed from the glass tray without changing its position in rotation stage of the microfocus X-ray CT. Then, a cesium carbonate solution (Cs_2CO_3) of 1.84 mol/L concentrations was poured into the glass tray until the specimen becomes submerged at a certain level. The level of the solution was 2 mm above its bottom edge as shown in the Figure 3.9(b). The exposure time in the solution was set as follows: 1, 3, 9 and 24 hours. In this way, the observation using X-ray CT during the initial condition and the subsequent diffusion test was conducted in-situ inside the X-ray CT machine.

3.2. IMAGE PROCESSING
3.2.1. Volume of interest (VOI)

Table 3.7 shows the specific size of volume of interests (VOI) used for image analysis in each type of investigation. The VOI size selection was based on the type of specimen used and the cross-sectional size of specimen that appears in the image. As stated by Uchikawa [82,83] that 100 micrometers is a representative size for studying cement pastes. Therefore, based on these literatures and cross-sectional image of the specimen, in the evaluation of pore structure in cement paste specimen by using synchrotron X-ray CT, a VOI with size of 400^3 voxels (200^3 μm^3) was selected.

For the evaluation of crack geometry in the cracked mortar, a bigger VOI size was selected in order to cover the whole crack in the cross-sectional image and to obtain more

Table 3.7 Volume of interest (VOI) selection for image analysis

Type of study	Type of Specimen	X-ray CT system	Voxel size (microns)	VOI size (voxel)
Evolution of pore structure	Cement paste	Synchrotron X-ray CT	0.5×0.5×0.5	400×400×400
Deteriorated cementitious materials				
- *Leaching*	Cement paste	Synchrotron X-ray CT	0.5×0.5×0.5	400×400×400
- *Fire exposure*	Concrete	Micro-focus X-ray CT	22×22×44	875×875×526
Cracked concrete				
- *Flexural Crack*	Mortar	Micro-focus X-ray CT	22×22×44	400×400×600
- *Splitting tensile crack*	Mortar	Micro-focus X-ray CT	22×22×44	600×600×600

complete information about the crack formation. On the other hand, considering the type of specimen used in the study of fire damage concrete and deterioration behavior occurred in the specimen, whole cross-sectional image of specimen exposed to fire condition was used as a VOI.

3.2.2. Extraction void space from microtomography images

The void space was then extracted from this VOI by thresholding the slice on the basis of their gray level histogram. For void space segmentation, global thresholding was used to separate the void from the "solid" matrix by defining the range of grayscale value (GSV) associated with void voxels. As described in Figure 3.10, the lower bound of GSV associated with void voxels was set to 0 while the upper bound is set to the void threshold value on the basis of transition point in segmented porosity-threshold dependency curve [10]. The output from this void segmentation is a set of binary images where the voids and solid matrix are imaged as black (GSV =0) and white voxel (GSV = 255), respectively. In addition, as there is no practical procedure yet to standardize pore segmentation from microtomographic images, which method is appropriate is still an open discussion. Some researchers define the void threshold value on the basis of grey level histogram alone while others define the threshold value on the basis of known experimental or theoretical porosity.

After pore segmentation, a basic 3D-image analysis program called SLICE [84], was used to obtain the largest percolating void and connectivity through cluster multiple labeling technique [85]. In this connectivity analysis [86,87], two voxels are defined as connecting voxels when both voxels share a common face as shown in Figure 3.11. This set of connected voxels forms a cluster. On the other hand, if the void voxels are in contact only at the vertex of edge, then the voxels are considered to be disconnected and belong to different cluster (Figure 3.11). This cluster multiple labeling allows us to identify and extract the largest void cluster from other smaller isolated void clusters. The output from the void cluster labeling enumerates the number of pore cluster and their size (number of voxels) including their end-to-end coordinate in the cubic image system [10].
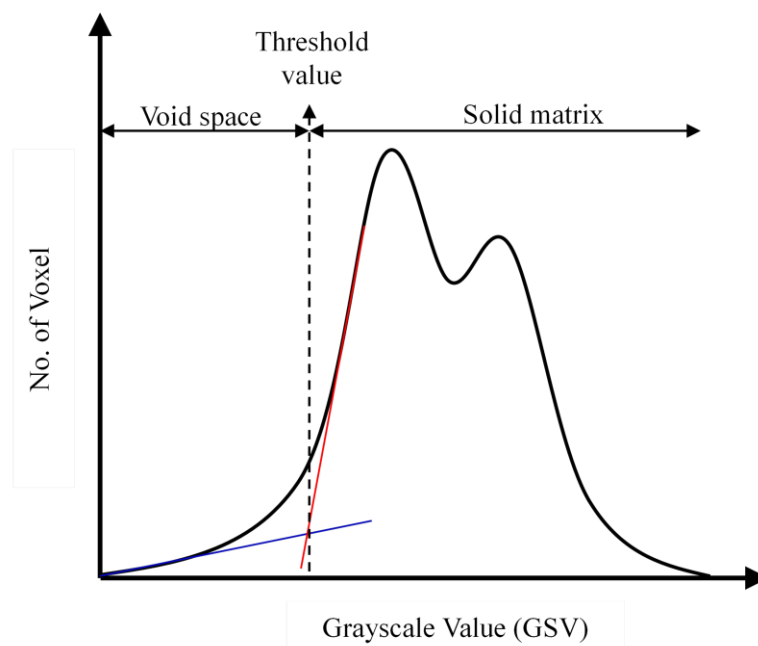
Figure 3.10 Example of GSV histogram for VOI and corresponding porosity-threshold dependency curve.
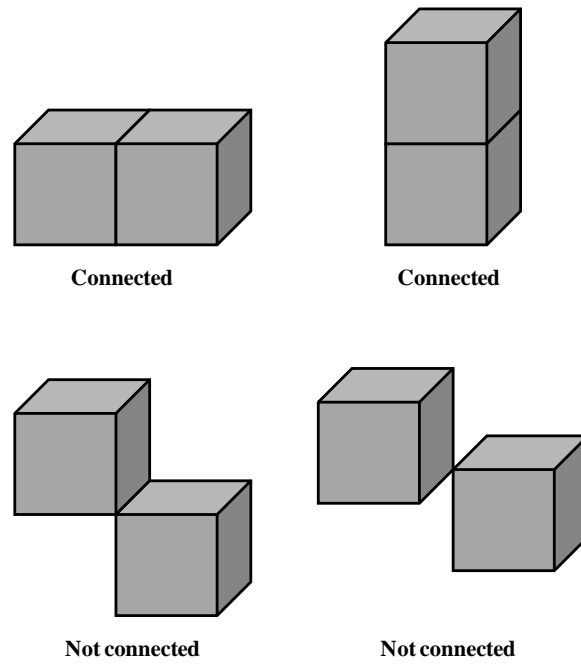
Figure 3.11 Definition of connection of void voxels in the three-dimensional image.

Figure 3.12 shows the illustration of quantification of percolated porosity and isolated porosity through cluster multiple labeling. Percolated porosity was obtained by checking the end-to-end coordinate of any void clusters after cluster multiple labeling. In this study, criterion to define percolation adopted the percolation criterion reported by Promentilla et al
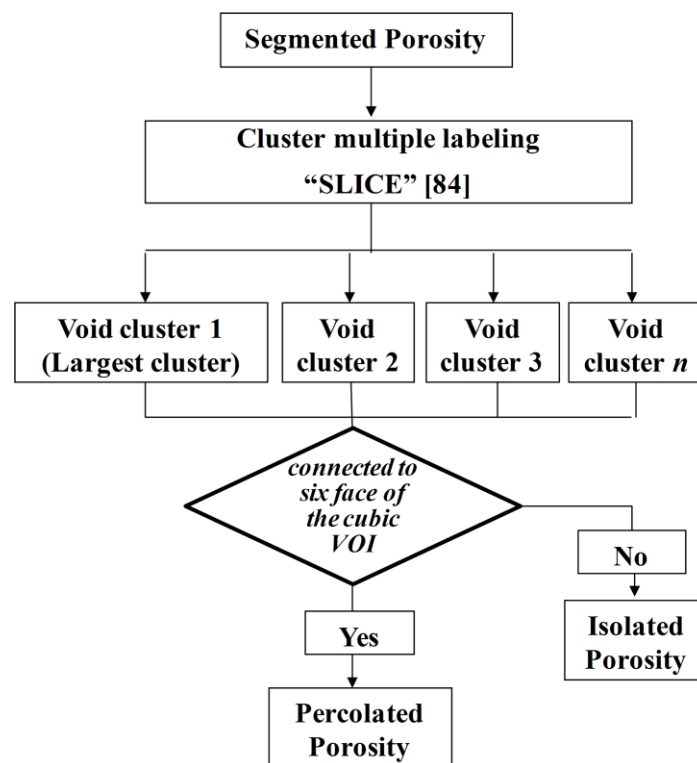
Figure 3.12 Illustration of quantification of percolated and isolated porosity.

[10] in which void cluster contains voxels that are connected to the six faces of the cubic VOI was defined as percolating void cluster. Usually, the largest void cluster obtained from cluster multiple labeling technique is a percolated porosity. Meanwhile, the rest of void cluster was then defined as isolated porosity. In other words, isolated porosity was calculated by subtracting segmented porosity to the percolated porosity. In addition, the degree of void connectivity was evaluated by determining the fraction of the largest void cluster and percolates along the three orthogonal directions (x, y and z-axis) to the volume of segmented porosity [10]:

$$Connectivity = \frac{Volume\ of\ percolated\ void}{Volume\ of\ segmented\ porosity} \tag{3.1}$$

On the other hand, in order to extract the crack space in the microtomographic image obtained from microfocus X-ray CT the following procedure as shown in Figure 3.13 was used. After void space segmentation the void space which consists of pore and crack can be easily distinguished from solid. Furthermore, through cluster multiple labeling the largest void cluster is separated from other smaller isolated void clusters. For the case of microtomographic images of cracked specimen, the largest void cluster which percolated only in two orthogonal direction (z and x-axis or z and y-axis) represents the crack space. Finally, after second segmentation process of binary image, the 3D crack space was obtained.
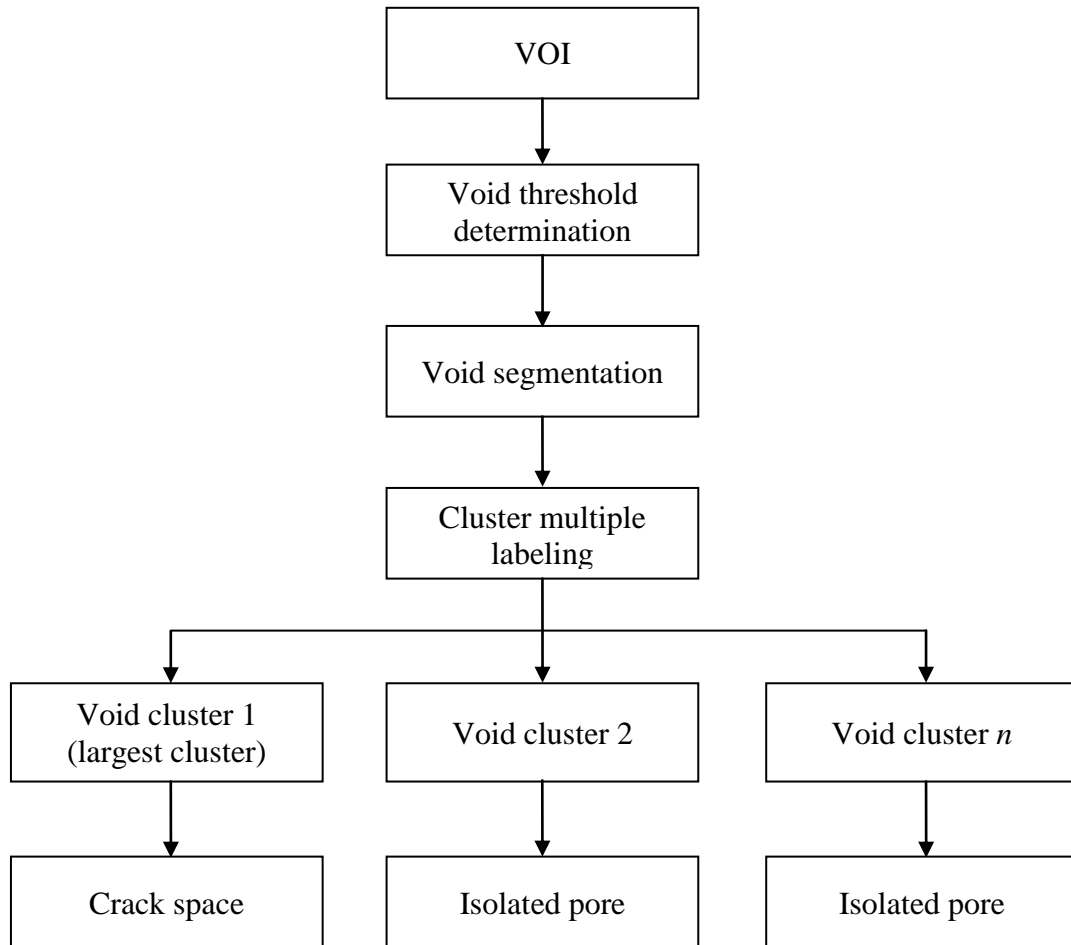
Figure 3.13 Procedure of extraction of crack space from microtomographic images.

3.2.3. Methodology to determine each solid phase based on measured LAC histogram

As reported by Tsuchiyama et al [88], the voxel intensities or grayscale values (GSV) in slice correspond to the CT values or CT numbers which are proportional to the measured linear attenuation coefficient (LAC) of X-rays provided by the tomographic reconstruction program used at SPring-8. In other word, GSV provided by the tomographic reconstruction program used at SPring-8 directly estimates LAC. Thus, hereafter, the CT values or LAC derived from tomographic reconstruction is called observed LAC, whereas theoretically calculated LAC is called theoretical LAC. The theoretical LAC of a sample was calculated using the following equation [89]:

$$theoritical\ LAC\ (\mu) = \rho \sum_i w_i \tau_i(E) \tag{3.2}$$

where ρ is the bulk density, w_i is the weight fraction of the i-th element, and τ_i is the mass attenuation coefficient of the i-th element at a given X-ray energy (E) from NIST database [90].

However, the observed LAC, f_p, as reported by Tsuchiyama et al [88] is slightly smaller than the theoretical LAC and followed the following equation as long as $f_p < 400$:

$$f_p = (0.892 \pm 0.004) \times \mu \tag{3.3}$$

Table 3.8 provides the LAC values of the phases of interest for hardened cement paste in descending order of their observed LAC at X-ray energy level of 15 keV and 25 keV.

3.2.4. Local thickness algorithm for determining void size distribution

After obtaining the largest cluster, the *Thickness* plugin in BoneJ [95,96], which is a set of public-domain plugins used for geometry and shape analysis of CT images originally

Table 3.8 Observed LAC values of the phases of interest for hardened cement paste at X-ray energy level of 15 keV and 25 keV.

Phase	Chemical Formula	Density, ρ (g/cc)	Observed LAC, f_p (cm^{-1})	
			15 keV	25 keV
Magnetite	Fe_3O_4	5.15 [91]	196.17	46.30
Hematite	Fe_2O_3	5.30 [91]	189.91	45.53
Ferrite	$(CaO)_4(Al_2O_3)(Fe_2O_3)$	3.73 [92]	81.31	19.48
Alite	$(CaO)_3(SiO_2)$	3.21 [92	50.41	12.01
Belite	$(CaO)_2(SiO_2)$	3.28 [92]	47.49	11.35
Aluminate	$(CaO)_3(Al_2O_3)$	3.03 [92]	41.90	10.03
Portlandite	$Ca(OH)_2$	2.24 [92]	33.82	8.10
Calcium Silicate Hydrate				
- *C-S-H I*	$(CaO)_5(SiO_2)_5\ 6H_2O$	2.25 [18]	23.43	5.70
- *C-S-H II*	$(CaO)_9(SiO_2)_5\ 11H_2O$	2.35 [18]	52.69	9.64
- *14Å Tobermorite*	$Ca_5Si_6O_{16}(OH)_2 \cdot 7H_2O$	2.23 [93]	23.59	5.77
- *Jennite*	$Ca_9Si_6O_{18}(OH)_6 \cdot 8H_2O$	2.33 [93]	39.14	9.49
Quartz	SiO_2	2.65 [94]	13.70	3.50
Ettringite	$(CaO)_3(Al_2O_3)(CaSO_4)\ 32H_2O$	1.70 [92]	12.78	3.20
Water	H_2O	1.00	1.50	0.53
Air	-	0.001	0.00	0.00
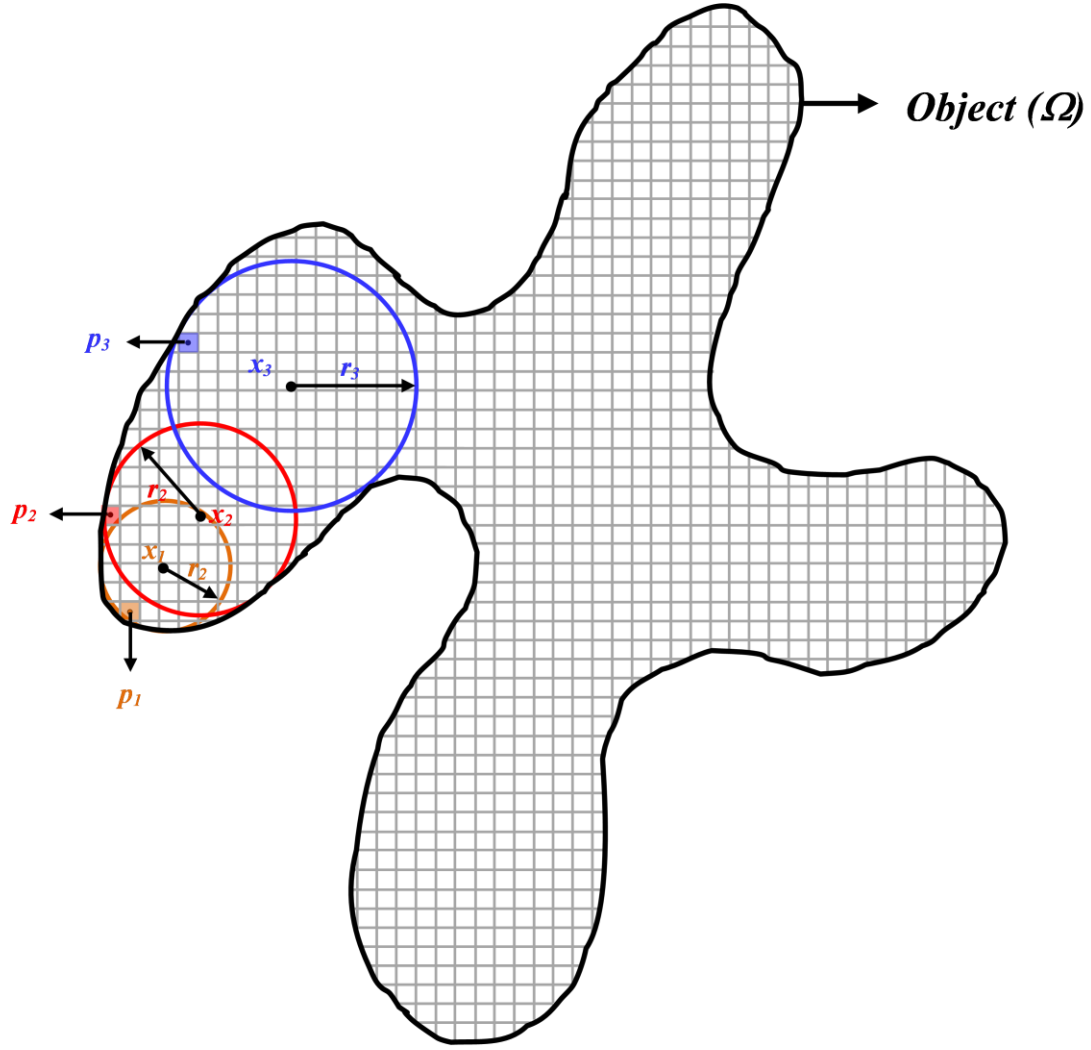
Figure 3.14 Illustration of *Thickness* algorithm.

designed for bone tissue, was performed to determine the pore size distribution in connected pore structure as well as crack width distribution in crack network. The operational definition of *Thickness* is based on the following equation [97,98].

$$\tau(p) = 2max(\{r|p \in sph(x,r) \subseteq \Omega, x \in \Omega\}) \tag{3.4}$$

where $\tau(p)$ is the diameter of the largest sphere that fits inside the object and contains the point (p). Let $p_i \in \Omega$ be the set of an arbitrary point (1 unit voxel) in the object (Ω) (Figure 3.14), which is defined as pore space in pore structure and crack space in crack structure. Subsequently, create the largest spheres with center x and radius r which contains the point 'p_i' and completely inside the object (Ω). The thickness $\tau(p_i)$ which is the diameter ($2r_{max}$) of the largest sphere is defined as the pore size in pore structure and crack width in this 3D crack analysis. Furthermore, from point 'pi' which represent 1 unit voxel we will have one data corresponding to the thickness of the object. This algorithm will continue to run until all the points (voxels) covered in the object (Ω). Finally, the information regarding the thickness (diameter) and its volume in object will be obtained. The output of *Thickness* plugin is the thickness of a 3D object which is displayed in the form of a thickness distribution and thickness map as shown in Figure 3.15 (a) and (b) for the case of pore space and Figure 3.15 (c) and (d) for the case of crack space.

34
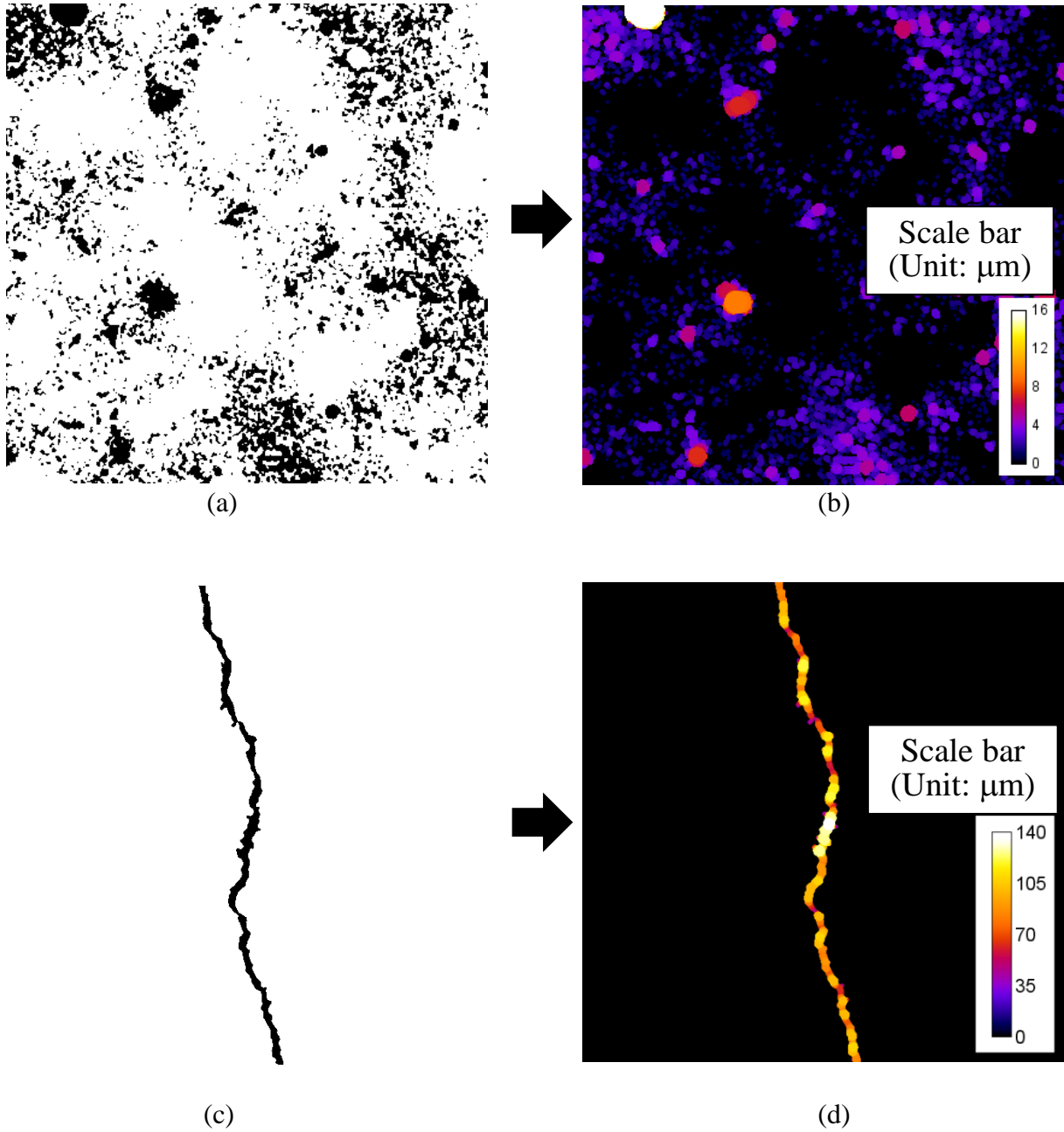
Figure 3.15 The output of *Thickness* plugin in (a) segmented pores were defined as (b) pore size distribution while when *Thickness* plugin in performed in (c) segmented crack space the output was defined as (d) crack width distribution.

3.2.5. Methodology to determine crack geometry parameter

In order to clarify the relationship between crack geometry and diffusion of solute in crack, the crack geometry parameter was first quantified using 3D image analysis. In this study, the crack geometry parameters are defined as geometric tortuosity, and constrictivity. Geometric tortuosity is defined in this study as the ratio of tortuous crack length (l_e) to the nominal crack length (l) as shown in Figure 3.16.

$$\tau = \frac{l_e}{l} \tag{3.5}$$

$$Tortosity\ (\tau) = \frac{l_e}{l}$$
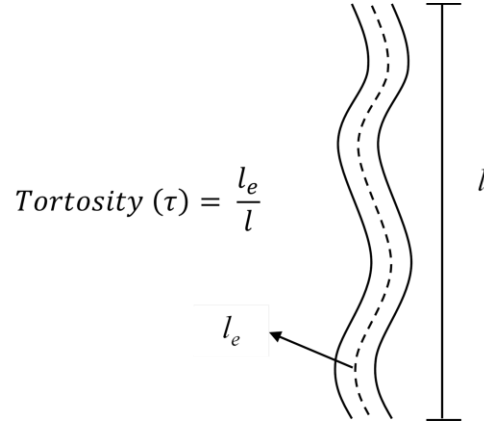
Figure 3.16 Definition of tortuosity.

Figure 3.17 shows the methodology to determine crack geometric tortuosity in the 3D artificial crack with VOI size of 600^3. In a volume of interest (VOI) of 600^3 voxels, the nominal crack length (l) is equal to 600 pixels (see Figure 3.17(a)). Meanwhile, in order to determine the tortuous crack length of 3D crack space of each specimen, skeletonization of 3D crack slice with a thickness of $\varDelta y$ (1 unit) pixel as show in Figure 3.17(b) was applied.
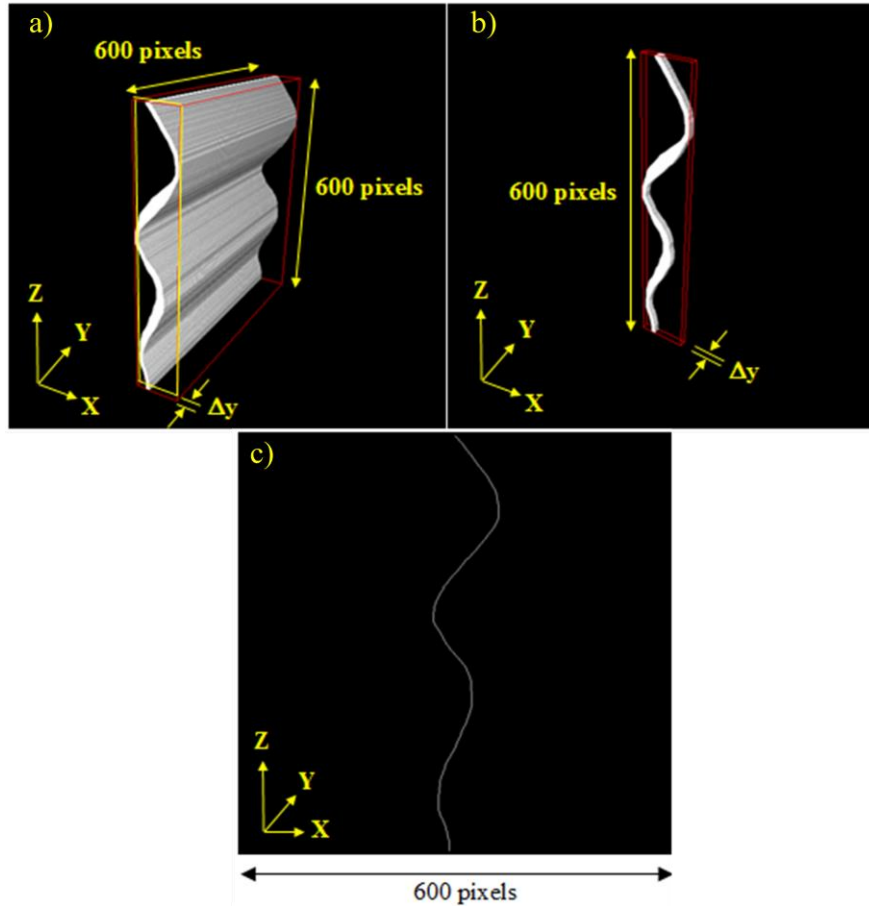
Figure 3.17 Determination of 3D crack geometry (a) 3D artificial crack (b) Crack slice with a thickness of Δy pixels,(c) Skeleton image of crack for *AnalyseSkeleton*.
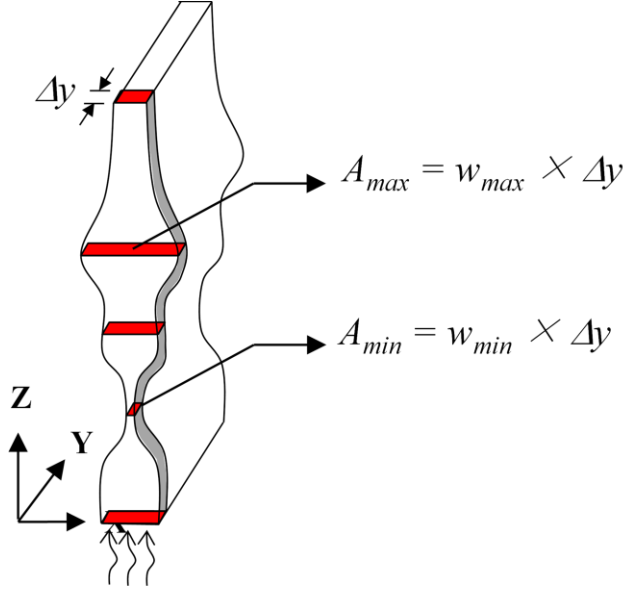
Figure 3.18 Definition of crack constrictivity.

Skeletonization is a repeatedly process to remove pixels from the edges of objects in a binary image until they are reduced to single-pixel-wide shapes as shown in Figure 3.17(c). This algorithm was implemented using one of the BoneJ plugins known as *AnalyseSkeleton* [99]. *AnalyseSkeleton* was used for measuring tortuous crack length. This plugin tags all pixels or voxels in a skeleton image and then counts all branches, and measures their length. Subsequently, the tortuous crack length (l_e) is then approximated by the total branches (pixels).

Another important parameter in crack is its constrictivity. The constrictivity, δ, accounts for the fact that the cross section of crack varies over its length. Figure 3.18 shows the definition of crack constrictivity. For the crack that has perfectly uniform in crack width, the constrictivity is 1. On the other hand, the constrictivity less than 1 indicates there is a gap between its crack widths. The constrictivity of the crack path can then be defined as follows [100,101]:

$$\delta = \frac{(Maximum \times minimum\ cross-section)^{\frac{1}{2}}}{mean\ cross-section} \qquad (3.6)$$

Mean cross section could be evaluated by linear approximation with average of maximum and minimum cross section. Subsequently, by analogizing that crack is composed of "crack slice" with a thickness of Δy pixels, as shown in Figure 3.18, the constrictivity could be calculated as follows:

$$\delta = \frac{((w_{max} \times \Delta y) \times (w_{min} \times \Delta y))^{\frac{1}{2}}}{\frac{1}{2}((w_{max} \times \Delta y) + (w_{min} \times \Delta y))} \qquad (3.7)$$

$$\delta = \frac{(w_{max} \times w_{min})^{\frac{1}{2}}}{\frac{1}{2}(w_{max} + w_{min})} \qquad (3.8)$$

where w_{max} is the maximum crack width and w_{min} is the minimum crack width which are obtained from *Thickness* plugin.

3.2.6. Quantification of diffusion tortuosity from random walk simulation (RWS) in 3D pore space

After extracting the largest percolating pore space, random walk simulation was performed in the 3D pore space to probe the pore geometry and quantify the diffusion tortuosity. Diffusion tortuosity is defined as the ratio of self-diffusion coefficient (D_o) of non-sorbing walkers in the free space to the long time self-diffusion coefficient (D_∞) of these walkers in pore space [10,11].

The operational definition of the time-dependent self-diffusion coefficient ($D(t_d)$) in a 3D lattice space is based on the following equation [102]:

$$D(t_D) = \frac{1}{6} \frac{d\langle r^2 \rangle}{dt_d} \tag{3.9}$$

where $\langle r^2 \rangle$ and t_d refer to the mean square displacement of the walkers and dimensionless lattice walk time, respectively. In a simple cubic lattice, the mean square displacement is computed as follows:

$$\langle r(t_D)^2 \rangle = \frac{1}{n} \sum_{i=1}^{n} \left[\left(x_i(t_D) - x_i(0) \right)^2 + \left(y_i(t_D) - y_i(0) \right)^2 + \left(z_i(t_D) - z_i(0) \right)^2 \right] \tag{3.10}$$

where n is the number of walkers, and x, y, and z are the 3D coordinates of the walker's position at time t_D for the i-th walker.

Accordingly, the diffusion tortuosity (τ_D) can be defined as follows:

$$\tau_D = \frac{\left(\frac{d\langle r^2 \rangle}{dt_d} \right)_{free\ space}}{\left(\frac{d\langle r^2 \rangle}{dt_d} \right)_{pore\ space}} = \frac{D_o}{D(t_D \rightarrow \infty)} = \frac{D_o}{D_\infty} \tag{3.11}$$

In this study, a 3D random walk algorithm implemented in Mathematica was employed to compute the mean square displacement of random walkers in a simple cubic lattice with mirror boundaries [102].

3.3. DETERMINATION OF DIFFUSION COEFFICIENT IN CRACK AND UNCRACKED MATRIX

3.3.1. Measurement of solute concentration

Generally, in order to determine the diffusion coefficient of solute both inside the crack and perpendicular to the crack wall (through the uncracked body), the concentration profile of solute should be quantified. In this study, the unique approach to determine Cs_2CO_3 concentration appeared in microtomographic images was based on CT number. It should be noted that CT number is strongly correlated with density of solid material as well as concentration of solution. Therefore, a calibration to describe the relationship between CT number and solute concentration is needed.

Furthermore, in order to determine the relationship between changes in CT number and Cs_2CO_3 concentration, preliminary test was conducted as follows. A capillary-glass tube with 2 mm diameter and 50 mm length was filled with 0 (water), 0.003, 0.030, 0.340 and 1.840 mol/L of cesium carbonate (Cs_2CO_3) solution. From the X-ray scan, the cross-sectional images of those solutions inside a capillary-glass tube were obtained as shown in Figure 3.19(a) to (e). The CT images in Figure 3.19 clearly show that the higher the concentration, the larger the contrast is.
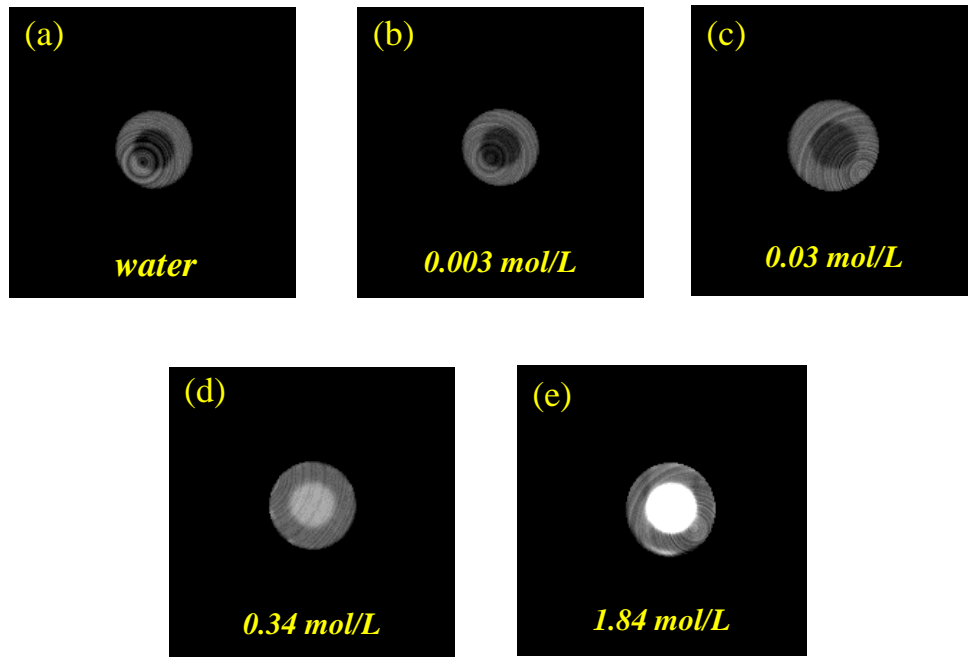
Figure 3.19 Visualization of representative cross-sectional images of a capillary-glass tube filled with (a) water, (b) 0.003 mol/L, (c) 0.03 mol/L, (d) 0.34 mol/L, (e) 1.84 mol/L Cs_2CO_3 solution.

From the analysis of CT number, the average of CT number of each solution was obtained. Subsequently, the difference between CT number of each solution and CT number of water is called ΔCT number. The ΔCT number indicates the change in concentration due to the presence of tracer in solution. Figure 3.20 shows the relationship between ΔCT number and tracer concentration. It can be seen that the ΔCT number is a linear function of tracer concentration. Note that such calibration of CT numbers to the density of the object has been performed by several researchers, especially for bone tissues [103,104].
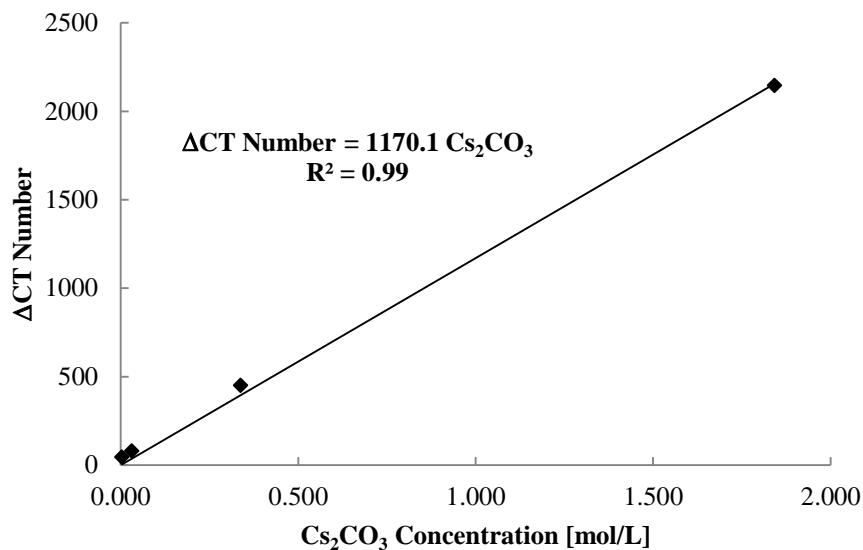
Figure 3.20 Relationship between CT number and Cs_2CO_3 concentration.

Furthermore, after obtaining the relationship between CT number and Cs_2CO_3concentration, the determination of Cs_2CO_3 concentration in microtomographic images of the specimens was conducted as follows. First, a specific slice at the represented height from the solution contact-exposed surface was chosen from the whole stack of

(a)   (b)

(c)   (d)

(e)   (f)
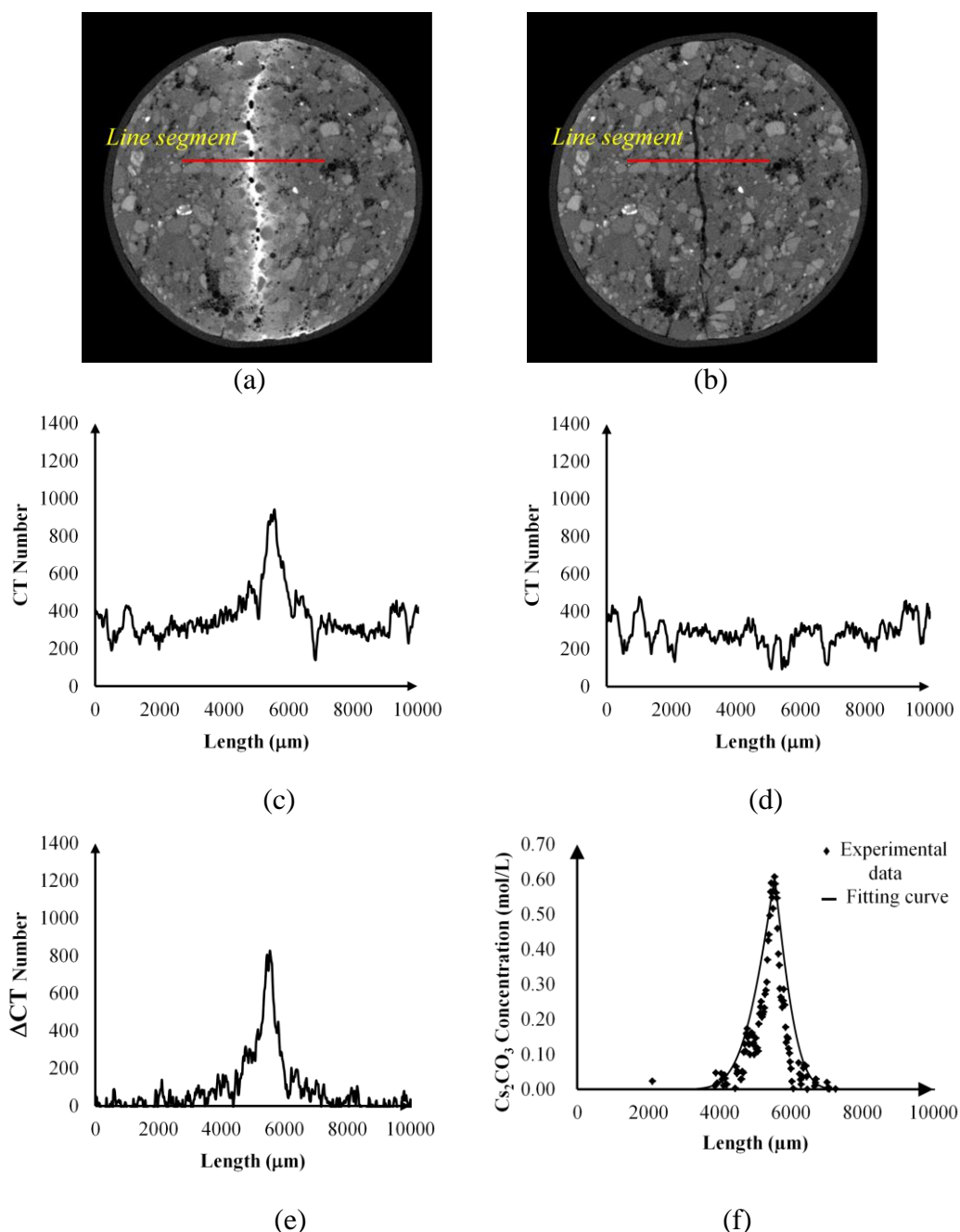
Figure 3.21 A method to determine diffusion coefficient from microtomographic image (OPC-MR-60-152) (a) Line segment is applied at crack filled by tracer in exposed condition, (b) Line segment, which has the same coordinate in initial condition with those of (a), is applied, (c) CT number profile of line segment in solution-exposed condition, (d) CT number profile of line segment in initial condition, (e) Subtracted CT number profile to obtain changes in CT number (ΔCT number) due to diffusion of tracer, (f) Tracer concentration profile.

reconstructed slices both in initial and solution-exposed condition. Then, a total of 10 regions of interest of crack filled with tracer were specified. Line segments which intersect perpendicularly to the crack were applied in these regions and were carried out at the same crack section both in initial and solution-exposed condition. The profile of CT number was obtained from each line segment and then compared between those values in initial and solution-exposed condition.

Subtraction between CT number profiles at the same region of cracks in both conditions was done to compute the CT number difference (ΔCT number) due to tracer diffusion in the cracked mortar. Based on the calibration between ΔCT number and tracer concentration shown in Figure 3.20, the average of the maximum ΔCT number was converted into the tracer concentration. Using the said method for the specific position of the exposed surface, tracer concentration profiles along the crack were obtained. It should be noted that this method can only be applied if the position and size of the cross section of the specimen in reconstructed slices are the same in both conditions. Such condition in the experiment was achieved as there was no change in the position of the specimen on the rotating stage at both initial condition and solution-exposed condition.

Figures 3.21 (a) to (f) illustrate an example to obtain the distribution of tracer concentration values in the crack space at a certain elevation from the surface exposed to the solution based from a given line profile (OPC-MR-60-152). Note that the line segments in Figure 3.21(a) and (b) were a representative segment selected from among the 10 total segments which were analyzed. From Figure 3.21(f) the tracer concentration in the crack was determined to 0.61 mol/L. This concentration is lower than the solution concentration of 1.84 mol/L. It means that the diffusion process occurs along the crack passage. The same method was applied to determine the concentration in the crack of OPC-MR-60-152and FA-MR-60-127 at the height of 5, 9, 13 and 17 mm from the surface exposed to the solution. However, for the case of OPC-MR-60-51, determinations of tracer concentrations were conducted at 4, 5, 6 and 7 mm from the surface exposed to the solution. For farther position, the contrast level of crack in the solution-exposed condition was similar to that of initial condition. It was then difficult to select regions of crack filled by tracer for line profile applications.

In the case of OPC-MR-50 and FA-MR-50, the determinations of tracer concentration were conducted at 2, 4, 6, 8 mm from the surface exposed to the solution. Basically there is no provision in selection of specific height from the surface exposed to the solution for determining tracer concentration. It was just based on the presence of tracer in the microtomographic images at those specific heights as well as the ease of further analysis.

3.3.2. Diffusion coefficient along the crack

Diffusion due to a concentration gradient in one dimension can in general be described by Fick's second law of diffusion as follows:

$$\frac{\partial C}{\partial t} = D \frac{\partial^2 C}{\partial x^2} \tag{3.12}$$

By solving the Fick's second law under proper boundary conditions the penetration of the diffusing species is then described by the following equations:

$$\frac{C - C_0}{C_s - C_0} = 1 - erf\left(\frac{x}{2\sqrt{Dt}}\right) \tag{3.13}$$

where C is the concentration of the diffusing species at penetration distance x at time t, C_s is the constant surface concentration, and C_0 is the initial concentration of the diffusing species

already present in the bulk phase. *D* is the diffusion coefficient of the diffusing species and *erf* is the error function. The diffusion coefficient along the crack is determined from the best-fitted curve represented by Eq.(3.13) for the measured tracer concentration profile along the crack.

3.3.3. Diffusion coefficient perpendicular to the crack wall

As describe in Section 3.3.2, similar method was applied to evaluate diffusion coefficient perpendicular to the crack wall (through the uncracked body). In the determination of the diffusion coefficient along the crack, we used the average of the maximum ΔCT number profiles, while in the determination of diffusion perpendicular to the crack wall, the whole ΔCT number profile is used. The ΔCT number profile completely shows the tracer concentration profile through the uncracked body of the mortar at specific height from the solution-exposed surface. The diffusion coefficient perpendicular to the crack wall then was determined from the best-fitted curve represented by Eq.(3.13) from the measured tracer concentration profile.

3.4. SUMMARY

Low alkali cement paste specimen with a composition of 40% OPC, 20% silica fume and 40% fly ash and water to binder ratio of 0.5 was prepared with increased curing periods from 2 days to 146 days and after leaching test for 13 weeks for synchrotron X-ray CT with resolution of 0.5 µm/voxel at SPring-8, Japan. As a comparison, normal cement paste specimen was also prepared in similar manner.

High strength concrete of a water cement ratio of 0.3 was prepared to investigate the change of pore structure due to high temperature exposure followed by different re-curing method. Re-curing either in water or in air was carried out for one and four weeks. In the study of deteriorated cementitious materials due to mechanical loading, synchrotron X-ray CT was combined with micro-tensile instrument and the observation during the application of load conducted in-situ inside synchrotron X-ray CT chamber.

Micro-focus X-ray CT was employed to observe cracked mortar specimens due to mechanical loading. The cracks in beam specimens of the size of 10 x 20 x 60 mm and cylinder specimens of the size of 20 mm in diameter and 40 mm in height were induced by flexural test and splitting tensile test, respectively. Subsequently, the 3D crack geometry was obtained from microtomographic images. The transport mechanism in cracked mortar specimen was clarified by employing micro-focus X-ray CT coupled with in-situ tracer diffusion test. Furthermore, the cesium tracer concentration both in crack space and uncracked matrix was calculated on the basis of profile of CT number. Then, the diffusion coefficient was determined by best-fitted curve of Fick's second law.

The image analysis to extract voids in the microtomography images was explained with the method of a threshold on the basis of their grey level histogram. Furthermore, after void segmentation, a basic 3D-image analysis program called SLICE, was used to obtain the largest percolating void and connectivity through cluster multiple labeling technique. As for pore structure analysis, *Thickness* plugin and Random Walk Simulation were performed in 3D pore structure to examine the pore size distribution and its diffusion tortuosity, respectively. Meanwhile, for extracting the 3D crack from microtomography images of cracked specimen, Skeletonize process was explained with regard to the measurement of tortuous crack length. It was also explained that the *Thickness* plugin was also applied to the 3D crack analysis in order to determine crack width distribution as well as its constrictivity factor.

CHAPTER 4
VISUALIZATION OF VOID STRUCTURE

4.1. PORE STRUCTURE EVOLUTION WITH INCREASING CURING PERIODS
4.1.1. Porosity

After X-ray CT scans of each specimen by using synchrotron X-ray Computed Microtomography at SPring-8, Japan, the stack of the reconstructed slices were obtained. The stack of these slices provides the reconstructed volumetric data set of scanned object. The reconstructed 3-D image data set was composed of 1300 contiguous grayscale images where each slice image contained 2000×2000 voxels. The effective size of a cubic voxel in the CT image is 0.5 μm. Figure 4.1 shows the representative cross-sectional images of OPC-CP-50 and HFSC-CP-50 specimen at 2, 7, 28 and 146 days curing periods. In these images, the presence of pores in the cross-sectional images of specimens can be distinguished with solid products. The pores are imaged as very dark voxels corresponding to the background color of the image. Meanwhile, the brighter voxels are considered as solid product in the object.

Visually, with enough effort, we may be able to observe changes in total porosity that occurred in each type of specimen with increasing curing periods. In this state, however, it is a little bit difficult to distinguish the pore space inside the cross-sectional specimen due to some black regions which represent pore space surrounded by low density of solid phases and its color looks similar with pore space and this condition may lead to different perceptions between each observer. Furthermore, in order to enhance the presence of pores in the cross-sectional images, the black color in the cross-sectional image was changed to red color as well as the background color. The changes in black region which represent pores space certainly based on the pore threshold value of each specimen on the basis of transition point in the segmented porosity-threshold dependency curve [10], as describe in Figure 4.2. Figure 4.3 shows the results of cross-sectional images of specimens in which red color was used to indicate the presence of pore.

	2 days	7 days	28 days	146 days
OPC-CP-50				
HFSC-CP-50				
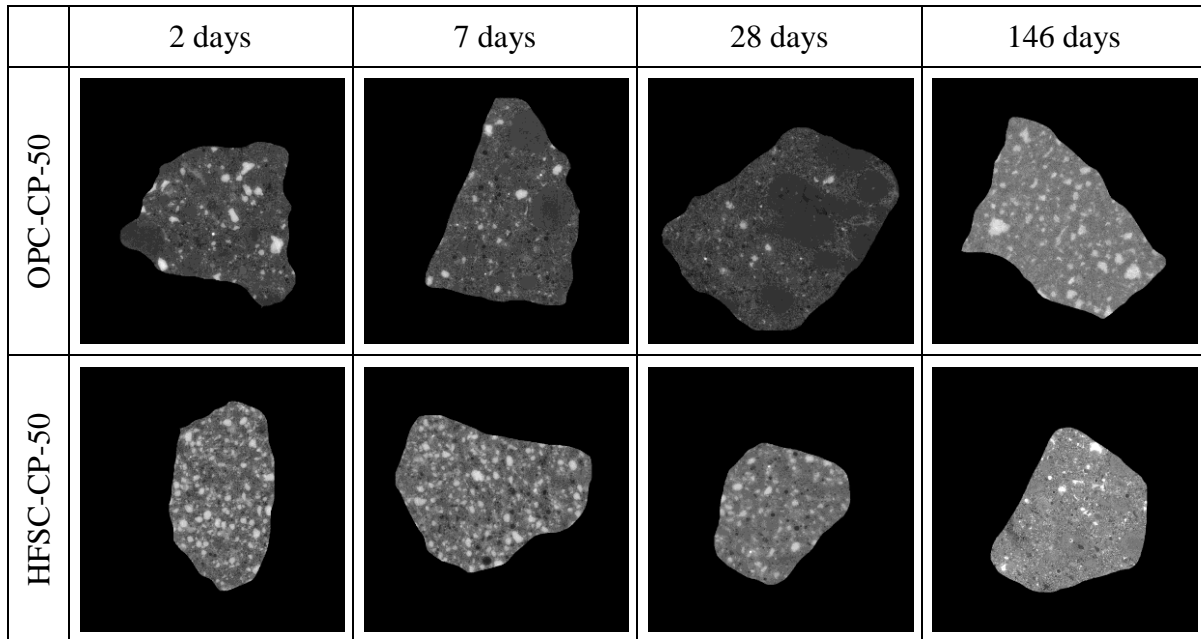
Figure 4.1 Representative cross-sectional images of OPC-CP-50 and HFSC-CP-50 with increasing curing periods.
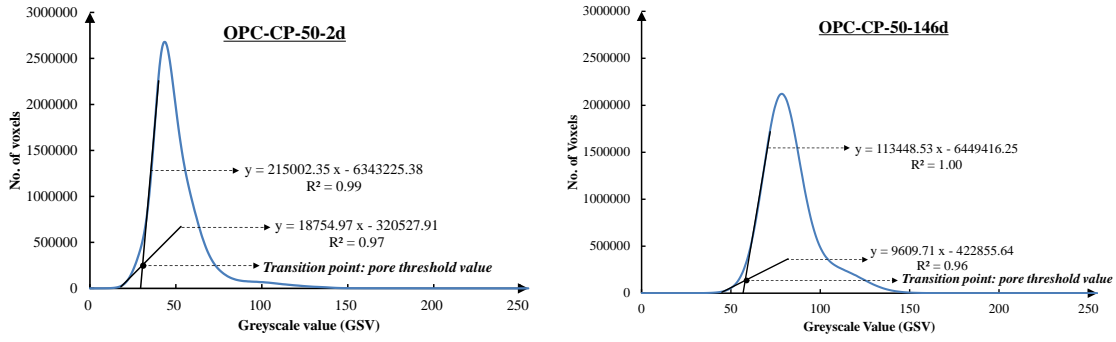
Figure 4.2 Example of GSV histogram for OPC-CP-50-2d and OPC-CP-50-146d and corresponding porosity-threshold dependency curve.

As shown in Figure 4.3, the amount of red color in the cross-sectional image of specimen was reduced with increasing curing periods. It is certainly not surprising because with increasing the age of cementitious material, more solid product formed through the hydration process and through pozzolanic reaction for the addition of mineral admixture such as fly ash and silica fume. The hydration products will then fill the gaps nearby and reduce the pore space in the microstructure of cementitious materials. However, just based on visual analysis of 2D images shown in Figure 4.3, it is, then, difficult to determine the behavior of pore structure change with increasing curing period for both OPC-CP-50 and HFSC-CP-50 specimen. In order to facilitate the discussion on characterizing the pore structure from the microtomographic images, the VOI was then extracted from the original data set (Figure 4.4). After pore segmentation and cluster multiple labeling process of each VOI shown in Figure 4.4, the three-dimensional of the pore structure associated with segmented porosity and the corresponding largest percolating pore and isolated porosity were obtained (see Appendix A). The segmented porosity (hereinafter total porosity) refers to the extracted pore space after segmentation whereas the percolating pore cluster is the largest pore cluster that percolates in three orthogonal directions. Furthermore, this percolating pore cluster is also referred here as the percolated porosity and the rest were categorized as isolated porosity.
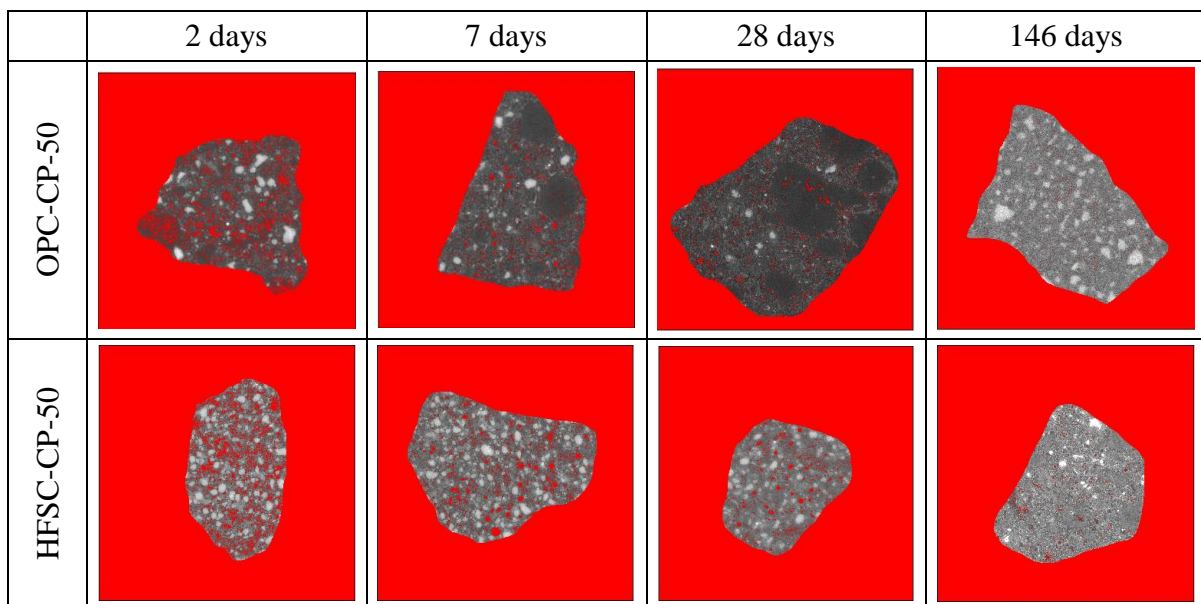
Figure 4.3 2D image processing. The application of red color to enhance the presence of pore in the cross-sectional images of OPC-CP-50 and HFSC-CP-50 specimen.

	2 days	7 days	28 days	146 days
OPC-CP-50				
HFSC-CP-50				
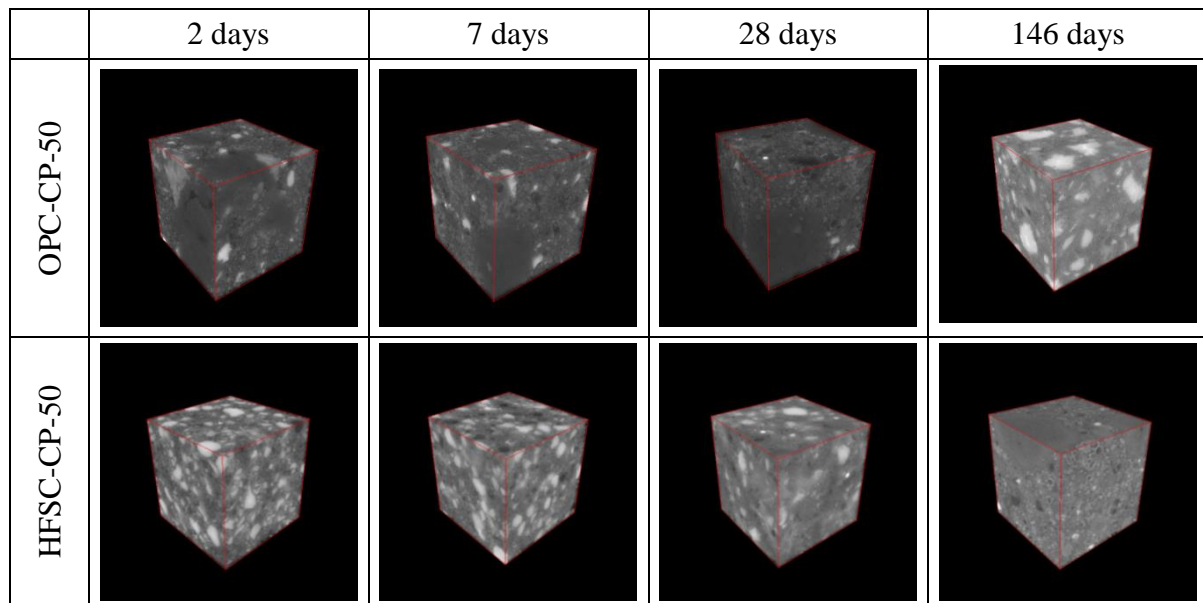
Figure 4.4 Representative VOI of OPC-CP-50 and HFSC-CP-50 with increasing curing periods.

Figure 4.5 shows the pore structure parameters derived from the microtomographic images of OPC-CP-50 and HFSC-CP-50 specimens with increasing curing periods. At 2 days curing period, the total porosity of OPC-CP-50 and HFSC-CP-50 specimen were 17.6% and 19.8%, respectively. At this stage, it can be said that the total porosity for both specimens are almost similar. It is considered that the presence of silica fume contribute to this phenomenon. Silica fume is typically much more reactive, particularly at early ages, because of very small particle size with specific surface area of 200.000 cm^2/g. This means more solid products were formed from pozzolanic reaction of silica fume and reduced the porosity in HFSC-CP-50 specimen. In addition, it can be seen that from the total porosity of 17%, more than 80% pores are connected to each other in OPC-CP-50 specimen at 2 days curing period. Meanwhile, it was more than 90% pores are connected in HFSC-CP-50 specimen. It is considered that most of the connected pore created by free water in the matrix. This free water was mostly used in the OPC-CP-50 specimen due to higher volume of ordinary Portland cement during the hydration process at 2 days curing period. Meanwhile, the volume of free water in HFSC-CP-50 specimen higher than that of OPC-CP-50 specimen due to both silica fume and fly ash does not react with water. In this regard, both volume of percolated porosity and connectivity in HFSC–CP-50 specimen were higher than that of OPC-CP-50 specimen.

Furthermore, as shown in Figure 4.5, the total porosity for both specimens reduced with increasing curing periods. However, a lower rate of decrease in porosity is found in HFSC-CP-50 specimen as compared with OPC specimen with increasing curing period. It is not surprising considering the formation of solid product in the HFSC specimen due to the addition of high volume of fly ash. Pozzolanic reaction in HFSC specimen due to the addition of fly ash will occur after CH which is one of the hydration products was formed. However, it is considered that most of CH had been used by silica fume in pozzolanic reaction at early ages. In the less availability of CH, the pozzolanic reaction due to the addition of fly ash was very slow. In addition, the slow decrease in porosity of the specimen HFSC also followed by a slow decrease in the degree of connectivity of the pore as shown in Figure 4.5. Up to 28 days curing period, the degree of connectivity of HFSC-CP-50 specimen was 80%. Meanwhile, it was 60% for OPC-CP-50 specimen. In this regard, rapid formation of solid
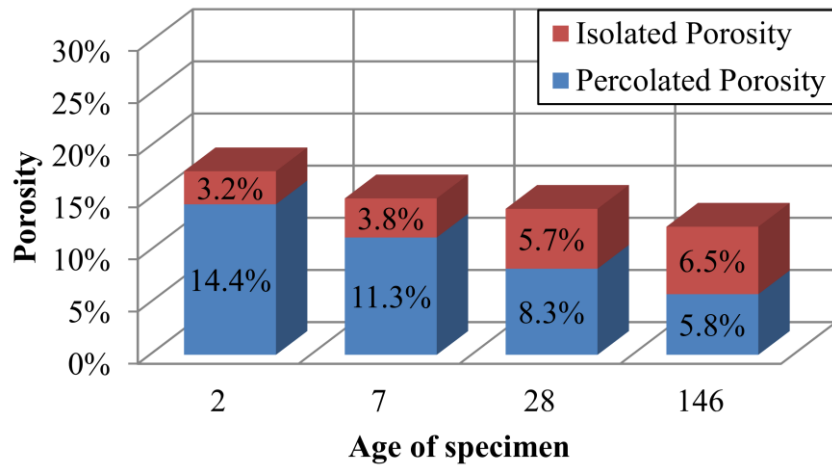
(a) OPC-CP-50
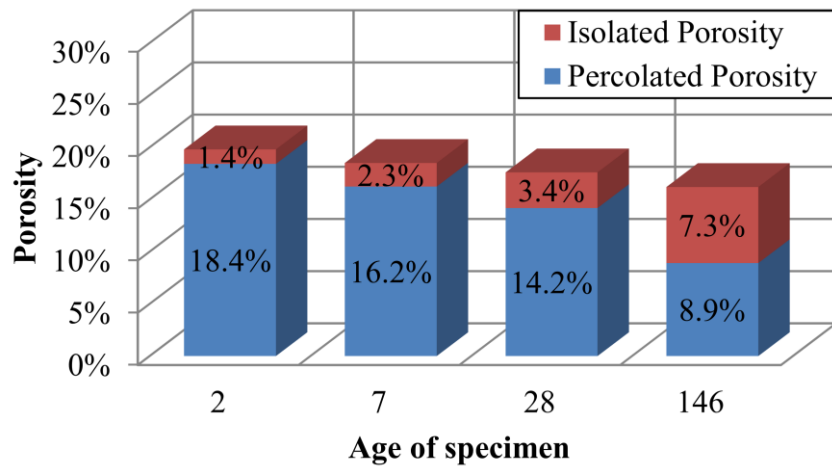
(b) HFSC-CP-50

Figure 4.5 Change of porosity of (a) OPC-CP-50 and (b) HFSC-CP-50 specimen with increasing curing periods.

product during hydration process led to faster reduction of the porosity as well as the pore connectivity.

From Figure 4.5, it can also be seen that from 28 to 146 days curing periods, decrease in the connectivity of pore structure of OPC-CP-50 specimen was slow as compared with that of HFSC-CP-50 specimen. This suggests that after normal curing period, the hydration process of OPC specimen was slow because most of the unhydrated cement clinkers have perfectly hydrated. Later hydration process was hindered by the volume of the solid that had formed earlier. Meanwhile, the solid product in HFSC-CP-50 specimen was formed constantly along with pozzolanic reaction and it was not hindered due to enough space. In addition, from further observation it is found that the presence of fly ash particles in form of cenosphere, which has a low density phase or void surrounded by high density of thin shell, contributed to the amount of porosity of HFSC-CP-50 specimen as shown in Figure 4.6. This fly ash particle (cenosphere) may not react during curing periods and remained in its original form at any time and might be calculated as isolated porosity during pore segmentation and cluster multiple labeling process.
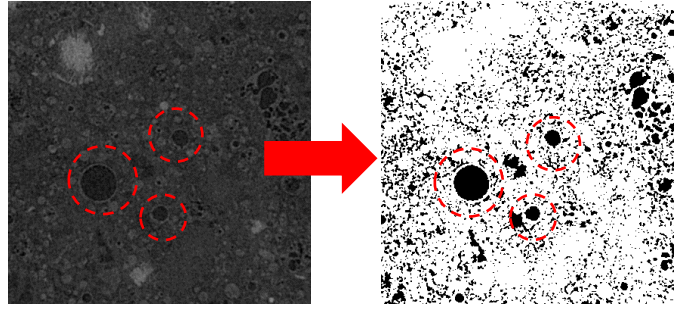
Figure 4.6 The presence of cenospheres in the microstructure of HFSC-CP-50 specimen.

The explanation above shows the capability of X-ray CT technique especially synchrotron X-ray CT in the observation of pore structure evolution with increasing curing periods in different types of cementitious materials, in this case normal cement paste and cement paste mixed with high volume fly ash and silica fume (low alkali binder). Using synchrotron X-ray CT, Provis et al [105] examined the pore structure in the paste specimen of alkali-activated binders. In this regard, the application of synchrotron X-ray CT has been employed to observe microstructure of any cementitious materials which lead to the development of new cementitious materials.

4.1.2. Pore size distribution

Furthermore, by applying *Thickness* plugin the three-dimensional of pore size distribution in the percolated porosity and isolated porosity of each specimen were obtained (see Appendix B). The different colors intensity are used to indicate the pore size where the brighter color shows the bigger pore while the darker color shows smaller pore size. From view point of percolated porosity, it can be seen that at 2 days curing period the distribution of color intensity in OPC-CP-50 specimen looks much darker and more uniform than that of HFSC-CP-50 specimen (see Appendix B). This indicates that the pore size of OPC-CP-50 specimen is smaller than that of HFSC-CP-50 specimen and also it might be dominated by a specific range of pore size. It also can be seen that high intensity color appeared in the pore structure of HFSC-CP-50 specimen and this may be the contribution of cenosphere coming from the inclusion of fly ash. Up to 28 days curing periods, the color of percolated porosity structure of OPC-CP-50 specimen becomes darker and more uniform than before. Meanwhile, little change in color observed from HFSC-CP-50 specimen with increasing curing periods and still brighter than that of OPC-CP-50 specimen in the same curing period. The significant change in color occurred in HFSC-CP-50 specimen from 28 days to 146 days curing period where the color in pore structure becomes darker and more uniform yet it still brighter than that of OPC-CP-50 at 146 days curing period (see Appendix B).

Figures 4.7(a) and (b) show the histogram of pore size distribution of percolated porosity of OPC-CP-50 and HFSC-CP-50 specimen with increasing curing periods, respectively. As shown in Figure 4.7(a), the pore with size range from 1 to 2 μm dominated the percolated porosity of OPC-CP-50 specimen. It took more than 60% pore volume of percolated porosity. Meanwhile, each of pore with size less than 1 μm and pore with size range from 2 to 3 μm contributed to 15% of percolated porosity and the rest of 10% was a contribution of pore with size more than 3 μm. Similar with that of OPC-CP-50 specimen, pore with size range from 1 to 2 μm can also be said dominating the percolated porosity of HFSC-CP-50 specimen but with smaller amount of 45%. Meanwhile, each of pore with size less than 1 μm and pore with size range from 2 to 3 μm contributed to 20% of percolated porosity and the rest of 15% was a contribution of pore with size more than 3 μm.
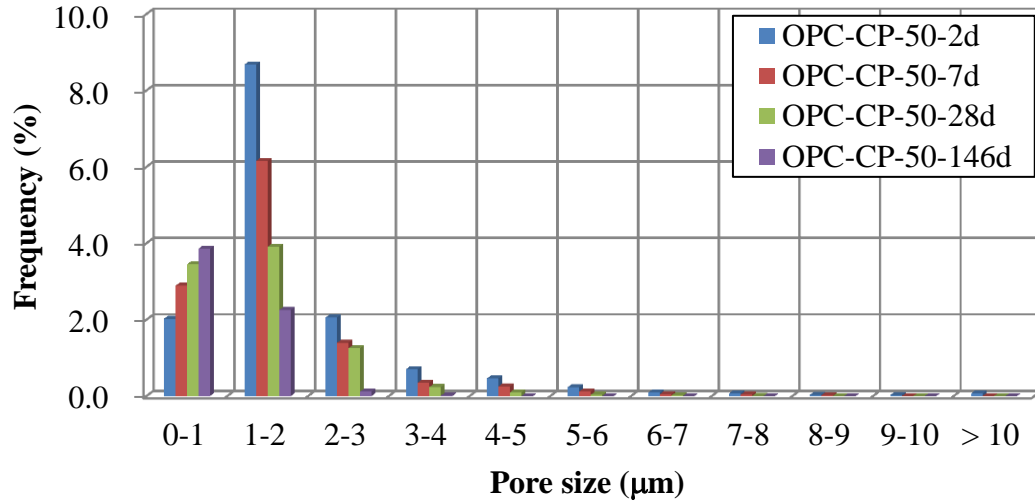
(a)
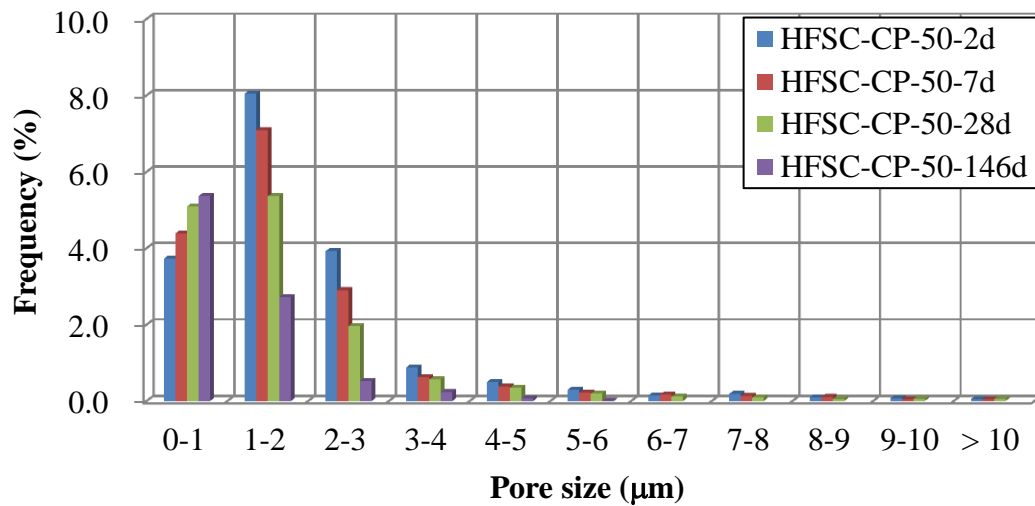
(b)

Figure 4.7 Pore size distribution of percolated porosity of (a) OPC-CP-50 and (b) HFSC-CP-50 specimen.

Furthermore, percolated porosity of both specimens shows similar trend with increasing curing periods. The pore with size less than 1 μm increased while the pore with size more than 1 μm decreased. However, if we look more detail at pore with a size of 1 to 2 μm in the histogram, we found that the pore within these sizes decrease rapidly in OPC-CP-50 specimen as compared with HFSC-CP-50 specimen up to 28 days curing periods. In this regard, the formation of solid product through the hydration process in OPC-CP-50 specimen significantly reduced the size of the larger pore. Meanwhile, the pozzolanic reaction occurred in the HFSC-CP-50 specimen due to the addition of fly ash has slower rate in the reduction of pore with larger size up to 28 days curing periods. As previously described, pozzolanic reaction in HFSC specimen due to the addition of fly ash will occur after CH which is one of the hydration products was formed. In the less availability of CH due to most of CH have been used by silica fume in pozzolanic reaction during the early ages, the pozzolanic reaction due to the addition fly ash was very slow.
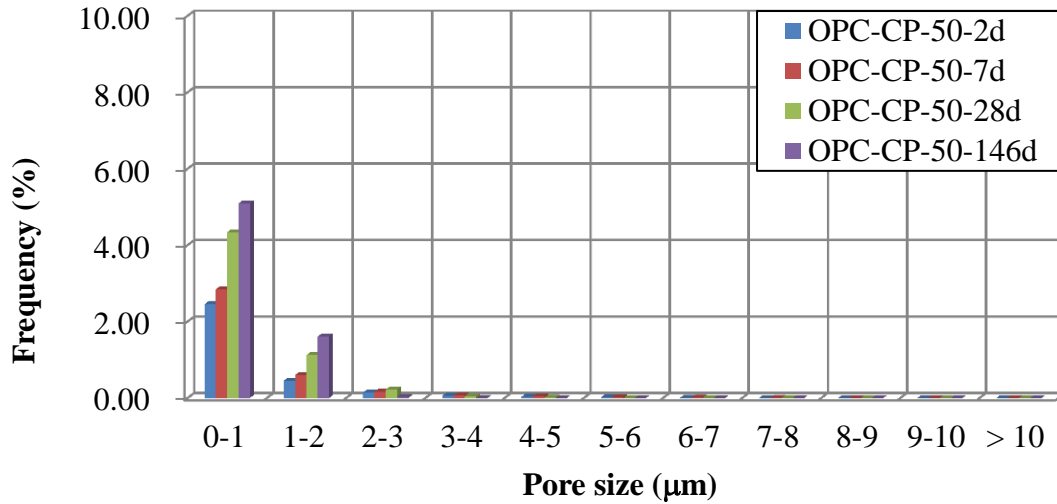
(a)
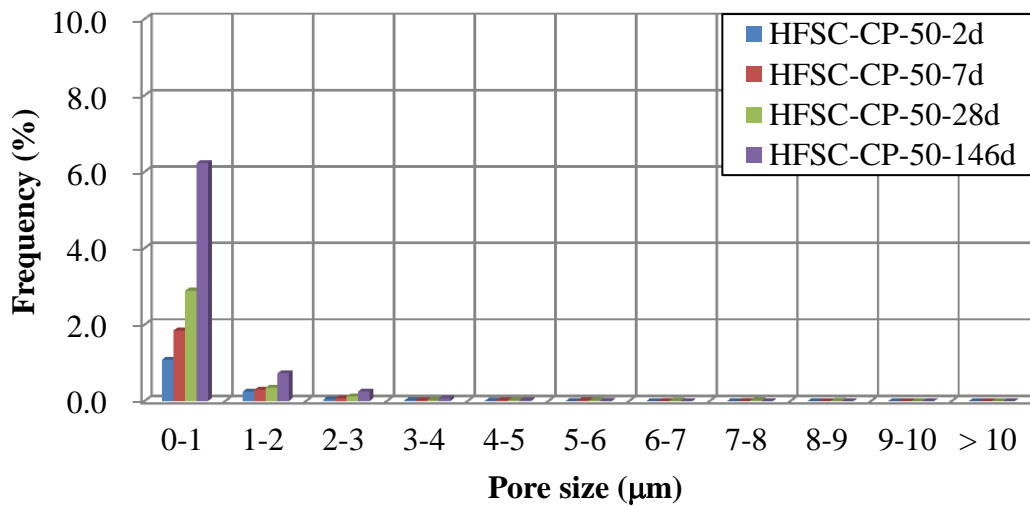
(b)

Figure 4.8 Pore size distribution of isolated porosity of (a) OPC-CP-50 and (b) HFSC-CP-50 specimen.

However, from 28 days to 146 days, HFSC-CP-50 specimen shows more significant in the reduction of pore with larger size as compared with OPC-CP-50 specimen. During these curing periods, it is considered that hydration process from rest of unhydrated cement clinkers in OPC-CP-50 specimen was inhibited by the less availability of free space. Most of spaces have been occupied by the solid product that had formed earlier. The disruption of hydration process in OPC-CP-50 specimen led to a slow in the reduction of pore with larger size Meanwhile, with higher availability of space and ongoing hydration process to produce CH, pozzolanic reaction in constantly occurred in HFSC-CP-50 specimen resulted in rapid in the reduction of pore with larger size.

In addition, at 146 days curing period, the percolated porosity of OPC-CP-50 specimen only compose of pore with size less than 2 μm. Meanwhile, at the same curing period the pore with size range from 3 to 4 μm still found in the percolated porosity of HFSC-CP-50 specimen though in the small amount. It is interesting to obtain this finding, because the use

of high volume of fly ash in mix proportion of cementitious materials has negative effect on the pore size even though underwent longer curing period.

Figures 4.8(a) and (b) show the histogram of pore size distribution of isolated porosity of OPC-CP-50 specimen and HFSC-CP-50 specimen with increasing curing periods, respectively. From these figures, it can be said that the volume of pore in each range of pore sizes of isolated porosity increased with increasing curing periods. Unlike the case of percolated porosity, in isolated porosity it is found that pore with size less than 1 μm dominated the isolated porosity. The increasing number of those pore size certainly originated from the pore that separated from the percolated porosity due to the formation of solid products. In addition, the presence of cenosphere which is unreacted fly ash particle contributes to the increasing pore size of the isolated porosity in HFSC-CP-50 specimen.

Pore size distribution of percolated porosity and isolated porosity was one of other aspects of pore structure parameter that was able to be obtained through the use of X-ray CT technique. This is certainly a positive point in X-ray CT technique.

4.1.3. Diffusion tortuosity

Furthermore, random walk simulation (RWS) was employed to determine to diffusion tortuosity of percolated porosity in each specimen. Figure 4.9 shows an example of trajectory of a walker in pore space (HFSC-CP-50-2d).
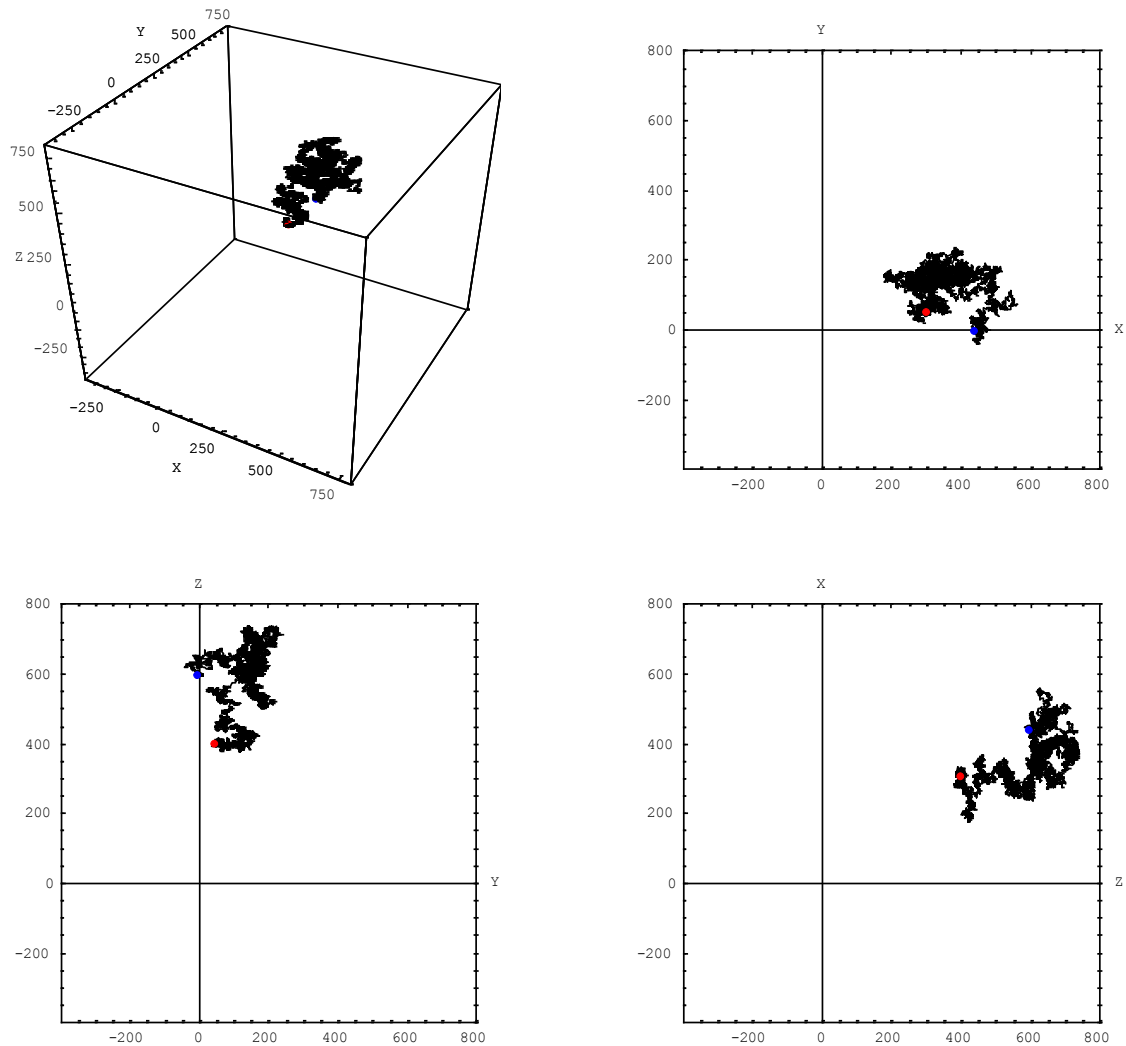
Figure 4.9 Example of trajectory of a walker in pore space (HFSC-CP-50-2d).
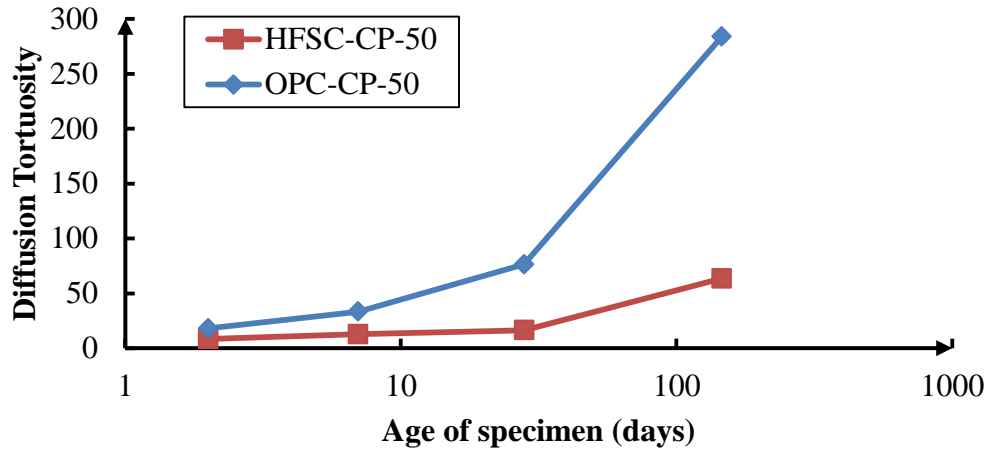
Figure 4.10 Diffusion tortuosity of percolated porosity of OPC-CP-50 and HFSC-CP-50 with increasing curing periods.

      Figure 4.10 shows the diffusion tortuosities for all specimens increasing curing periods. From Figure 4.10, it can be seen that the diffusion tortuosity tends to increase in a 3D pore space with increasing curing periods. These finding reasonable with common knowledge on change in the pore structure in hardened cement paste as the formation of solid product progresses with increasing curing period. However, as shown in Figure 4.10, the rate of increase of diffusion tortuosity in percolated porosity of OPC-CP-50 specimen higher than that of HFSC-CP-50 specimen. This phenomenon certainly related to the rate of decrease of its percolated porosity with increasing curing periods in which it was higher in OPC specimen as compared with that of HFSC-CP-50 specimen. It is easy to understand given that the smaller the percolated porosity the greater tortuosity of pore space due to the formation of solid product.

      On the other hand, it is found that at the similar volume of percolated porosity the diffusion tortuosity of pore space in OPC-CP-50 specimen was higher than that of HFSC-CP-50 specimen. It has been explained that the volume of free water in HFSC-CP-50 specimen higher than that of OPC-CP-50 specimen in the same water to binder ratio due to silica fume and fly ash does not react with water. It is considered that the percolated porosity formed by excessive free water creates less tortuous pore structure. This could be the reason why diffusion tortuosity in HFSC-CP-50 specimen smaller than that of OPC-CP-50 specimen at the similar volume of percolated porosity. The diffusion tortuosity obtained from RWS may indicate that the transport process of any species in the HFSC-CP-50 specimen through its percolated porosity has less obstruction as compared with that of OPC-CP-50 specimen by assuming that the percolated porosity would like most likely contribute to the macroscopic transport property of the hardened cementitious materials [10] although such a permeability or diffusion test were not performed in this study.

      The relationship between diffusion tortuosity and pore size distribution at the similar volume of percolated porosity is not clear in this study. For example, OPC-CP-50-2d specimen has similar volume percolated porosity with that of HFSC-CP-50 specimen but there was a difference in its pore size distribution. The pore with size range form 0-1 μm, 1-2 μm and 2-3 μm occupied 15%, 60% and 15% of percolated porosity in OPC-CP-50-2d, respectively. In this pore size distribution of percolated porosity the diffusion tortuosity is found to be around 18. Meanwhile, it was 35% for 0-1 μm, 35% for 1-2 μm and 15% for 2-3

µm in percolated porosity of HFSC-CP-50-28d specimen and diffusion tortuosity was found to be around 16. Further observation was conducted using OPC-CP-50-28d and HFSC-CP-50-146d which have similar volume of percolated porosity but different in its pore size distribution. With 35% of 0-1 µm, 50% of 1-2 µm and 15% of 2-3 µm in the pore size distribution resulting 76 of diffusion tortuosity in OPC-CP-50-28d. While the diffusion tortuosity of 34 was obtained from 60% of 0-1 µm, 30% of 1-2 µm and 10% of 2-3 µm in the pore size distribution of percolated porosity of and HFSC-CP-50-146d specimen. From this explanation, it is difficult to find a relationship between diffusion tortuosity and pore size distribution in the similar volume of percolated porosity.

4.2. CHANGE OF PORE STRUCTURE IN DETERIORATED CEMENTITIOUS MATERIALS

4.2.1. Leaching mechanism

Figure 4.11 shows representative cross-sectional images of OPC-CP-50 and HFSC-CP-50 specimen before leaching test (146 days curing periods) and after leaching test for 13 weeks. Based on visual observation of cross-sectional images of both specimens before and after leaching test, the darker voxels which represent pore space in the cross-sectional image of OPC-CP-50 specimen increased after leaching test. In this regard, it is estimated that the pore structure of OPC-CP-50 specimen changed after leaching test. As for HFSC-CP-50 specimen, it is a little bit difficult to find the difference in the appearance of cross-sectional images before and after leaching test. This is because of similar appearance of cross-sectional images before and after leaching test.

Before Leaching Test	After Leaching Test
OPC-CP-50-146d	OPC-CP-50-146d-e
HFSC-CP-50-146d	HFSC-CP-50-146d-e
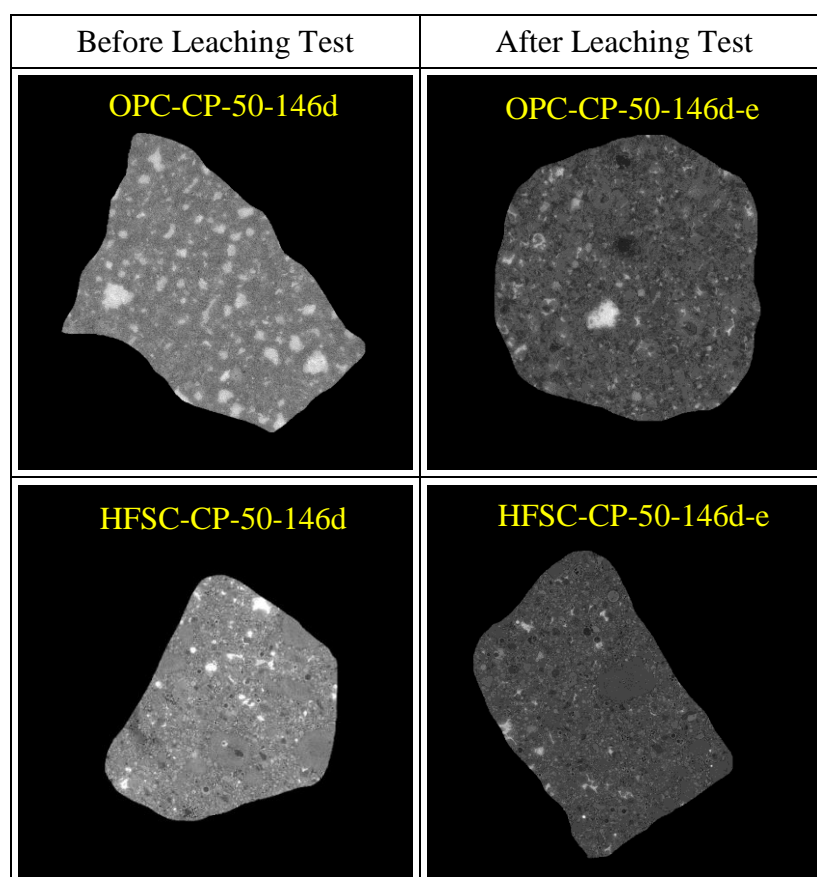
Figure 4.11 Representative cross-sectional images of OPC-CP-50 and HFSC-CP-50 specimen before leaching test (146 days curing periods) and after leaching test for 13 weeks.
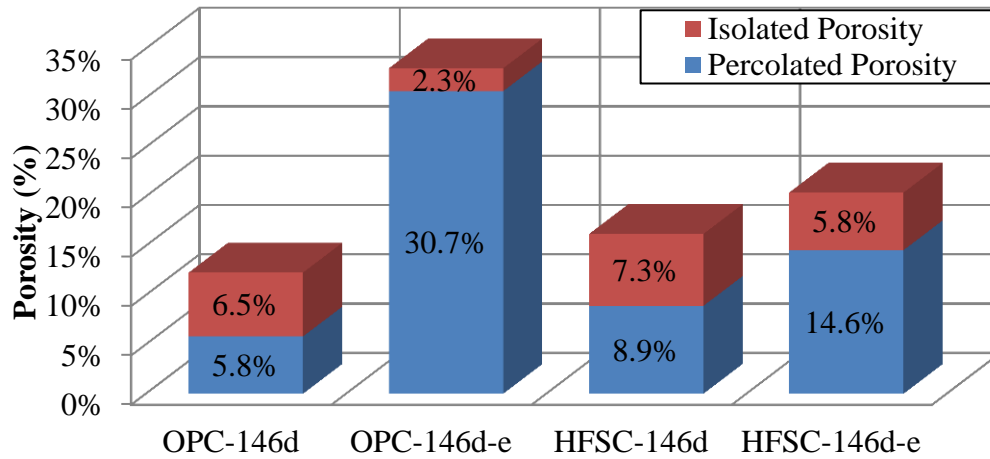
Figure 4.12 Change of porosity in deteriorated OPC-CP-50 and HFSC-CP-50 specimen due to leaching.

Thus, from visual observation of cross sectional image of both specimens before and after leaching test, it can be said that leaching has less effect on the pore structure of cement paste specimen with low alkali binder. On the other hand, it has significant effect on the pore structure of normal cement paste specimen. Furthermore, for further analysis of the effect of leaching on the pore structure of both specimens, the VOI of deteriorated specimen was then extracted from the original data set. The size of VOI of deteriorated specimen was 400^3 voxels which is similar to that of before leaching test that has been analyzed in previous section. After pore segmentation and cluster multiple labeling process of VOI of deteriorated specimen, the 3D geometry of the pore structure associated with segmented porosity and the corresponding largest percolating pore and isolated porosity were obtained (see Appendix C).

Figure 4.12 shows the pore structure parameters derived from the microtomographic images of OPC-CP-50 and HFSC-CP-50 specimen before and after leaching test. As shown in Figure 4.12, before leaching test, the total porosity of OPC-CP-50 specimen was 12.3%. Furthermore, after leaching the total porosity of the OPC-CP-50 specimen increased to the value of 33%. This means that there was an increase in the total porosity of OPC-CP-50 specimen of 2.5 times due to leaching. Meanwhile, for the HFSC-CP-50 specimen the total porosity before leaching test was 16.2%. After leaching test the total porosity of HFSC-CP-50 specimen became 20.4%. In this way, there was an increase in the total porosity of HFSC-CP-50 specimen of 1.25 times due to leaching. From this result, it can be inferred that leaching significantly increases the total porosity of the normal cement paste specimen as compared with cement paste specimen with low alkali binder.

From view point of percolated porosity, before leaching test volume of percolated porosity was 5.8% while after leaching test it increased to the value of 30.7%. On the other hand, before leaching test, the volume of percolated porosity of HFSC-CP-50 specimen was 8.9%, while after leaching test it increased to the value of 14.6%. Although the has been an increase in the volume of percolated porosity of HFSC-CP-50 specimen after leaching test, however, it was not significant as compared with that of the OPC-CP-50 specimen.

In contrary to that of percolated porosity, after leaching test the isolated porosity for both specimens decreased. Before leaching test the volume of isolated porosity of OPC-CP-50 specimen was 6.5% while after leaching test it became 2.3%. As for HFSC-CP-50, it was decreased from 7.3% to 5.8%. This result indicates that dissolution of hydration products due to leaching not only creates the new pore space in the microstructure of cementitious material but also able to connect the isolated porosity. In addition, it also can be seen that the

formation of new pores in the microstructure of normal cement paste specimen during leaching test is faster than that of cement paste specimen with low alkali binder.

Furthermore, it can be estimated that the increase in porosity due to leaching can cause an increase in the pore size of the pore structure. Through the application of *Thickness* plugin, the three-dimensional of pore size distribution of pore structure of OPC-CP-50 and HFSC-CP-50 specimen before and after leaching test were obtained (see Appendix D). As described previously, very dark color appeared in both percolated and isolated porosity of OPC-CP-50 specimen before leaching test. This indicates that pore with smaller size occupied the pore structure. Meanwhile, at 146 days curing period HFSC-CP-50 specimen showed just a little bit brighter color than that of OPC-CP-50. In this way, it can be said that before leaching test the pore size of the pore structure of OPC-CP-50 specimen smaller than that of HFSC-CP-50 specimen. After leaching test, the brighter color appeared in the percolated porosity of OPC-CP-50 specimen. This indicates that there was an increase of larger pore size present in percolated porosity structure after the leaching test. On the other hand, for HFSC-CP-50 specimen the result looks similar indicating little increase in the pore size of percolated porosity after leaching test. Furthermore, for the isolated porosity structure of both specimens show similar results in which the color appeared before and after leaching test looks similar.
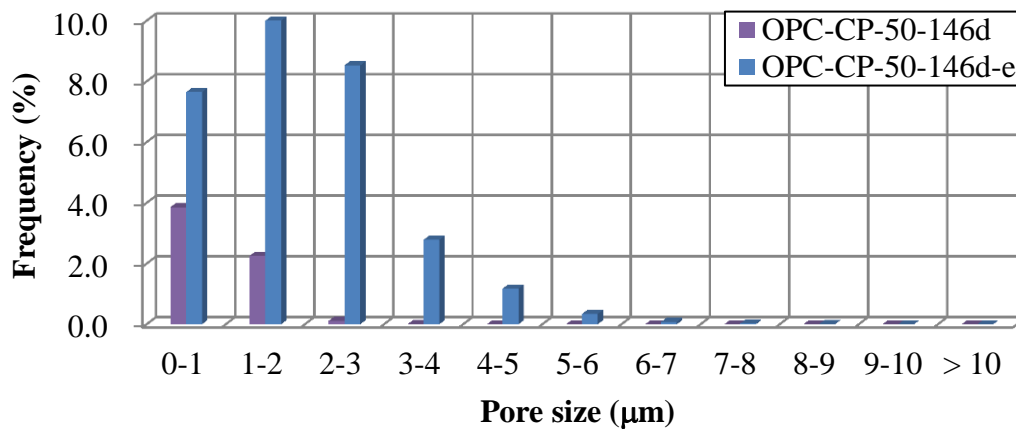
(a)
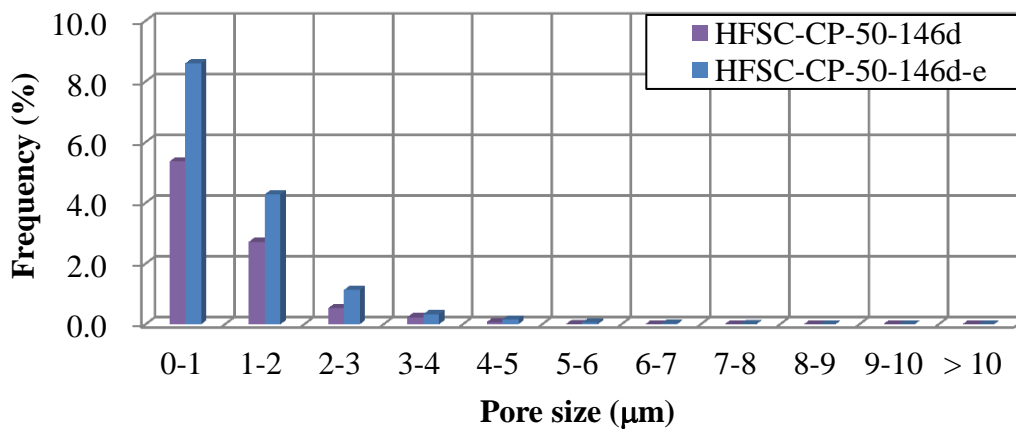
(b)

Figure 4.13 Pore size distribution of percolated porosity of (a) OPC-CP-50 and (b) HFSC-CP-50 specimen before and after leaching test.

Figures 4.13(a) and (b) show the change of the histogram of pore size distribution of percolated porosity before and after leaching test of OPC-CP-50 and HFSC-CP-50 specimen, respectively. It has been described that at 146 days curing period, the percolated porosity of OPC-CP-50 specimen only composed of pore with size less than 2 μm. Meanwhile, at the same curing period the pore with size range from 3 to 4 μm still found in the percolated porosity of HFSC-CP-50 specimen though in the small frequency. After leaching tests for 13 weeks, the distribution of pore structure of OPC-CP-50 specimen was significantly changed. The increased volume of pore occurred up to pore with size of 6 μm. In addition, unlike before leaching test in which the highest pore volume in the percolated was the pore with size less than 1 μm, after leaching test it was found that the volume of pore with size range from 1 − 2 μm was the highest. For HFSC-CP-50 specimen, it was extremely different from that of OPC-CP-50 specimen. An increase in pore volume of HFSC-CP-50 specimen after leaching test was clearly seen in pore with sizes smaller than 1 μm.
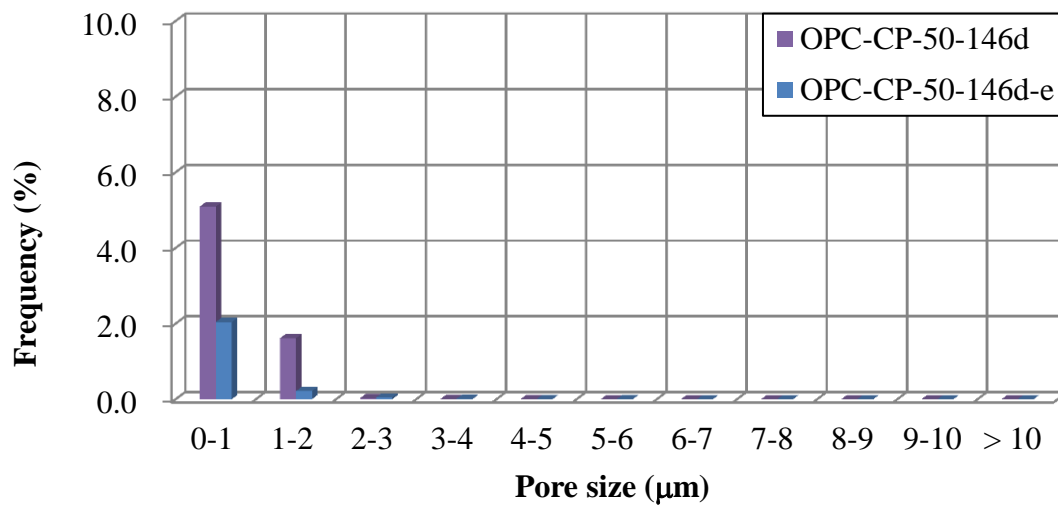
(a)
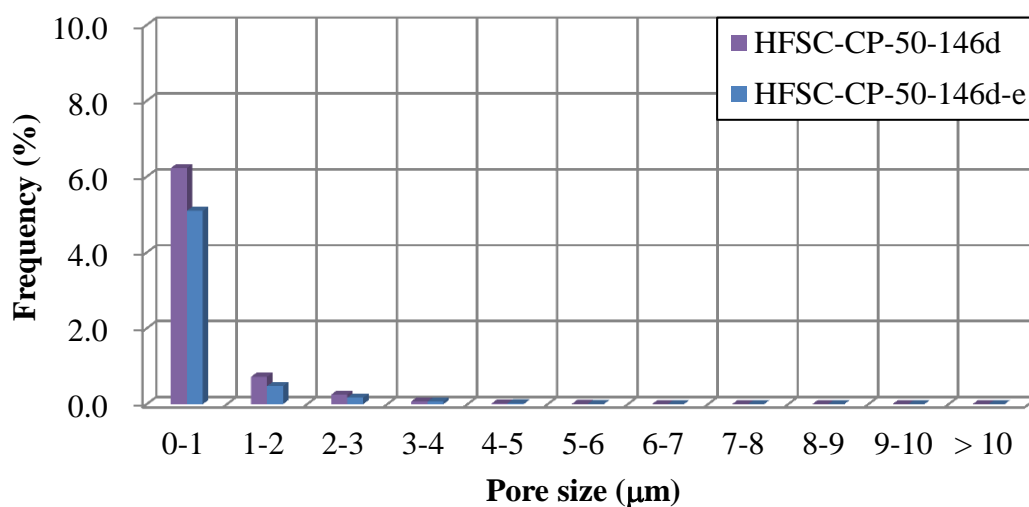
(b)

Figure 4.14 Pore size distribution of isolated porosity of (a) OPC-CP-50 and (b) HFSC-CP-50 specimen before and after leaching test.

Daimon et al [106] considered that the C-S-H gel consisted of gel particles with an internal structure, together with pores with equivalent diameters of 3.2-200 nm. Based on this information, pores within this range were considered to be related to the C-S-H gel. In this study, by using a resolution of 0.5 μm such pore will not be detected. However, it is considered that in the absence of CH in the microstructure of HFSC-CP-50 specimen the deterioration occurred due to the decalcification of C-S-H. In this regard, increasing pore volume with sizes smaller than 1 μm somehow related to the decalcification of C-S-H. Furthermore, considering that the changes in pore structure due to decalcification of C-S-H increases the pore volume with size less than 1 mm, it is thought that an increase in pore volume with a size greater than 1 mm in the OPC-CP-50 specimen is the contribution of dissolution of CH. This result is considered reasonable by considering that in hardened cement, CH is often observed in the form of crystal larger than a few microns and C-S-H is very small in comparison. In addition, it can also be seen that the formation of new pores due to the dissolution of CH is much faster compared to that of due to the decalcification of C-S-H.

Figures 4.14(a) and (b) show the change of the histogram of pore size distribution of isolated porosity before and after leaching test of OPC-CP-50 and HFSC-CP-50 specimen, respectively. From Figure 4.14(a), it can be seen that the volume of pore reduced significantly due to leaching for 13 weeks especially for the pore with size less than 1 μm. Most of the isolated porosity in the OPC-CP-50 specimen was connected to the percolated porosity after the leaching test led to reduce in the volume of isolated porosity. Meanwhile, as shown in Figure 4.14(b), little changed occurred in pore size distribution of the isolated porosity of HFSC-CP-50 specimen.

Furthermore, random walk simulation (RWS) was employed to evaluate the change in pore structure geometry after leaching test from view point of diffusion tortuosity. Figure 4.15 shows the diffusion tortuosity in both percolated porosity of OPC-CP-50 and HFSC-CP-50 specimen after leaching test. The diffusion tortuosity of OPC-CP-50 specimen before and after leaching was estimated to be 284 and 7, respectively. Meanwhile, it was 63 and 31 for HFSC-CP-50 specimen before and after leaching test, respectively. Dissolution of hydration product in OPC-CP-50 specimen reduced dramatically the diffusion tortuosity to a single digit
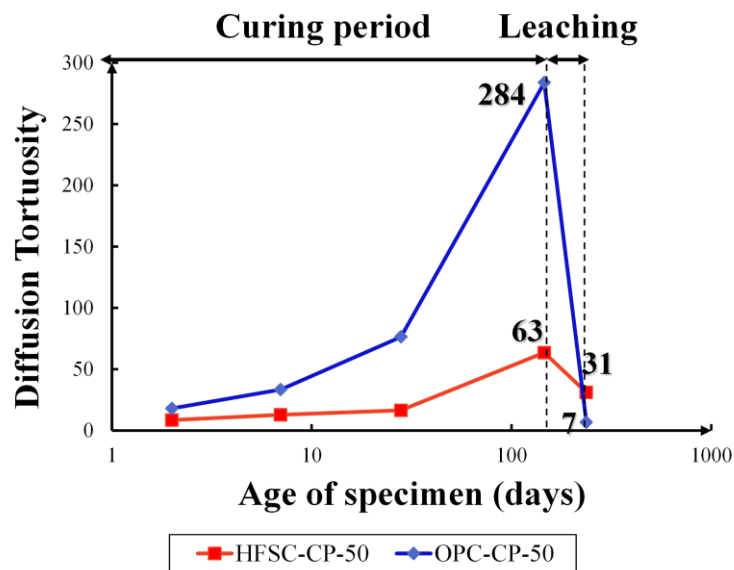
Figure 4.15 Diffusion tortuosity in OPC-CP-50 specimen and HFSC-CP-50 specimen with increasing curing periods and after leaching test.

as more isolated pore become connected with percolated porosity as well as new pores are formed and connect to the percolated porosity. On the other hand, although there was a reduction in the diffusion tortuosity for percolated porosity of HFSC-CP-50 specimen, however, it was not dramatically when compared with that of OPC-CP-50 specimen.

Before leaching test, it is found that transport process of any species in the HFSC-CP-50 specimen through its percolated porosity has less obstruction as compared with that of OPC-CP-50 specimen. Meanwhile, as the diffusion tortuosity decrease dramatically in the OPC-CP-50 specimen after leaching, the transport process of any species in OPC-CP-50 through its percolated porosity is far more facile then that of HFSC-CP-50 specimen. This condition also supported by higher volume of percolated porosity as well as the pore size distribution became coarser.

4.2.2. Microstructure study under tensional force

Figure 4.16(a) and (b) show the representative cross-sectional image of fly ash mortar in initial condition and applied load of 4.27 N. From Figure 4.16(a), it can be seen the presence of aggregates which have higher color intensity than the hydration products. In addition to the presence of aggregate, the shades of color in the specimen cross-sectional images of fly ash mortar is highly variable. If the specific range of the color intensity represents a particular phase of a cementitious material, therefore it can be estimated that there are many phases present in the microstructure of fly ash mortar. These phases include, hydration product, unhydrated cement grains and unreacted fly ash grains. The presence of these phases in the microstructure of fly ash mortar may affect the behavior of fly ash mortar itself under mechanical load.

Furthermore, the tensile load of 4.27 N was applied and then observed by using synchrotron X-ray CT at the same time. However, it is difficult to find the change in the microstructure before and after load applied from the investigation of microtomographic images. It is considered that the maximum load could not be reached in the experiment due to loss of grip on the clamps of specimen. In order to prove this phenomenon, we observed the change in the position and diameter of the void target due to the application of load. In fact, voids have a tendency to change in its shape when the load is applied in cementitious materials. The VOI with size of 200^3 voxel contained void target in initial condition as shown in Figure 4.17 was selected. The details information of this VOI is shown in Table 4.1. After separating void target with other object through pore segmentation and multiple clusters

(a)   (b)
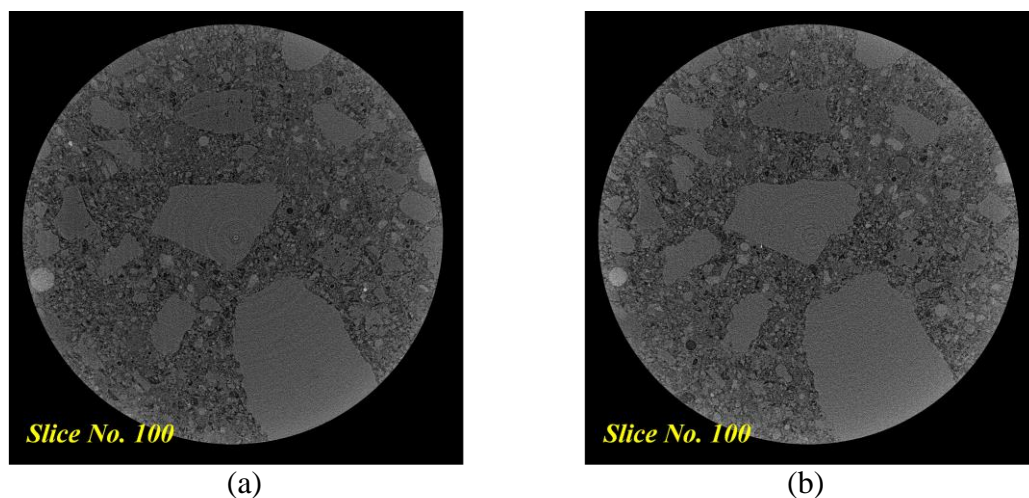
Figure 4.16 Representative cross-sectional images of fly ash mortar. (a) Without load and (b) tensile load of 4.27 N.
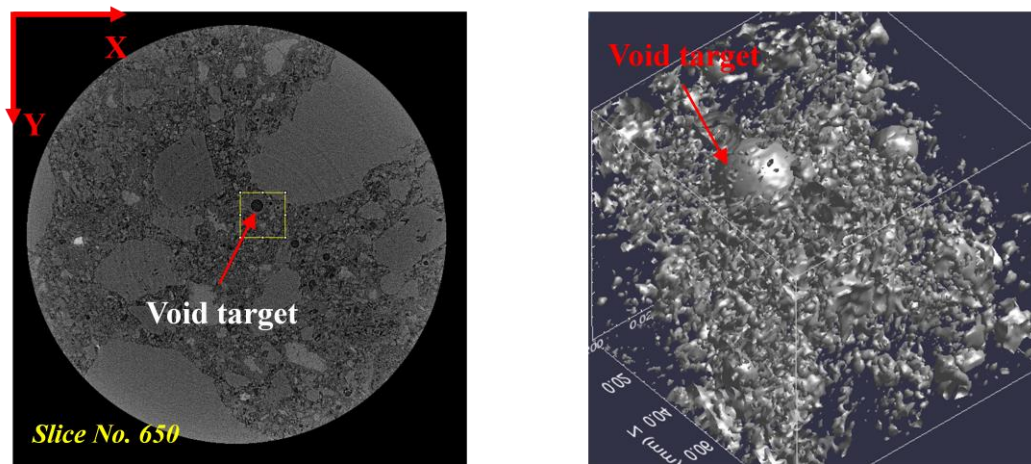
Figure 4.17 VOI selection in the microtomographic images of fly ash mortar to analyze the position and diameter of void target in initial condition.

Table 4.1 Details information of VOI in 1300 contiguous microtomographic images

Slice	550-750
Position	
- X coordinate	1000
- Y coordinate	800

labeling, the coordinate of void target in the VOI coordinate in initial condition was obtained as shown in Table 4.2. The coordinate of void target is defined as lower and upper surface coordinate. For the example, in Z direction, lower surface coordinate indicate the coordinate at the bottom surface of the void target. Meanwhile, upper surface coordinate represent the coordinate at the top surface of the void target. In this case, the diameter of void target was calculated by subtracting the upper coordinate with lower coordinate. Using this method the diameter of void target was found to 58 voxel (29 μm).

      In the same way, the observation was performed to determine the position and diameter of the same void target in load applied condition. The details information of VOI in initial condition was used in the load applied condition. As the result, the coordinate of void target in load applied condition as well as its diameter are shown in Table 4.2. From Table 4.2, it can be seen that position of void target changed largely in Z direction (load direction). Meanwhile, it was little changed in both X and Y direction. However, the change of the position of void target was not accompanied by the change of its diameter. As shown in Table 4.2, there was

Table 4.2 The coordinate and diameter of void target before and after tensile load of 4.27 N.

	Initial Condition			Tensile Load of 4.27 N		
	Lower coordinate	Upper coordinate	Diameter	Lower coordinate	Upper coordinate	Diameter
X	46	104	58	47	105	58
Y	113	171	58	114	172	58
Z	44	102	58	68	126	58

no changed in the diameter of void target in X, Y and Z coordinate. This result indicates that the microstructure of fly ash mortar specimen did not respond the tensile load due to loss of grip on the clamps of specimen. The amount of load applied before losing grip unable to generate considerable strain that can be detected with spatial resolution of 0.5 μm/voxel. In this way, the stress level occurred on the load bearing phases cannot be determined.

Although there was no definite result of this experiment, however, by improving the quality both sample preparation and loading instrument, the behavior of microstructure under external load could be observed through the application of synchrotron X-ray CT combined with other mechanical tests.

4.2.3. High temperature exposure and re-curing

Figure 4.18 shows the cross-sectional images of both water re-cured and air re-cured concrete specimens after heating. In the specimen used to investigate water re-curing, it can be seen that there are several large aggregates occupying various spaces; in particular, some of the aggregates are at the surface of the specimen and were likely cut when the core was extracted from the original concrete cylinder. The shades of these aggregates also vary, which implies that the aggregates in the concrete are of differing mineral compositions. As the thermal behavior of aggregates depends on the mineral composition [107], these images clarify that the concrete specimen, when under heating, will undergo varying degrees of thermal stresses.

For the specimen used to investigate air re-curing, one large aggregate appears to occupy the center of the specimen at lower heights, whereas other smaller aggregates can be seen in the upper part of the specimen and around its surface. In addition, a small void at the surface of the specimen can also be seen in the upper part of the specimen. The aggregates in this specimen are also of varying shades of grey, and thus composed of varying minerals with differing thermal behavior.
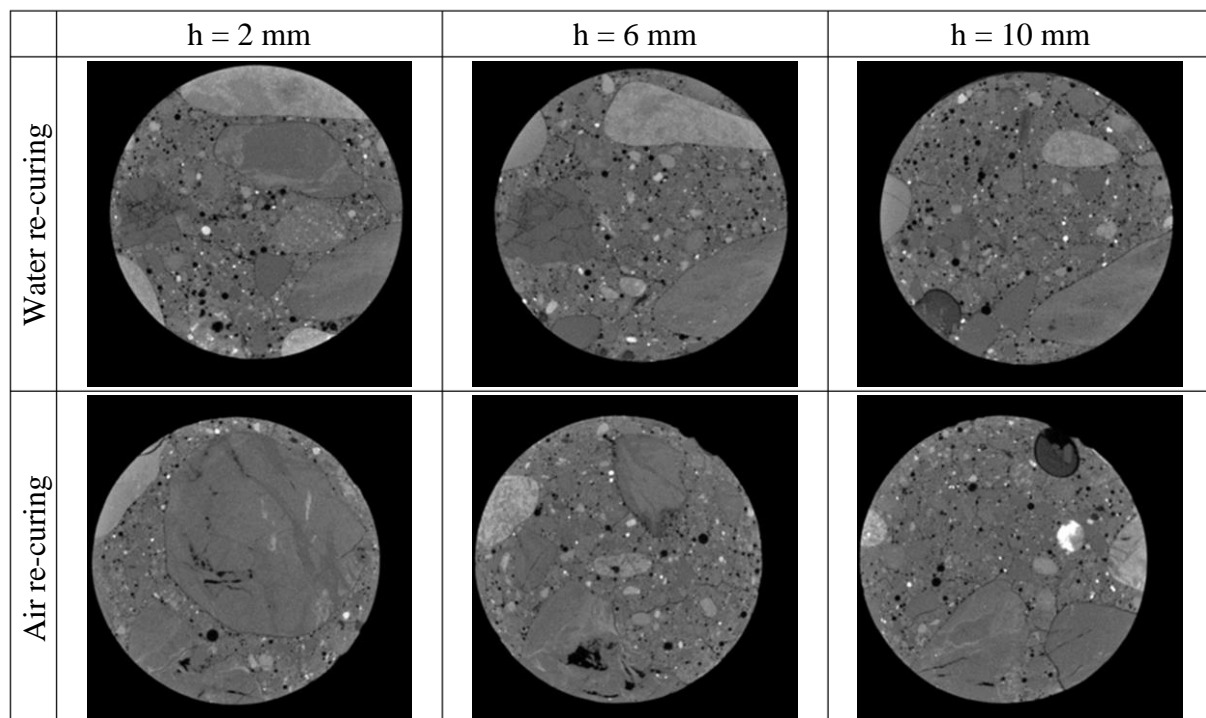
Figure 4.18 Cross-sectional images of concrete specimens after heating used for water re-cured and air re-cured.

	h = 2 mm	h = 6 mm	h = 10 mm
Water re-curing			
Air re-curing			
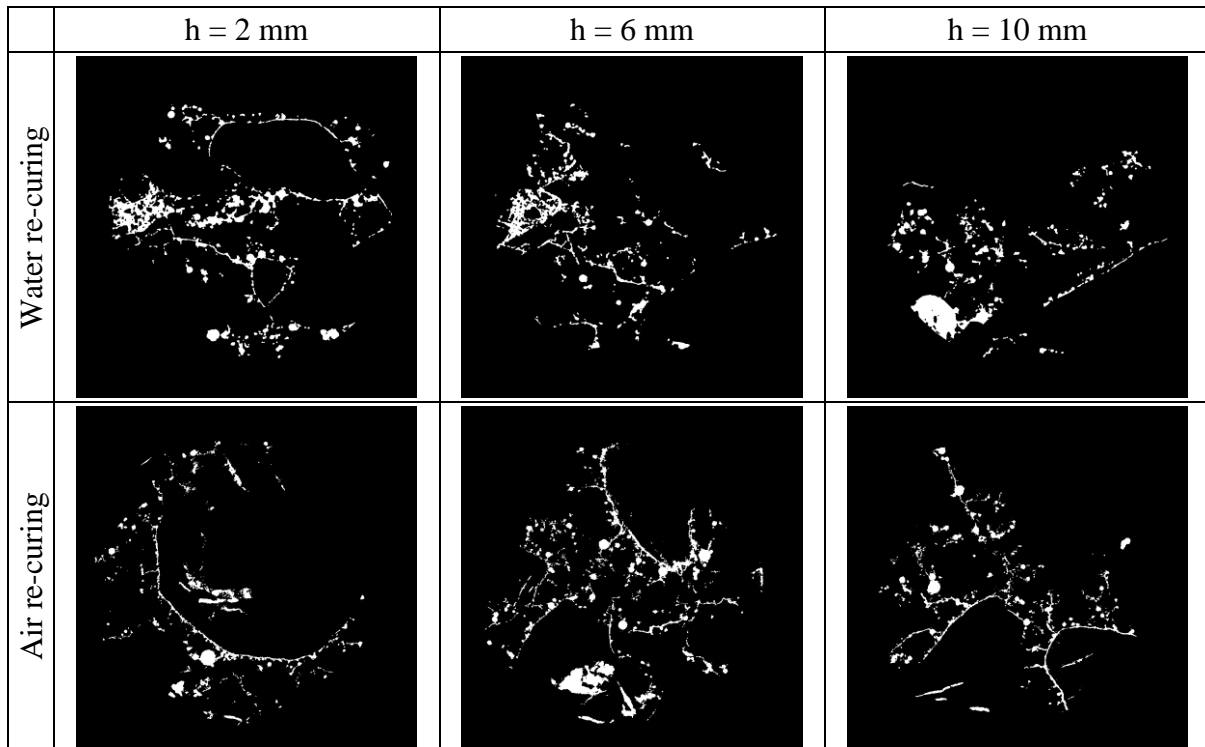
Figure 4.19 Images of percolated porosity space in water and air re-cured specimen.

Following the cluster multiple labeling, slices images of the connected pore space were extracted for both water re-cured and air re-cured specimen. The resultant images are shown in Figure 4.19. The post-heating images clearly show that cracks formed in several ways: around aggregates which were completely inside the specimen; cracks which bridged between different aggregates; and cracks which bridged between aggregates and large air voids. In the air re-cured specimen, cracks formed in a similar manner as in the water-re-cured specimen: distinct crack surfaces can be seen in aggregate-mortar interface, along with some crack bridging. Therefore, the volume of total and percolated porosity of heated specimen increased due to the presence of these cracks.

Figures 4.20 shows the pore structure parameters derived from microtomographic images after segmentation and cluster multiple labeling processes. As shown in Figure 4.20(a), in the water re-cured specimen the total porosity after heating was 9.4%. Meanwhile, for the air re-cured specimen (Figure 4.20(b)) it was slightly higher to the value of 9.9%. At 7 days of water curing, the total porosity of water re-cured specimen reduced to 5.9%. Unlike water re-curing, air re-curing did not lead to large reduction in total pore volume, with a decrease of only 0.5%. Further re-curing both in water and air up to 28 days only contributed to a minor reduction in the total pore volume.

Significant decrease in the total porosity of water re-cured specimen at 7 days was also accompanied by a decrease in its connectivity. After heating, degree of connectivity of pore structure in water re-cured specimen was 60%. Meanwhile, after 7 days of water re-curing the connectivity of pore became 36%. The majority of the microstructure recovery under water supply occurred within the first seven days of re-curing. While some studies have also reported high degrees of rehydration within the first seven days of re-curing [81], in general the recovery of concrete properties has been observed to occur over a period of weeks or months [108,109]. The fast pace of microstructure recovery was assisted by the high connectivity after heating and the relatively small specimen size, which enabled the quick supply of water to the dehydrated cement particles. It is not clear, however, whether the
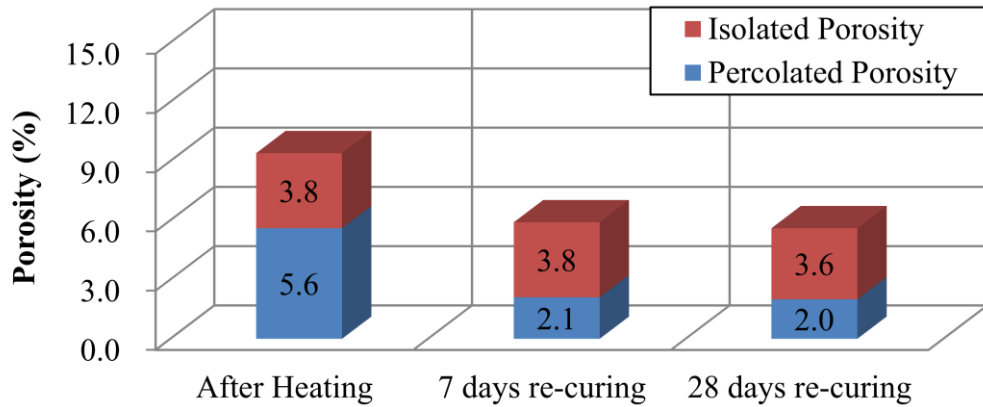
(a)
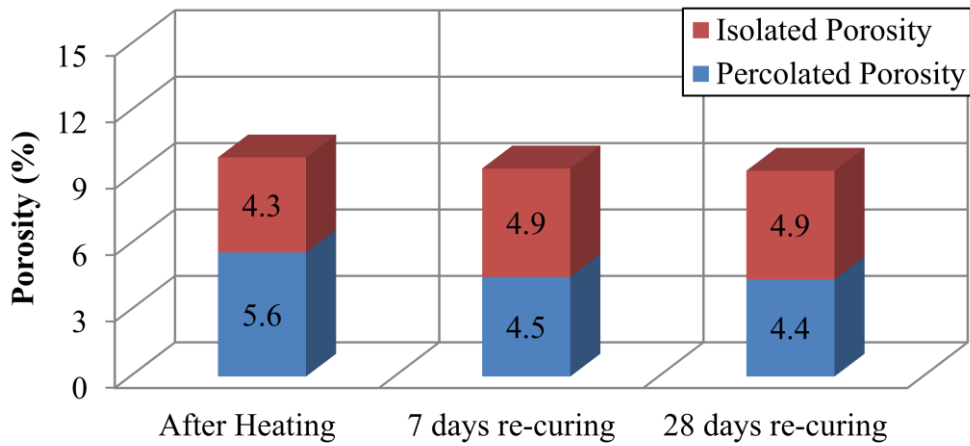
(b)

Figure 4.20 Change of porosity of (a) water re-cured specimen and (b) air re-cured specimen with increasing curing periods.

recovery of the connected pore space was achieved by crystalline regrowth, expansion under rehydration, or some other self-healing mechanism. Further examination of pore structure of water re-cured specimen at 28 days shows that some connected pore space remained at the center of the specimen and in the aggregate-mortar interfaces, the self-healing of surface crack at short period water re-curing may have stopped the supply of water necessary to further reduce the residual connected pore space. This should be the reason why the microstructure recovery after 7 days of water re-curing was very slow.

Although the microstructure of the air re-cured specimen may not have undergone significant changes during re-curing which indicated by small decrease in the total pore volume over 28-day period, this does not imply that air re-curing carries no benefit for the recovery of concrete properties. Specifically, fire-damaged concrete left in atmospheric conditions has been found to undergo extensive carbonation due to the reaction of atmospheric CO_2 with calcium oxide produced by the dehydration of hydration products [18]. In reinforced concrete this leads to deterioration over time, but in non-reinforced concrete carbonation serves as a major contributor to strength recovery by producing a denser pore structure. However, the effects of carbonation on the microstructure were not observed in this study.

4.3 OBSERVATION AND QUANTIFICATION OF CRACK GEOMETRY
4.3.1. Crack geometry for splitting tensile crack

Figure 4.21 shows the representative cross-sectional images of cracked specimen generated by splitting tensile test. In these images, lighter shades of grey voxels indicate higher density materials, whereas darker shades of grey voxels or black indicate lower density materials or air voids, respectively. It also can be seen the presence of heat-shrinkable tube which surrounds the specimen. The heat-shrinkable tube was used to prevent sudden failure during the splitting tensile test to generate the crack in the specimen. Based on visual observation of these figure, it is found that there was a fundamental difference between the cross-sectional images of OPC-MR-60 specimen and FA-MR-60 specimen. The difference lies in the presence of pore space in which the OPC-MR-60 specimen appears to have more pore spaces in its cross-sectional image as compared with FA-MR-60 specimen. In this regard, the use of 30% fly ash as ordinary Portland cement replacement accompanied by a longer curing period increased the density of its microstructure by pozzolanic reaction. Furthermore, from Figure 4.21, it can be seen that the crack splitting the specimen into two separate parts and is prone to failure. Because of the application of heat-shrinkable tube, we were able to have the perfect cracked specimen without having fears of failure during specimen preparation. Through a deeper visual observation, it is found that some parts of the crack in the OPC-MR-60 specimens (both in smaller and higher crack opening width) formed in the pore. It is, then, certainly increase the crack width in those particularly area. In this regard, it is expected that the cracks in the OPC-MR-60 specimens have greater variation in its crack width as compared with FA-MR-60 specimen.
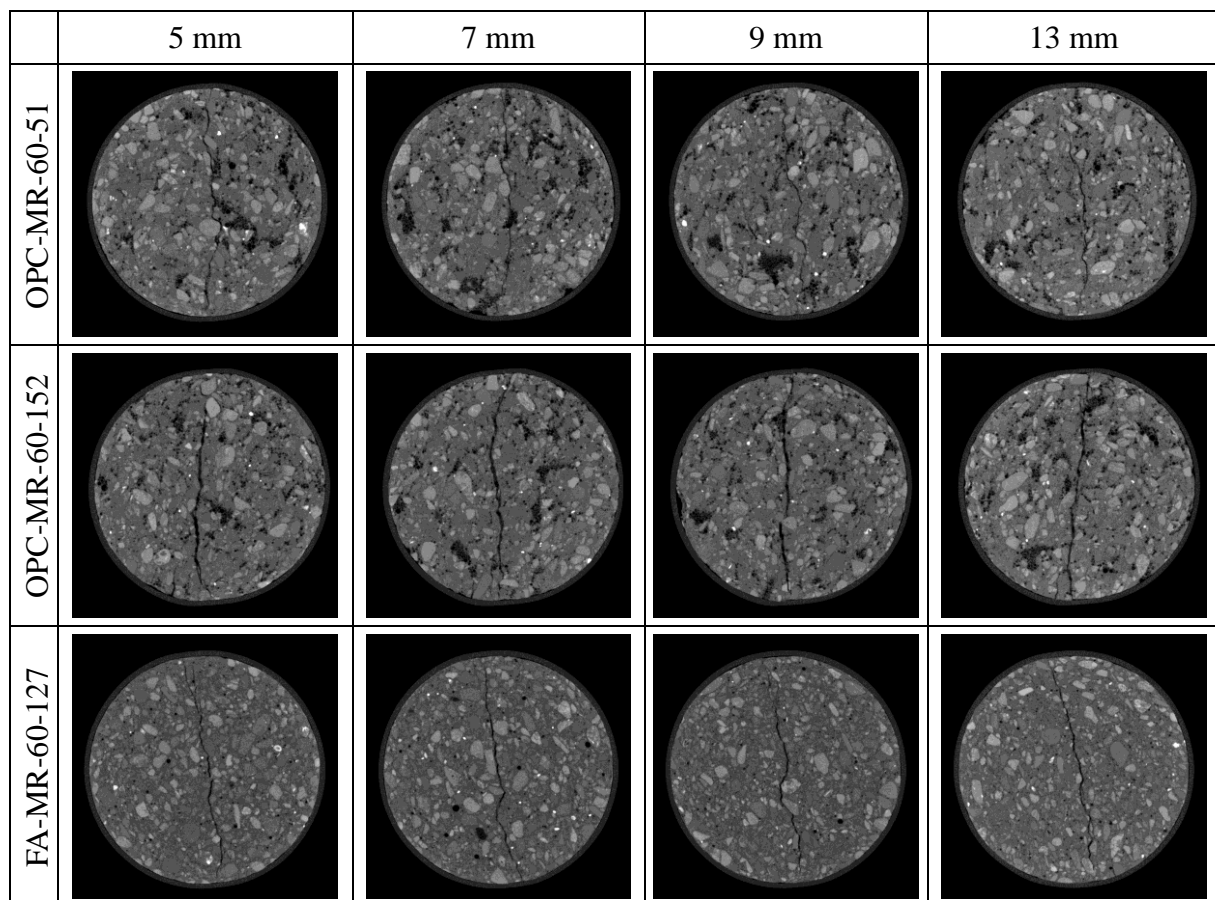
Figure 4.21 Representative cross-sectional images of cracked specimen generated by splitting tensile test.

	X-Y	Y-Z	X-Z
OPC-MR-60-51	13.2 mm	13.2 mm / 13.2 mm	13.2 mm
OPC-MR-60-152	13.2 mm	13.2 mm / 13.2 mm	13.2 mm
FA-MR-60-127	13.2 mm	13.2 mm / 13.2 mm	13.2 mm
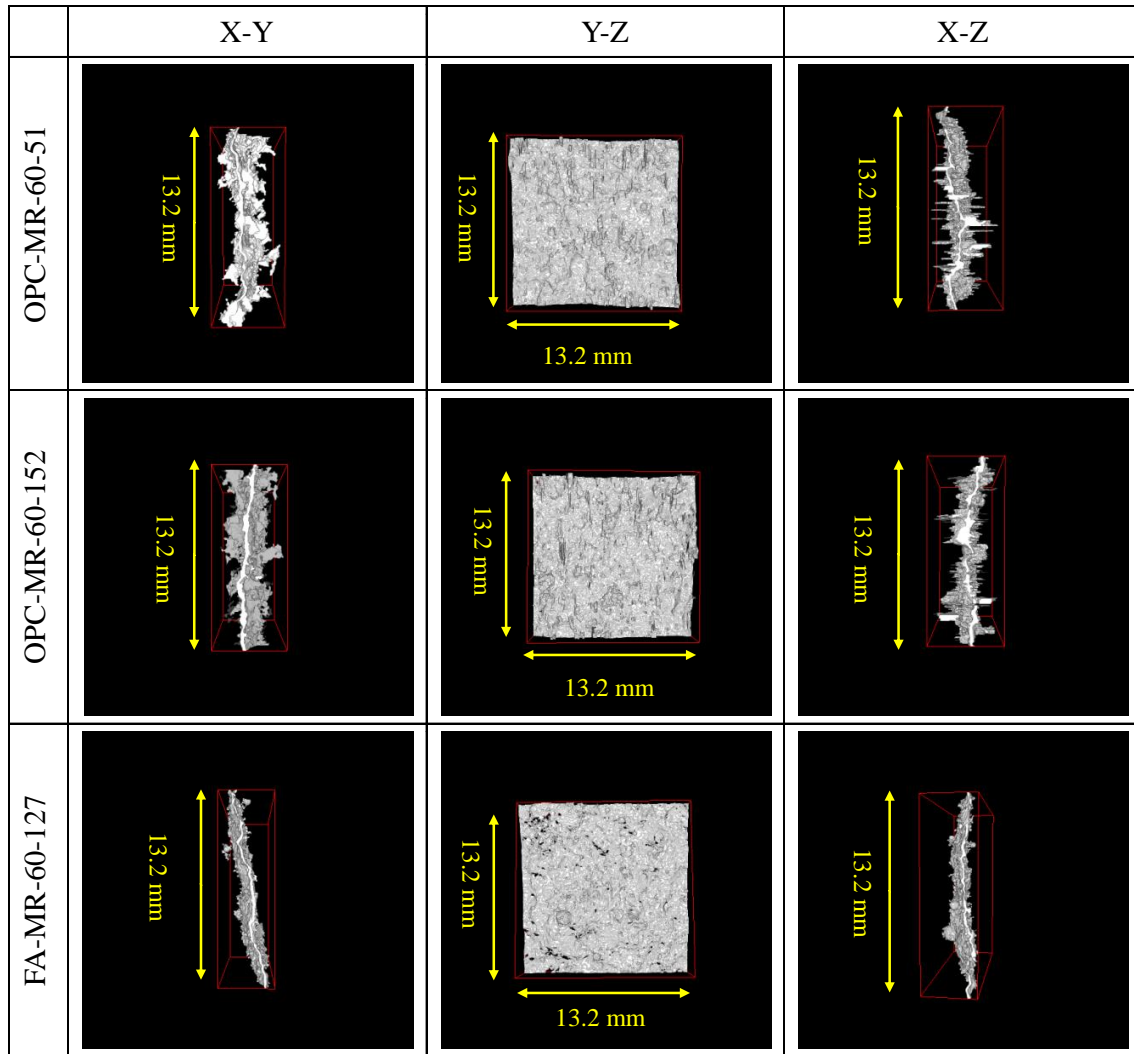
Figure 4.22 Visualization of 3D crack network derived from microtomographic images of splitting tensile cracked specimen

Figure 4.22 visualizes three-dimensional cracks network derived from microtomographic images of cracked specimens after void segmentation and cluster multiple labeling. After conducting a visual observation of the 2D cross-sectional images for each specimen, it is known that some parts of the crack in the OPC-MR-60 specimens (both in smaller and higher crack opening width) occurred through the pore. Furthermore, the results found by visual observation of the three-dimensional crack network, especially in the X-Y or X-Z coordinates, also showed similar results. It can be seen that some pores are connected to the crack structure after void segmentation and cluster multiple labeling and certainly affect the crack geometry parameter especially for crack constrictivity.

Subsequently, the crack geometry parameter will be determined by using 3D crack network shown in Figure 4.22. In this study, as described in the Section 3.2.5, the crack geometry parameters are defined as geometric tortuosity, and constrictivity. Table 4.3 summarizes the crack geometry parameters of derived from three-dimensional crack network. The tortuosity is found to be around 1.25 to 1.26. This means that in spite of differing mix proportions and crack opening widths, the length of the crack in the specimen, which contains maximum aggregate size of 1.7 mm and a crack that was induced by a splitting tensile test, was about 25% longer than the length of specimen.

Table 4.3 The crack geometry parameters of splitting tensile cracked specimen

Specimen	Residual COD (μm)	Tortuosity (τ)	Constrictivity (δ)
OPC-MR-60-51	51	1.25	0.54
OPC-MR-60-152	152	1.25	0.59
FA-MR-60-127	127	1.26	0.80

The constrictivity of FA-MR-60-127 is the largest while OPC-MR-60-152 exhibits equivalent constrictivity to that of OPC-MR-60-51 as shown in Table 4.3. It is interesting to obtain these findings because the crack opening width of OPC-MR-60-152 is three times larger than that of OPC-MR-60-51 and slightly larger but roughly equivalent to that of FA-06-127. This result suggests that in spite of different crack opening width, the cracks that occur in the same material would have similar crack constrictivity value. Thus, the type of materials play important role on the constrictivity of the crack. Different types of materials certainly have a difference in its pore structure, and then when crack occurred due to external load, some parts of the crack are formed or goes through the pore and are considered to be connected each other (crack and pore). This condition has an effect on the uniformity of the crack width leading to a broader distribution of crack width.

Figures 4.23(a) to (c) show the crack width distribution of three-dimensional crack network of OPC-MR-60-152, OPC-MR-60-51, FA-MR-60-127, respectively. From Figure 4.23(a) and (b), it can be seen that both OPC-MR-60-152 and OPC-MR-60-51 have similar crack width distribution between the maximum and minimum value although the frequency of each value of crack width differs. This means that in the same material the range between maximum and minimum crack width could be the same. Despite the slightly smaller crack opening width of FA-MR-60-127 as compared with that of OPC-MR-60-152, smaller range between the maximum and minimum crack width occurred in the FA-MR-60-127 specimen (Figure 4.23(c)). Hence, crack constrictivity as described by crack width distribution is controlled by the distribution and the mean of the crack width along its length.

In principle, the propagation of cracks in concrete always occurs in the weakest areas or areas that require lower energy in order to dissipate the energy due to work load. These areas are the ITZ, unhydrated cement grains, and pores. The presences of these regions in the microstructure of concrete also affect the width of cracks formed by the application of loads. It has been explained that some part of the crack of the specimen OPC-MR-60 were formed in pore cluster while some parts are around the aggregate. Considering that the pores are connected to the crack, the crack width formed in the pore region was generally larger relative to other crack width along crack length. Such condition can obviously lower the degree of the crack width uniformity resulting to an increased variation of crack widths along the crack length. In addition, significant effect of constrictivity occurs on the crack that forms a large difference in its width along the crack length. It is known that the addition of fly ash could decrease the number of pores in the mortar. The spherical shape of some fly ash particles and the pozzolanic reaction products filled the void that no other parts of the mix can fill, thus creating a more dense material resulting to higher compressive strength for FA-MR-60. Thus, the propagation of cracks generally occurred in the area around the aggregate and cement matrix resulting to a more uniform crack width. This means that the cracks that occurred in the specimen FA-06-127 has a higher level of uniformity when compared with the other specimens.

(a)

(b)
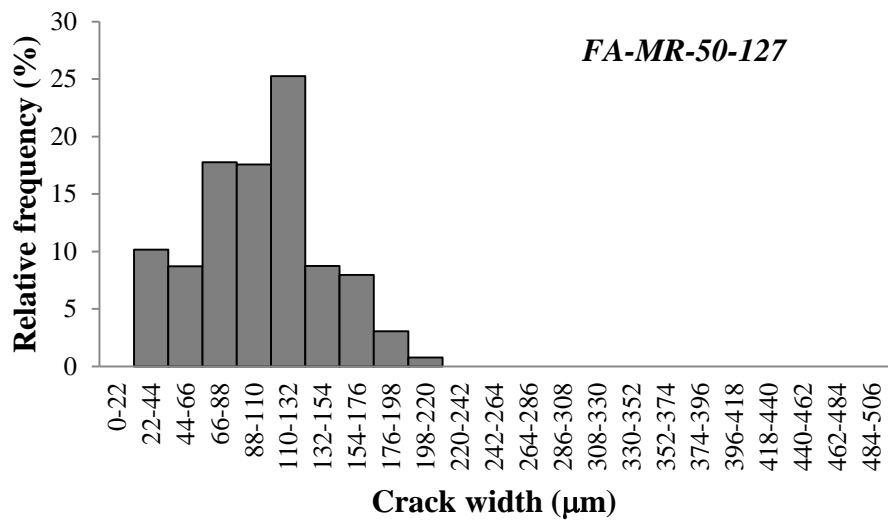
(c)

Figure 4.23 Crack width distributions of (a) OPC-06-152, (b) OPC-06-51,(c) FA-06-127.

4.3.2. Crack geometry for flexural crack

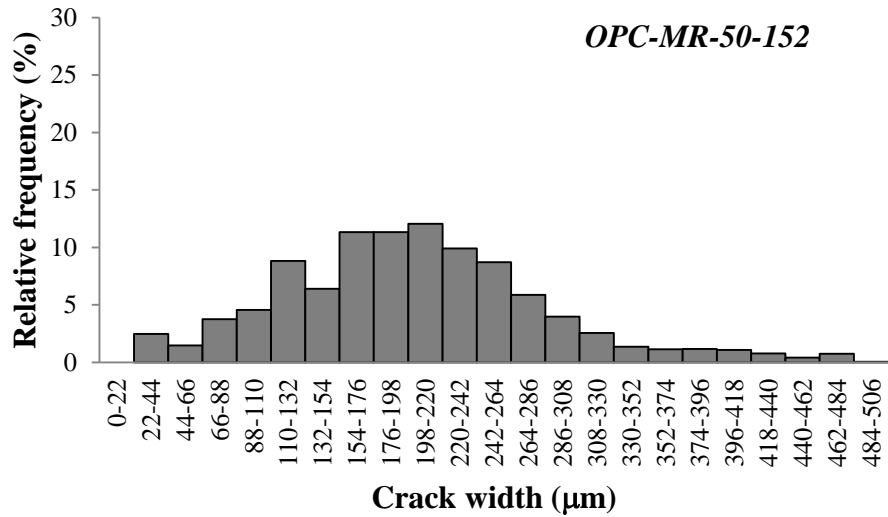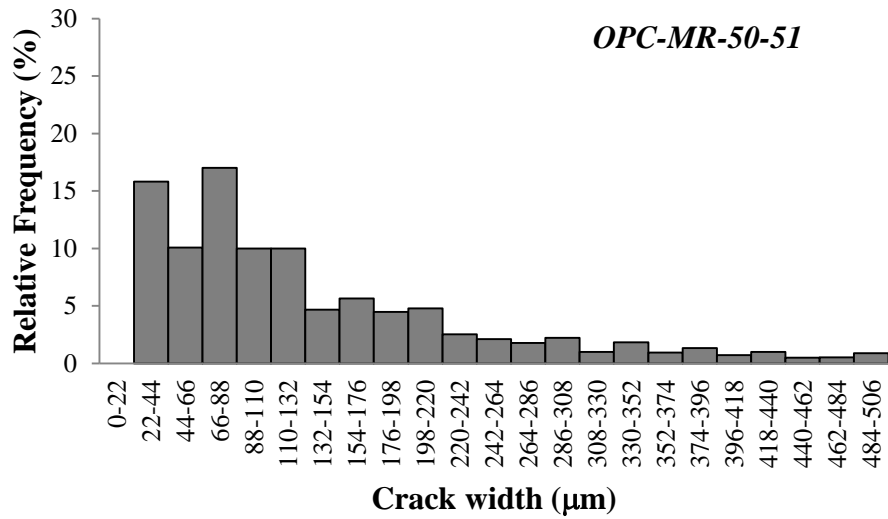Figure 4.24 shows the representative cross-sectional images of cracked beam specimens generated by flexural test. Based on visual observation of the cross-sectional images of both OPC-MR-50 and FA-MR-50 specimen, basically, it is difficult to find fundamental differences in both cross-sectional images because it looks similar. It is certainly different from what was found in the visual observation of the cross-sectional images of splitting tensile cracked specimens in which microstructure of OPC-MR-60 and FA-MR-60 specimen can easily be distinguished by the presence of more pore space appeared in the OPC-MR-60 specimens as compared with FA-MR-60 specimen. In this regard, under similar crack opening width it can be estimated that the crack in the OPC-MR-50 and FA-MR-50 specimen would have similar crack geometry parameter. Therefore, in order to quantify the crack geometry parameter, the cracks in both OPC-MR-50 and FA-MR-50 specimen were extracted from microtomographic image through crack segmentation and cluster multiple labeling processes. In addition, it can be seen that with such a small crack opening width and the application of FRP, the crack depth of OPC-MR-50 and FA-MR-50 specimen were 10.4 mm and 8.8 mm, respectively.

Figure 4.25 visualizes three-dimensional cracks network derived from microtomographic images of flexural cracked specimens after void segmentation and cluster multiple labeling. In general, there is no significant difference between 3D crack network of OPC-MR-50 and FA-MR-50 specimen based on visual observation. This supports the result that has been explained in the visual observation of cross-sectional images of specimens. On the other hand, as shown in Figure 4.25, it can also be seen that some part of crack in both specimens went through the entrapped air void. It is characterized by sudden changes on the size of the crack as shown in Figure X (yellow circle in X-Y coordinate).

Furthermore, the crack geometry parameter will be determined by using 3D crack network shown in Figure 4.25. Table 4.4 summarizes the crack geometry factors derived after extracting the crack from the CT images. The tortuosity is found to be around 1.13 to 1.14. This means that the length of the crack in the specimen, which contains maximum aggregate size of 1.7 mm and a crack that was induced by a flexural test was about 15% longer than the
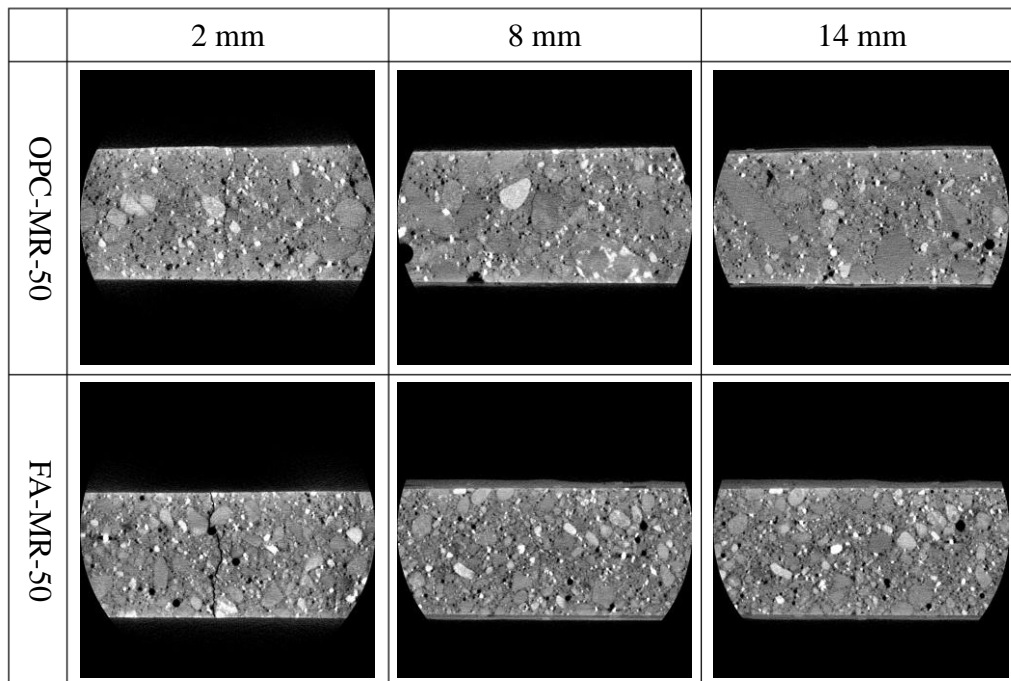
Figure 4.24 Representative cross-sectional images of flexural cracked specimens.
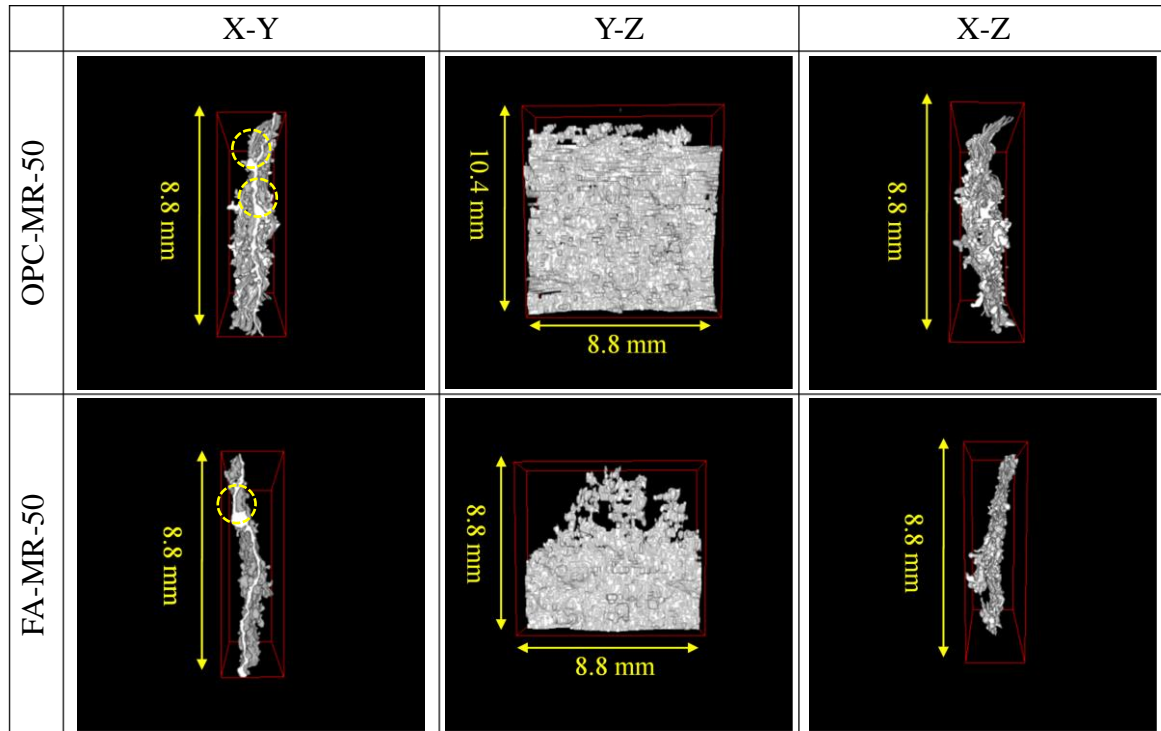
Figure 4.25 Visualization of 3D crack network derived from microtomographic images of flexural cracked specimen.

Table 4.4 The crack geometry parameters of flexural cracked specimen

Specimen	Residual COD (μm)	Tortuosity (τ)	Constrictivity (δ)
OPC-MR-50	20-40	1.14	0.67
FA-MR-50	45-55	1.13	0.70

length of specimen. It is interesting to obtain this finding because without considering the mix proportion and the maximum aggregate was same, the tortuosity of crack that was induced by flexural crack was smaller than that of splitting tensile crack.

The constrictivity of FA-MR-50 specimen was slightly higher but roughly equivalent to that of OPC-MR-50 specimen. This result is reasonable considering the microstructure of both specimens looked similar based on the visual observation of its cross-sectional images. Figures 4.26(a) and (b) show the crack width distribution of three-dimensional crack network of OPC-MR-50 and FA-MR-50, respectively. As shown in Figure 4.26(a) and (b), it can be seen that both OPC-MR-50 and FA-MR-50 have similar crack width distribution between the maximum and minimum value although the frequency of each value of crack width differs. Since crack constrictivity is controlled by the distribution of the crack width along its length, this could be the reason why the constrictivity of FA-MR-50 specimen was slightly higher but roughly equivalent to that of OPC-MR-50 specimen.

However, the constrictivity of flexural crack is quite low considering the maximum crack width occurred in the crack was only the crack formed or went through the isolated porosity. Therefore, the behavior of crack that was induced by flexural test in which the crack width decreases along the crack depth should be the reason in lower constrictivity for flexural crack.
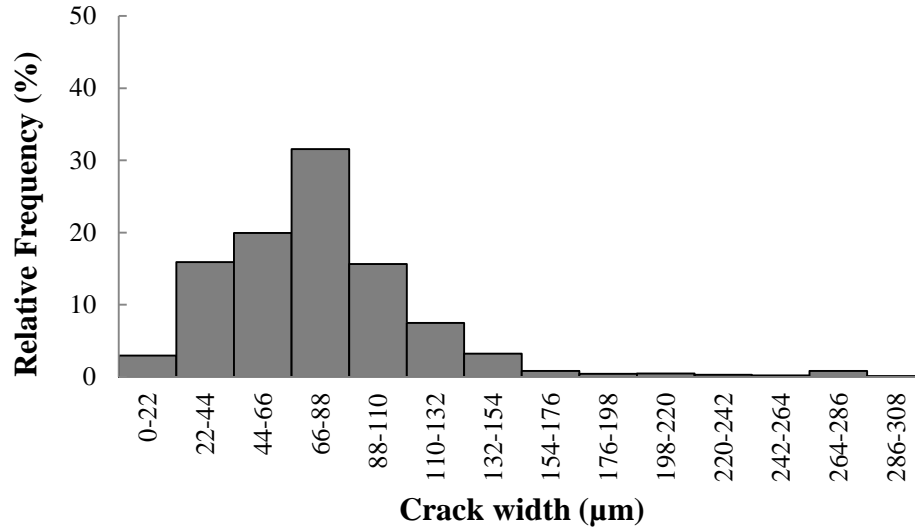
(a)
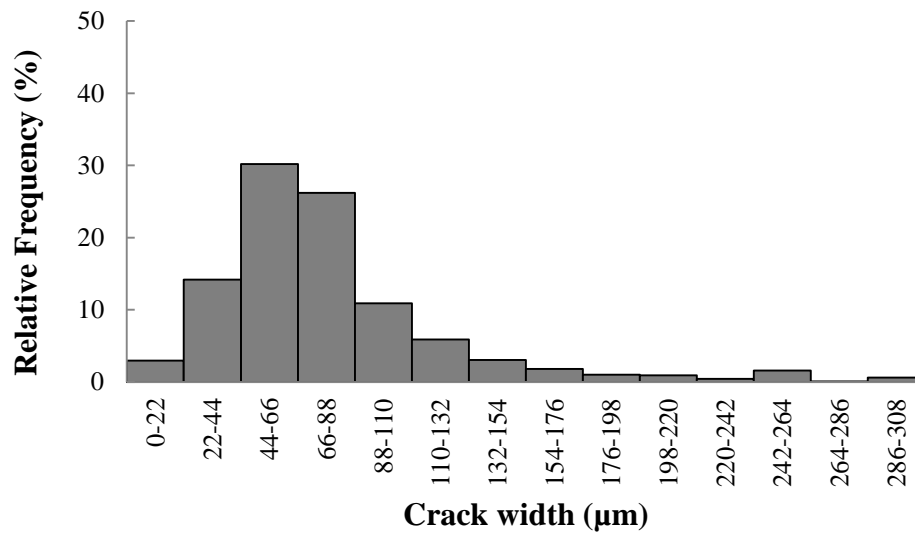
(b)

Figure 4.26 Crack width distributions of (a) OPC-MR-50 (b) FA-MR-50 specimen.

4.4   SUMMARY

Using synchrotron X-ray CT the change in the porosity in the normal cement paste and low alkali binder specimens with increasing curing periods were examined. The pore structure parameters such ash total porosity, connectivity, and pore size distribution were obtained through the analysis of 3D microtomographic images. The total porosity for both normal cement paste and low alkali binder specimens reduced with increasing curing periods. However, a lower rate of decrease in porosity is found in low alkali binder specimen as compared with that of normal cement paste specimen. The slow decrease in porosity of low alkali binder specimen was also followed by a slow decrease in the degree of connectivity of the pore structure. Higher rate of decrease in porosity as well as connectivity led to higher decrease in the larger pore size in the percolated porosity of normal cement paste specimen resulted in slightly finer pore structure as compared with that of low alkali binder specimen. Furthermore, Random Walk Simulation (RWS) was performed to quantify the diffusion tortuosity in the pore structure of each specimen. The diffusion tortuosity of pore structure of

normal cement paste was higher than that of low alkali cement paste at the same curing periods.

After leaching test the pore structure of normal cement paste specimen changed significantly as compared with that of low alkali binder specimen. The total porosity of normal cement paste increased around 2.5 times. Meanwhile, it was 1.25 times in low alkali binder specimen. In this regard, the pore structure of normal cement paste specimen became coarser than that of low alkali binder after leaching test. In addition, after leaching the diffusion tortuosity reduced dramatically to a single digit. On the other hand, although there was a reduction in the diffusion tortuosity for percolated porosity of low alkali binder specimen, however, it was not dramatically when compared with that of normal cement paste specimen.

Furthermore, the application of synchrotron X-ray CT technique was combined with micro-tensile instrument and the observation during the application of load was conducted in-situ inside synchrotron X-ray CT chamber. This experimental method shows us that the application of synchrotron X-ray CT can be combined with other mechanical test and the behavior of microstructure under external load could be observed.

Using micro-focus X-ray CT, the change of pore structure in high strength concrete due to high temperature exposure followed by different re-curing method namely water re-curing and air re-curing was examined. The different type of cracks occurred in the concrete specimen after heating were identified namely interfacial cracks between mortar and coarse aggregates, bridging cracks between aggregates and bridging cracks between aggregates and air voids. The presence of these cracks definitely increased the porosity in the concrete specimen. Both water re-curing and air re-curing after heating reduced the porosity in the concrete specimen. However, water re-curing is more effective in the recovery of microstructure of concrete after high temperature exposure.

Micro-focus X-ray CT was used to examine the crack in the mortar specimens. The cracks in beam specimens of the size of 10 x 20 x 60 mm and cylinder specimens of the size of 20 mm in diameter and 40 mm in height were induced by flexural test and splitting tensile test, respectively. The mechanical properties of specimen play important role on the tortuosity of crack. Under the same maximum aggregate size but with lower compressive strength, the crack tortuosity of splitting tensile crack specimen was higher than that of flexural crack specimen with higher compressive strength. On the other hand, the presence of voids and type of cracks plays an important role on the constrictivity of the crack. The addition of fly ash could reduce the effect of constrictivity in the crack as presence of fly ash decrease the number of voids in the mortar.

CHAPTER 5
DETERMINATION OF SOLID PHASES IN MICROSTRCUTURE OF CEMENTITIOUS MATERIALS

5.1. EVOLUTION OF SOLID PHASES IN MICROSTRUCTURE WITH INCREASING CURING PERIODS.

In this study phase analysis is attempted to differentiate any solid phases present in the microstructure through the observation of LAC histogram. Figures 5.1(a) and (b) show the LAC histogram of OPC-CP-50 and HFSC-CP-50 specimen, respectively. As shown in Figure 5.1 it can be seen the change of LAC histogram with increasing curing periods. At 2 days curing period of OPC-CP-50 specimen, there are two peaks appeared in the histogram. The first peak is the peak with a lower observed LAC and another peak with the higher observed LAC.
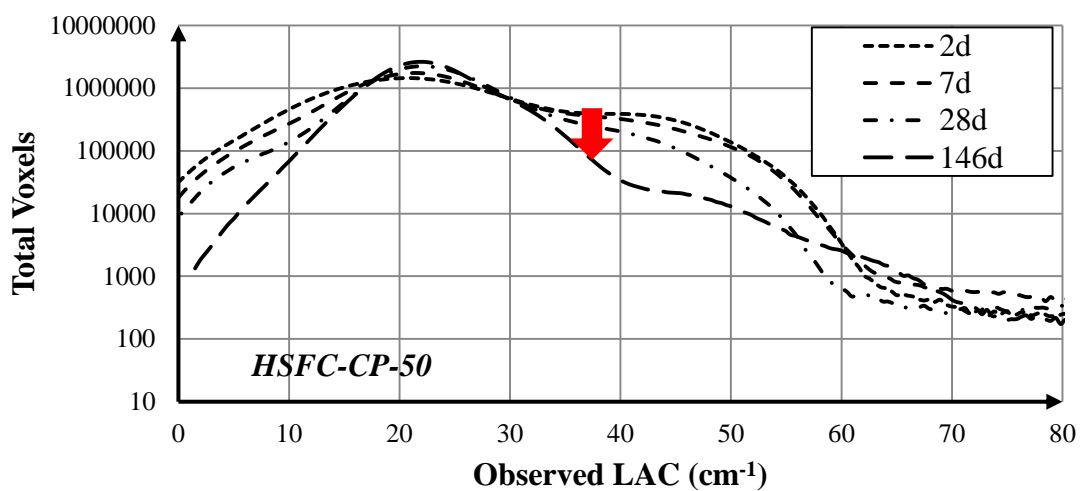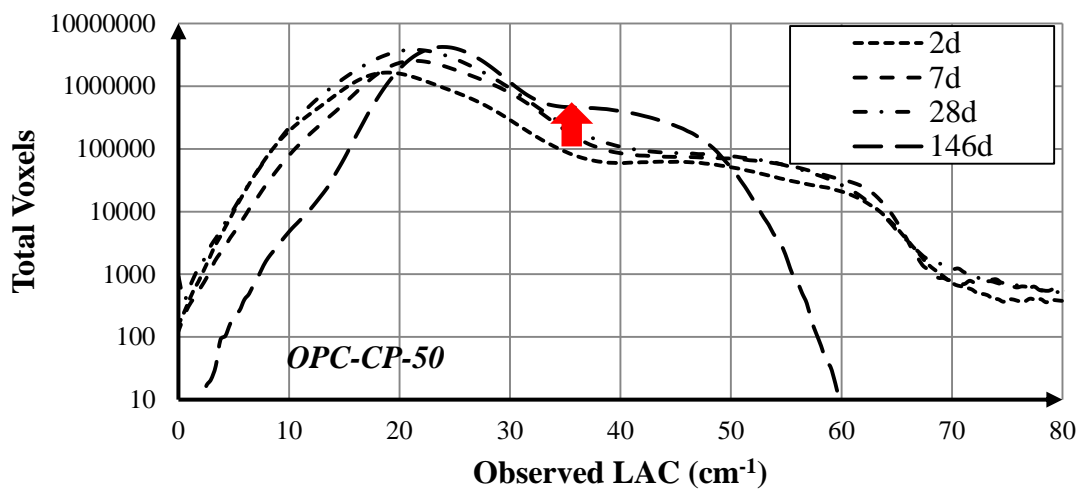

(a)

(b)

Figure 5.1 Observed linear attenuation coefficient (LAC) histogram of (a) OPC-CP-50 and (b) HFSC-CP-50 specimen.

Based on observed LAC values shown in the Table 3.8 and then fitted in the histogram, it is estimated that the first peak may represent either C-S-H (I) or 14Å Tobermorite. Taylor [18] considered that C-S-H (I) is a structurally imperfect form of 14Å Tobermorite, with a similarity in weight fraction and mass attenuation coefficient of its atomic constituent. This could be the reason why both of these phases have similar observed LAC. Unlike phase analysis of the first peak with lower LAC which can be done relatively easily, to identify which kind of phases that are covered in the second peak is quite difficult to be done. This is because the observed LAC of several phases such as CH, and cement clinkers are in this peak range. It is also considered that C-S-H (II) with higher Ca/Si ratio present in the second peak of LAC histogram of OPC-CP-50 specimen. Richardson [110] reported that the C-S-H present in hardened pastes of ordinary Portland cement generally has a mean Ca/Si ratio of about 1.75, with a range of values from 1.2 to 2.1. Thus, based on the observation of LAC histogram, this result may imply that in OPC-CP-50 the C-S-H present in two different structures and it seems similar to C-S-H (I) and C-S-H (II). Furthermore, both peaks in LAC histogram increased in volume with increasing curing periods as the results of hydration process of cement clinkers.

Similar to that of OPC-CP-50 specimen, two peaks appear in the LAC histogram of HFSC-CP-50 specimen at 2 day curing period. The first peak is the peak with a lower observed LAC and another peak with the higher observed LAC. The first peak may represent either C-S-H (I) or 14Å Tobermorite and the second peak may represent CH, C-S-H (II), and cement clinkers. Though the LAC of C-S-H (II) lay within the second peak range, however it does not automatically indicate the presence of C-S-H (II) in the HFSC-CP-50 specimen. As stated by Richardson [110], if a paste contains a supplementary cementing material such as silica fume, fly ash, metakaolin or ground granulated blast-furnace slag then the mean value of Ca/Si ratio is much reduced to less than 1. Meanwhile, García Calvo et al [111] reported that the C-S-H generated with low-pH binders contains Ca/Si ratios between 1.2 and 0.8. In this regard, C-S-H (II) which has Ca/Si ratio of 1.8 may not be found in HFSC-CP-50 specimen. Thus, the second peak of the histogram should refer to CH and cement clinkers. Unlike that of OPC-CP-50 histogram where both peaks increases with increasing curing period, in the LAC histogram of HFSC-CP-50 specimen, only the first peak which represents C-S-H (I) increased and the second peak which represent CH and cement clinkers decreased. Increasing in volume of first peak is caused by both hydration process of cement clinkers and pozzolanic reaction of fly ash. Meanwhile, decreasing of second peak is caused by the reduced volume of CH that used in pozzolanic reaction during curing period.

5.2. PHASE CHANGE BY LEACHING

Figures 5.2(a) and (b) show the LAC histogram of OPC-CP-50 and HFSC-CP-50 specimen before and after leaching test, respectively. As described previously, in the LAC histogram of OPC-CP-50 specimen before leaching formed two peaks which consisted of that with a lower observed LAC and another with the higher observed LAC. The peak with lower observed LAC has a similarity with observed LAC of C-S-H (I) and the peak with higher observed LAC represent several phases due to its wider peak curve such as, CH, C-S-H (II) and cement clinkers. After leaching test in OPC specimen, there are several phenomena that can be observed through the histogram. The first phenomenon which is considered the main problem of leaching is dissolution of CH resulting in decreased volume of CH. Furthermore, there was a shift in the first peak where it moved toward lower observed LAC. This result shows that the decalcification of C-S-H (I) in OPC specimen might occur. Assuming that there is no change in density after reduction in Ca/Si ratio after leaching test, then with the analogy by Eq.(3.2), decrease in observed LAC in the first peak in the histogram shows the decrease of Ca/Si ratio in the C-S-H (I).
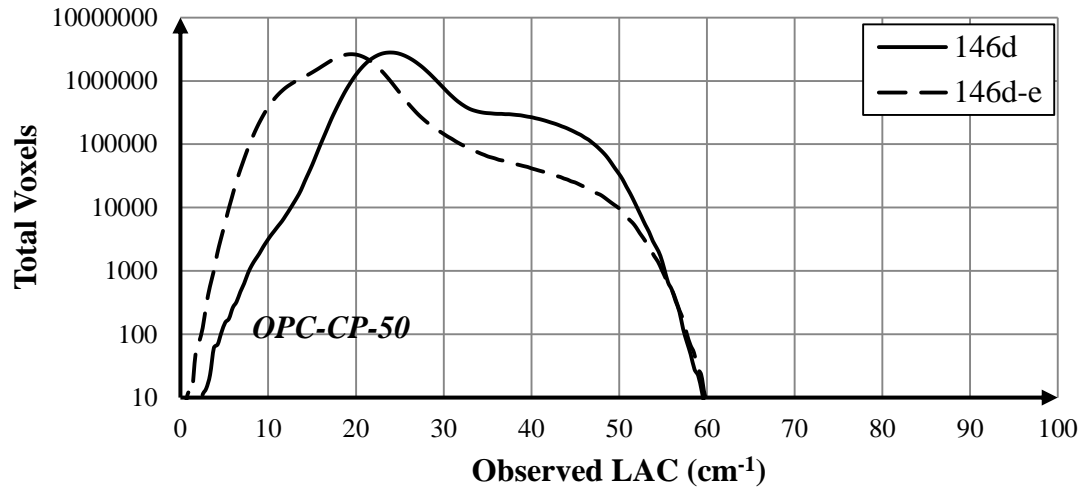
(a)
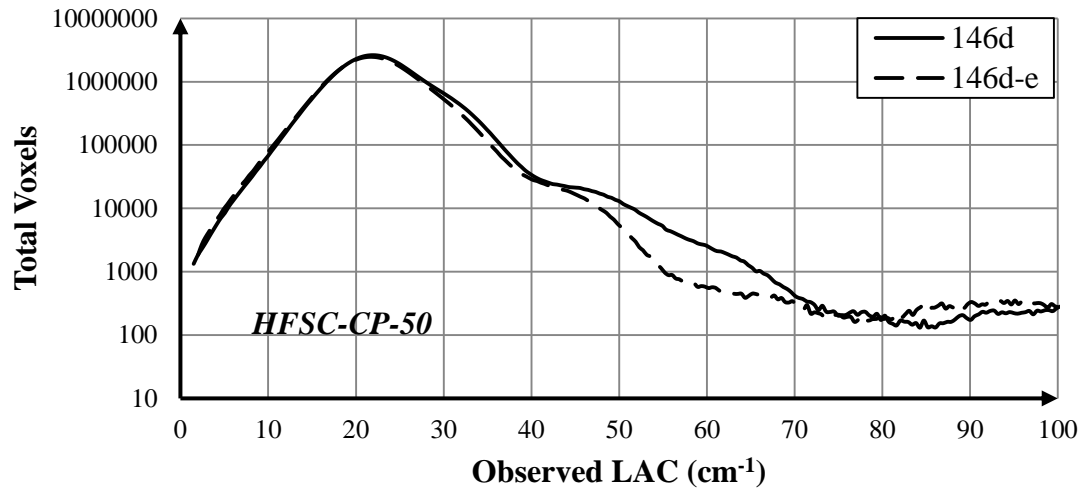
(b)

Figure 5.2 Observed LAC histogram before and after leaching test of (a) OPC-CP-50 and (b) HFSC-CP-50.

The thing that is also interesting is the decrease evenly on the peak region with the higher observed LAC which covered three solid phases in OPC specimens. The total voxel counted near the observed LAC for CH is reduced combined with reduction for other solid phases such as C-S-H (II) and cement clinkers. However it is difficult to ascertain whether there was a reduction in the volume of C-S-H (II) or cement clinkers during the leaching test. This is because observed LAC of C-S-H (II) is close to that of cement clinkers especially C_3A. Considering that the low density of C-S-H phase (C-S-H (I)) appears to be more vulnerable to chemical degradation than the dense C-S-H (C-S-H (II)) [112], it can be estimated that there was a decrease in the volume fraction in the cement clinkers instead of C-S-H (II) during the leaching test so that the total voxel C-S-H (II) after leaching test reflects the initial volume of C-S-H (II) before the leaching test.

In addition, the number of the total voxel near the LAC around 10 cm^{-1} increases largely. This implies the secondary products after leaching test for the OPC. According to the observed LAC these may be Ettringite and Quartz. Faucon et al [113] reported that Ettringite as second precipitations was observed in the OPC degraded paste. Haga et al [114] estimated

that the Ettringite observed was considered to be a secondary mineral formed in the process of hydrate dissolution. For the presence of Quartz it may be due to the decalcification of C-S-H or the migration of silica ions under the given electrical field. In order to verify these secondary products observed in the deteriorated OPC further chemical analysis is necessary in the future.

On the other hand, as shown in Figure 5.2(b), the same trend between before and after leaching test in the distribution of LAC is found in HFSC-CP-50 specimen, while the total voxel of the first peak which represent C-S-H (I) is slightly decreased. This result implies that the deterioration of HFSC specimen occurred due to the decalcification of C-S-H (I) instead of dissolution of CH. In this way, it is shown that with a small amount of CH left behind after its consumption by pozzolanic reaction the calcium would leach away from C-S-H phase. In addition, the pH of the leaching solution at 13 weeks of the natural leaching test of HFSC specimen was smaller than 10.5 [115]. By considering the chemical composition of leaching solution similar with that of pore water solution, this result has good agreement with those reported by previous researcher where the pH of pore water solution lay within 12.6 and 10.0 after the dissolution of calcium from the C-S-H [116-118].

5.3. FLY ASH PARTICLES

This research also reveals the presence of different types of fly ash particles in cementitious materials mixed with fly ash. Two types of fly ash particles were detected in cementitious materials mixed with fly ash, such as either low or high density fly ash particle and a fly ash particle in form of a cenosphere. Figure 5.3(a) may show the low density fly ash particle. From the analysis of LAC histogram of line segments as shown in Figure 5.3 (a), it may say that the fly ash particle exists in hydration products of a solid phase

Figure 5.3(b) shows the unreacted fly ash particle in form of cenosphere. Visually, microtomographic image of cenosphere is similar to a sphere with high density shell that encloses a low density phase or void therein. This fly ash particle (cenosphere) may not react during curing periods and remained in its original form although the hydration products such as CH present around this particle. Using synchrotron X-ray microtomography, Provis et al [106] observed the paste specimens that were generated by fly ash and granulated blast furnace slag. They found that up to 45 days curing, the presence of fly ash particle in the form of a perfectly round sphere with low density materials or void inside the sphere still exists. It is estimated that high density shell of this fly ash particle may hinder the reaction with hydration products.

Furthermore, another unreacted fly ash particle was detected in the microtomographic images of fly ash mortar as shown in Figure 5.3(c). This fly ash particle has a spherical form with a high density. Based on the observation of observed LAC histogram, this particle has a similarity in observed LAC value to the Magnetite and Hematite. Considering the relatively higher density of both Magnetite and Hematite given in Table 3.8 (25 keV), it is estimated that this fly ash particle shown by high contrast in microtomographic images might contain both. Similar to that of cenosphere, this unreacted fly ash particle will not react during curing periods and remained in its original form.

5.4. SUMMARY

The evolution in the solid phases in the microstructure of normal cement paste specimen and low alkali binder specimen with different curing periods were evaluated by using synchrotron X-ray CT on the basis of linear attenuation coefficient (LAC). The changes in the volume of each solid phase in the microstructure of both normal cement paste specimen and low alkali binder specimen due to increasing curing period were observed through the changes in the LAC curve. The fundamental difference in the evolution of solid phases

between normal cement paste specimen and low alkali binder specimen was clearly seen in the LAC histogram. The different lies in the area of LAC histogram which represent the presence of CH. This area experienced an increase in its volume for normal cement paste specimen while it was decreased for low alkali binder specimen with increasing curing periods.
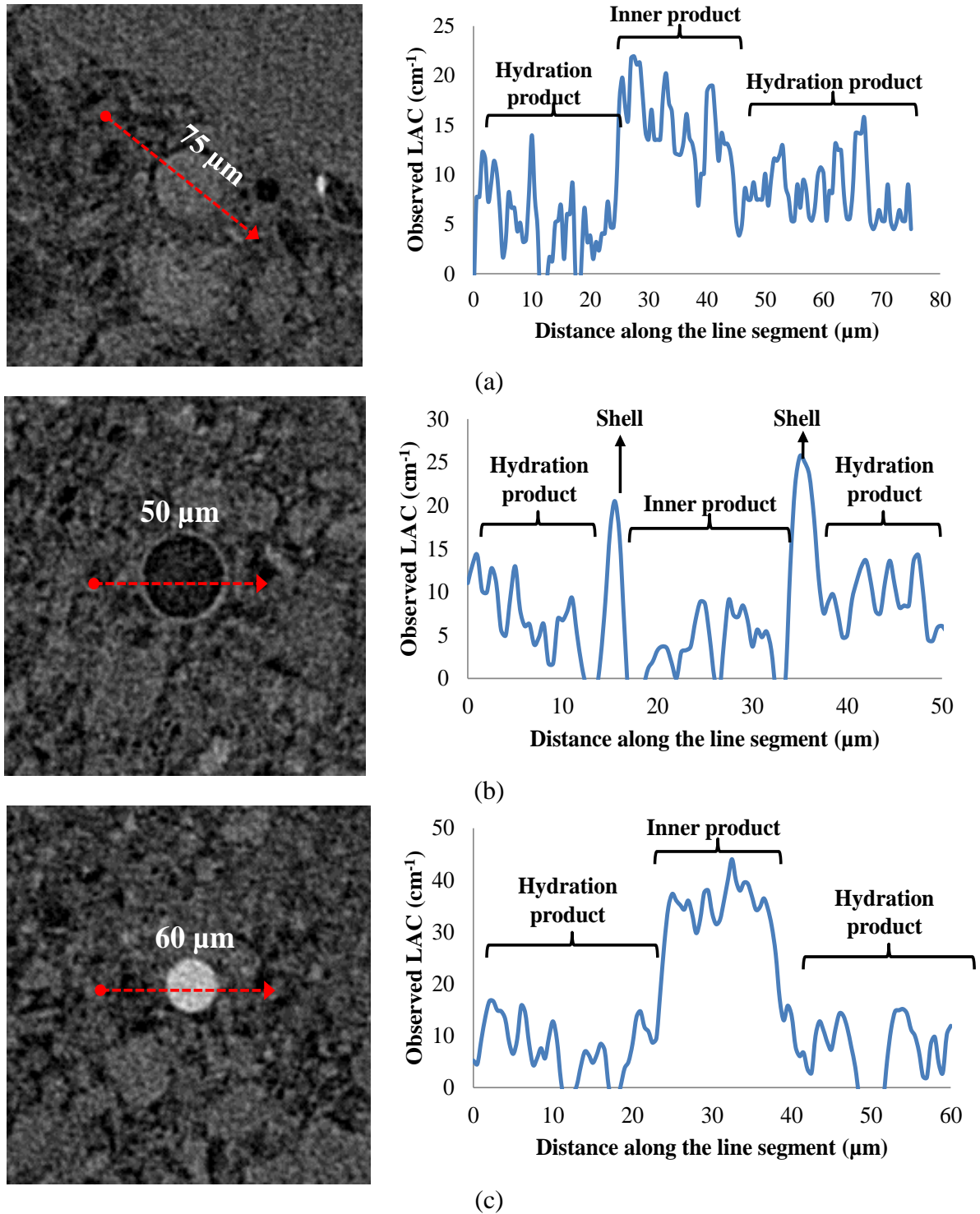

(a)

(b)

(c)

Figure 5.3 Different types of fly ash particle detected in microtomographic image (a) low density fly ash particle, (b) Cenosphere, (c) high density fly ash particle.

Furthermore, using the same technique the change in the solid phase due to leaching was also evaluated. The changes in the LAC histogram of normal cement paste specimen after leaching test looks more complex than that of low alkali binder specimen. Several parts in the LAC histogram of normal cement paste specimen changed both in its volume as well as its LAC value. This indicates that the microstructure of normal cement paste specimen underwent significant change. Meanwhile, although there is a change in the LAC histogram of low alkali specimen, however, it just is limited to the change of volume of specific area in its LAC histogram.

In addition, on the basis of LAC measured for specimen mixed with fly ash two types of fly ash particles were detected; namely either low or high density fly ash particles and a fly ash particle in form of a cenosphere.

CHAPTER 6
QUANTIFICATION OF TRANSPORT PROPERTIES IN CRACKED CEMENTITIOUS MATERIALS

6.1. OVEN-DRIED CRACKED CEMENTITIOUS MATERIALS

Figure 6.1 visualizes microtomographic images of OPC-MR-50 and FA-MR-50 specimen after 24 hours cesium tracer diffusion test. As shown in Figure 6.1, it is known that the aggregates have a higher grey scale value shown with higher color intensity before cesium tracer diffusion test. This is because the aggregate generally has a higher density as compared with any solid products in hardened cementitious materials. However, after cesium tracer
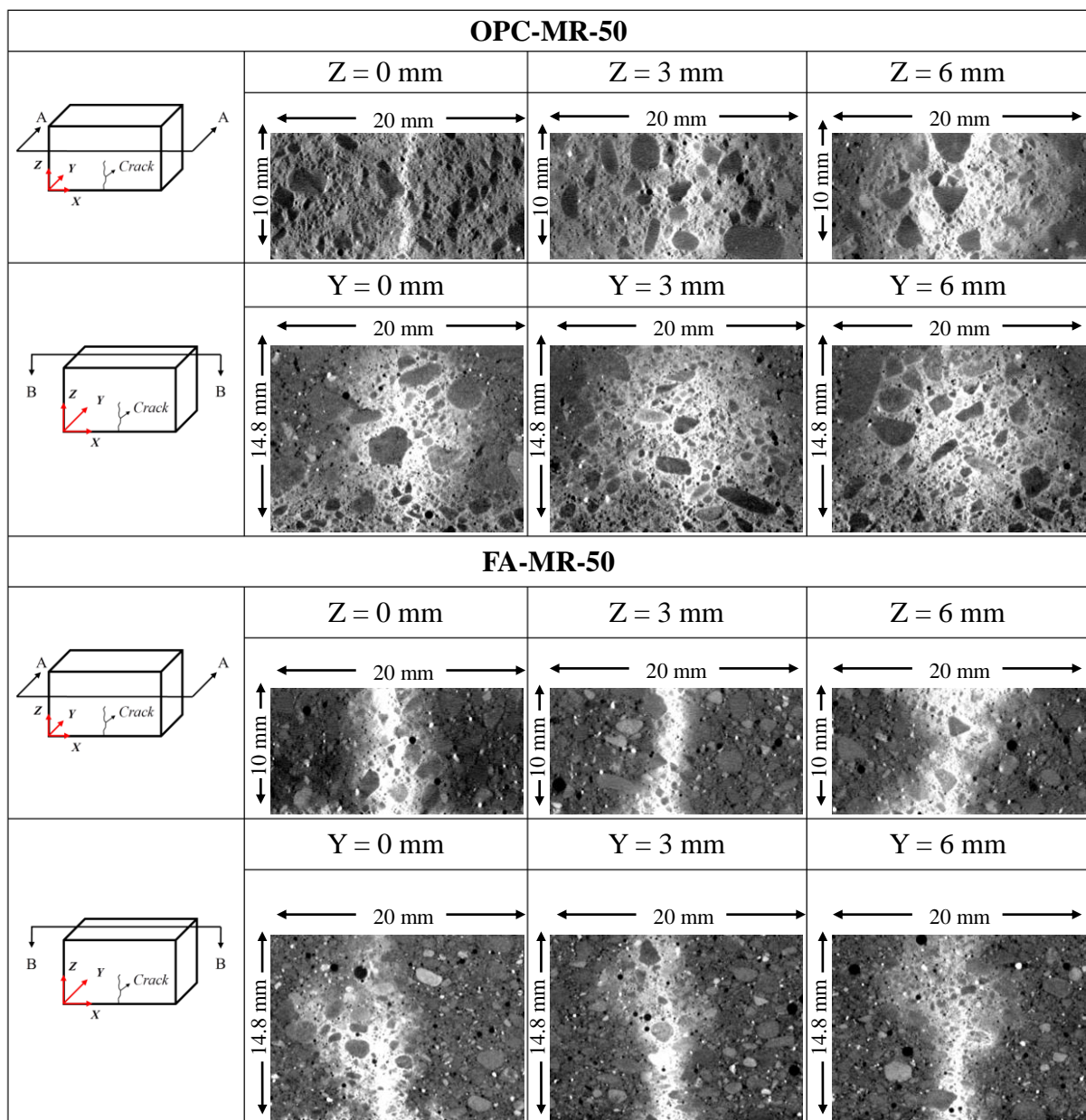

Figure 6.1 Visualization of cesium tracer diffused in cracked cementitious material after 24 hours.

diffusion test, it is found that color intensity of aggregates become lower than that of initial condition under X-ray CT observation. This is certainly due to the presence of cesium tracer which has higher density than the aggregate. In this way, the presence of cesium tracer can be easily distinguished in the microtomographic image of the cesium tracer diffused specimen.

From Figure 6.1, it can be seen that high intensity of white color which represents the presence of cesium tracer appears in the crack area and fading along the uncracked matrix. This means that crack becomes the main channel in the movement of solute in the cracked cementitious material during cesium tracer diffusion test. Thus, it has been proven that the crack can act as a preferential channel for any solute to diffuse in the cracked cementitious material. Furthermore, it can also be seen that the intensity of white color, which represents the cesium tracer, in crack area of FA-MR-50 specimen higher than that of OPC-MR-50 specimen at the same distance from surface exposed to the solution. This indicates that the concentration of cesium tracer in the crack of FA-MR-50 is higher than that of OPC-MR-50 specimen. This phenomenon should be related to the diffusivity of cesium tracer toward the uncracked matrix. As shown in Figure 6.1, it is found that the transport distance of cesium in uncracked matrix of FA-MR-50 specimen is smaller than that of OPC-MR-50 specimen. In this regard, the FA-MR-50 specimen has a higher density in its uncracked matrix leading to increased resistance to diffusivity. Therefore, increased resistance against the diffusivity in the uncracked matrix resulted in higher concentration of cesium tracer in the crack space.

The presence of air void also affect to the diffusivity in uncracked matrix. As shown in Figure 6.1 cesium tracer does not diffuse in the air void. In this regard, the air void which cannot be diffused by cesium tracer is defined as an isolated pore with high inner pressure. In addition, it also can be seen that the cesium tracer did not diffuse in the aggregate as well. This is certainly due to high density of the aggregate. So that in the diffusion process, cesium tracer will move around the aggregate through the interface area between aggregate and hardened cement matrix (ITZ) to reach area with a lower concentration gradient. This result implies that the presence of isolated pores and aggregates influence the diffusivity of solute in uncracked matrix of cracked cementitious materials.

Furthermore, the concentration of cesium tracer both in crack and uncracked matrix needs to be determined from microtomographic images on the basis of CT number in order to conduct quantitative analysis of diffusivity in cracked cementitious materials. Figures 6.2(a) and (b) show the solute concentration profile of OPC-MR-50 and FA-MR-50, respectively. It can be seen that a higher concentration was found near the surface exposed to the solution and
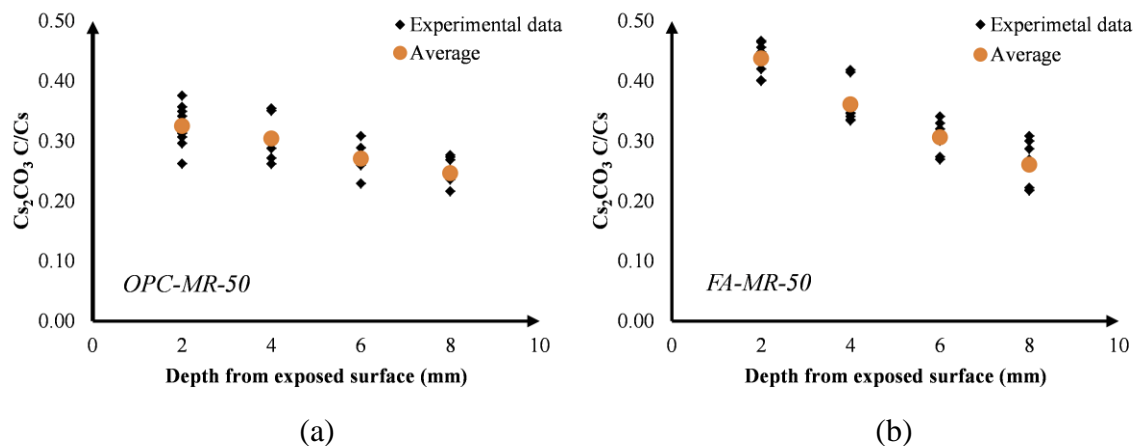

(a)   (b)

Figure 6.2 Profile of cesium tracer concentration in the crack of (a) OPC-MR-50 and (b) FA-MR-50 specimen.
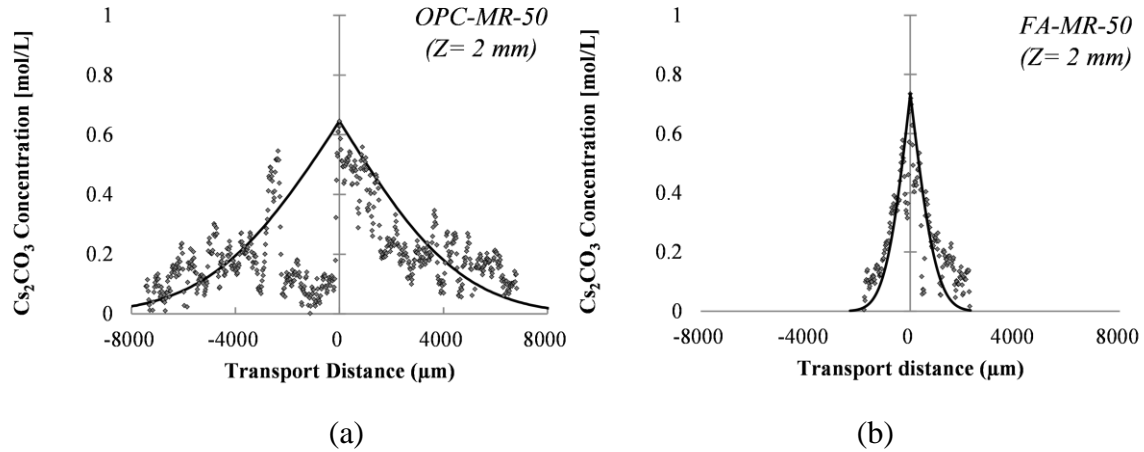
(a)   (b)

Figure 6.3 Representative of cesium tracer concentration profile in uncracked mortar of (a) OPC-MR-50(b) FA-MR-50 at 2 mm from surface exposed to the solution.

reduced along the crack depth. This means that diffusion occurs along the crack passage. On the other hand, Figure 6.2 shows that the concentration of cesium tracer in the crack of FA-MR-50 specimen is always higher than that of OPC-MR-50 specimen at the same distance from exposed-surface to the solution. This is of course in accordance with the results obtained by visual observation of the cross-sectional images of the cesium tracer diffused specimen.

Figures 6.3(a) and (b) show the representative of cesium tracer concentration profile in uncracked matrix at 2 mm from the surface exposed to the solution of OPC-MR-50 and FA-MR-50 specimen, respectively. High concentration of cesium tracer is detected in the center of the curve which represents the crack and reduced along the uncracked matrix. Moreover, as shown in Figure 6.3(a) cesium tracer concentration profile of OPC-MR-50 in the left side of the crack is different with right side. A low concentration of cesium tracer is detected up to 2000 μm from the crack wall and suddenly increased over this region. This region actually represents the presence of aggregate along the diffusion path of cesium tracer. This finding shows that during diffusion process cesium tracer will move around the aggregate instead of penetrating into its matrix. Furthermore, in accordance with the results obtained from visual observation of its cross sectional image, the transport distance of cesium tracer in uncracked matrix of OPC-MR-50 specimen is greater than that of FA-MR-50 specimen at the same level from surface exposed to the solution as shown in Figure 6.3.

The diffusion coefficient along the crack is determined from the best-fitted curve of Fick's second law. Table 6.1 shows the diffusion coefficient along the crack for both specimens. The diffusion coefficient along the crack (D_{cr}) for OPC-MR-50 specimen was 1.70×10^{-09} m^2/s and it was 9.30×10^{-10} m^2/s for FA-MR-50 specimen. From the Table 4.4 we know that the crack constrictivity of FA specimen was higher than that of OPC specimen. This means that the movement of solute inside the crack space of FA specimen should be more

Table 6.1 Diffusion coefficient of unsaturated specimen

Sample	Crack opening width (μm)[*1]	Diffusion Coefficient (m^2/s)	
		D_{cr}	D_{ucr}[*2]
OPC-MR-50	20-40	1.70×10^{-09}	9.12×10^{-11}
FA-MR-50	45-55	9.30×10^{-10}	3.47×10^{-12}

[*1] Measured by microscope, [*2] Apparent diffusion coefficient

fluent than that of OPC specimen from constrictivity factor point of view. However, as given in Table 6.1, the cesium diffusion coefficient along the crack (D_{cr}) of OPC specimen is greater than that of FA specimen. We suggest that in the oven-dried condition, the constrictivity of crack has less influence on the transport mechanism of solute in the crack space due to a higher rate of solute under the capillary absorption mechanism. In addition, it can be noted that the diffusion coefficient of cesium in such a small crack opening width and under oven-dried condition almost reached the diffusion coefficient of cesium in free water (2.06×10^{-9} m^2/s [119,120].

The average apparent diffusion coefficients of uncracked body (D_{ucr}) for OPC and FA specimens were 9.12×10^{-11} and 3.47×10^{-12} m^2/s, respectively. In general, at 28 days curing period the diffusivity of ions in fly ash concrete is higher than that of OPC concrete due to slow in pozzolanic reaction. However, in this research the drying process before penetration test enhanced the pozzolanic reaction. This resulted in the increased resistance to diffusivity due to the dense microstructure for FA specimen. In addition, reduced diffusion coefficient for uncracked matrix in the FA specimen could be related to the lower diffusion coefficient along the crack in the FA specimen.

6.2. PARTIALLY SATURATED CRACKED CEMENTITIOUS MATERIALS

Figures 6.4, 6.5 and 6.6 visualize microtomographic images of initial (after immersion for 24 hours) and after cesium tracer diffusion test of OPC-MR-60-51, OPC-MR-60-152 and FA-MR-60-127, respectively. The X-ray CT scan was conducted after 1, 3, 9, and 24 hours diffusion test. Before cesium tracer test, the presence of aggregates which have higher density as compared with cement paste matrix can easily be distinguished in microtomographic images due to high grey scale value. Furthermore, after cesium tracer diffusion test, the color intensity of aggregates becomes lower than that of initial condition under X-ray CT observation but still can be distinguished with cement paste matrix. This is certainly due to the presence of cesium tracer which has higher density than the aggregate. Accordingly, the highest color intensity appeared in the microtomographic images of each specimen after diffusion test must be related to the presence of cesium tracer.

For OPC-MR-60-51, the results of the visual observation of microtomographic images after 1 hour of diffusion test show that there is no change in color intensity both in the area of the crack and the uncracked matrix at any height from surface exposed to the solution. Furthermore, visual observation that was carried out on the microtomographic images after 3 hours of diffusion test also show similar result in which the presence of cesium tracer is not found either in the crack area or the uncracked matrix. Subsequently, the presences of cesium tracer are detected in microtomographic images after 9 hours of diffusion test. However, it was only detected in the area of crack and at the height less than 9 mm from surface exposed to the solution. The presence of cesium tracer becomes more visible after 24 hours of diffusion test. In this condition, cesium tracer was detected not only in the area of the crack but also into the uncracked matrix. Although cesium tracer was detected up to the height of 9 mm from the surface exposed to the solution, based on visual observation the difference between the 9 hours and 24 hours at this height is not significant. Accordingly, it can be estimated that the concentration of cesium tracer at this height is very low.

If we look more details at the microtomographic images after 24 hours diffusion test, we find that the cesium tracer hardly fills the whole crack space. It seemed that less than half of crack space was occupied by cesium tracer. In addition, even after 24 hours of diffusion test the area of the uncracked matrix that was diffused by cesium tracer was small. This condition certainly related to the small amount of cracked filled by cesium tracer as well as to the low concentration of cesium tracer in the crack.

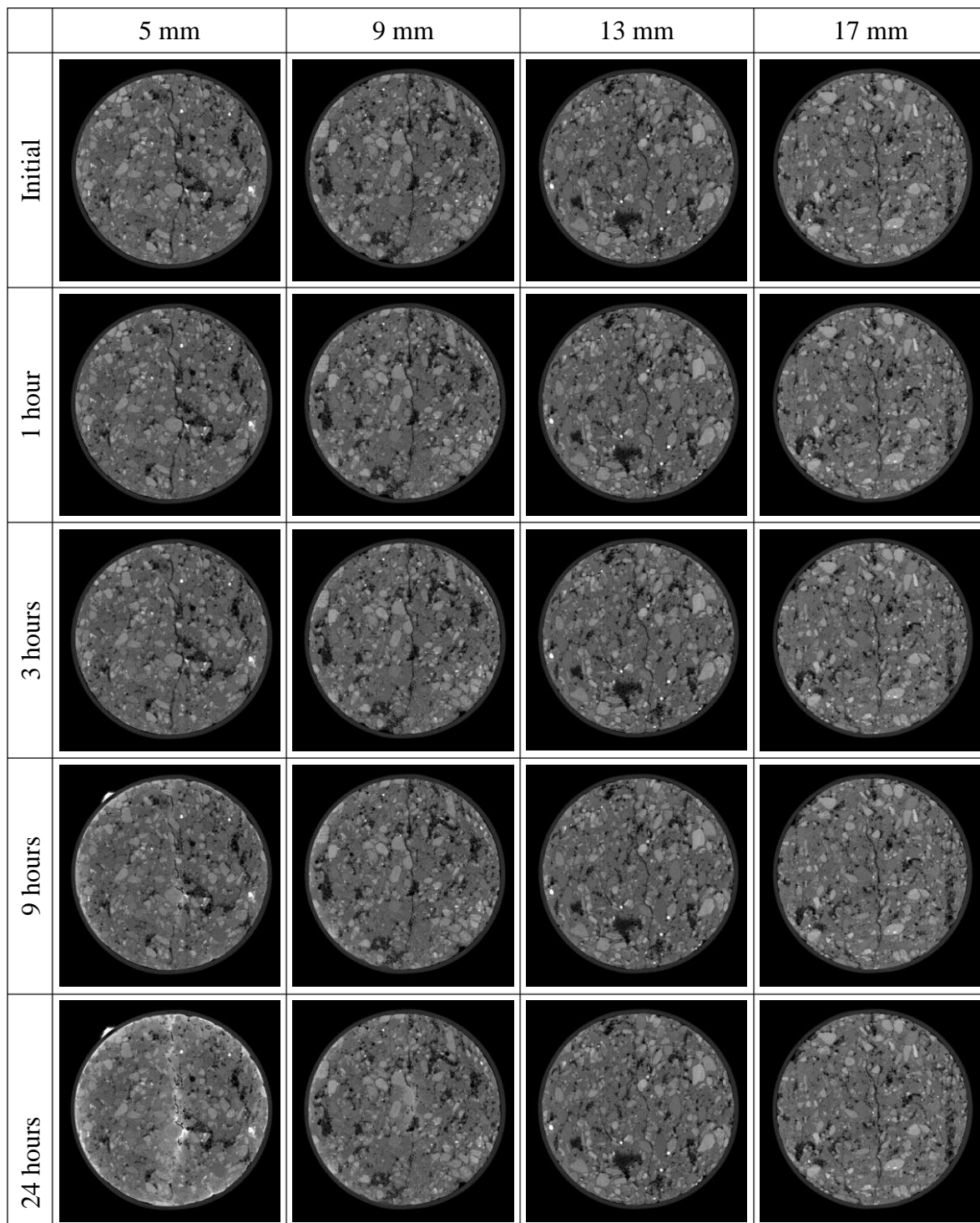|	5 mm	9 mm	13 mm	17 mm
Initial				
1 hour				
3 hours				
9 hours				
24 hours				

Figure 6.4 Visualization of cesium tracer diffused in OPC-MR-60-51 specimen.

For OPC-MR-60-152 specimen just 1 hour after diffusion test, the presence of cesium tracer has been detected crack space as shown in the Figure 6.5. This was totally different from that of OPC-MR-60-51 in which the presence of cesium tracer was detected in longer exposure time. In this regard, it can be seen that the crack opening width plays an important role on the diffusivity in the cracked cementitious materials. However, there was still some of crack spaces which are hardly filled by cesium tracer. Although cesium tracer has been detected in the most of crack spaces, it was difficult to determine the presence of cesium

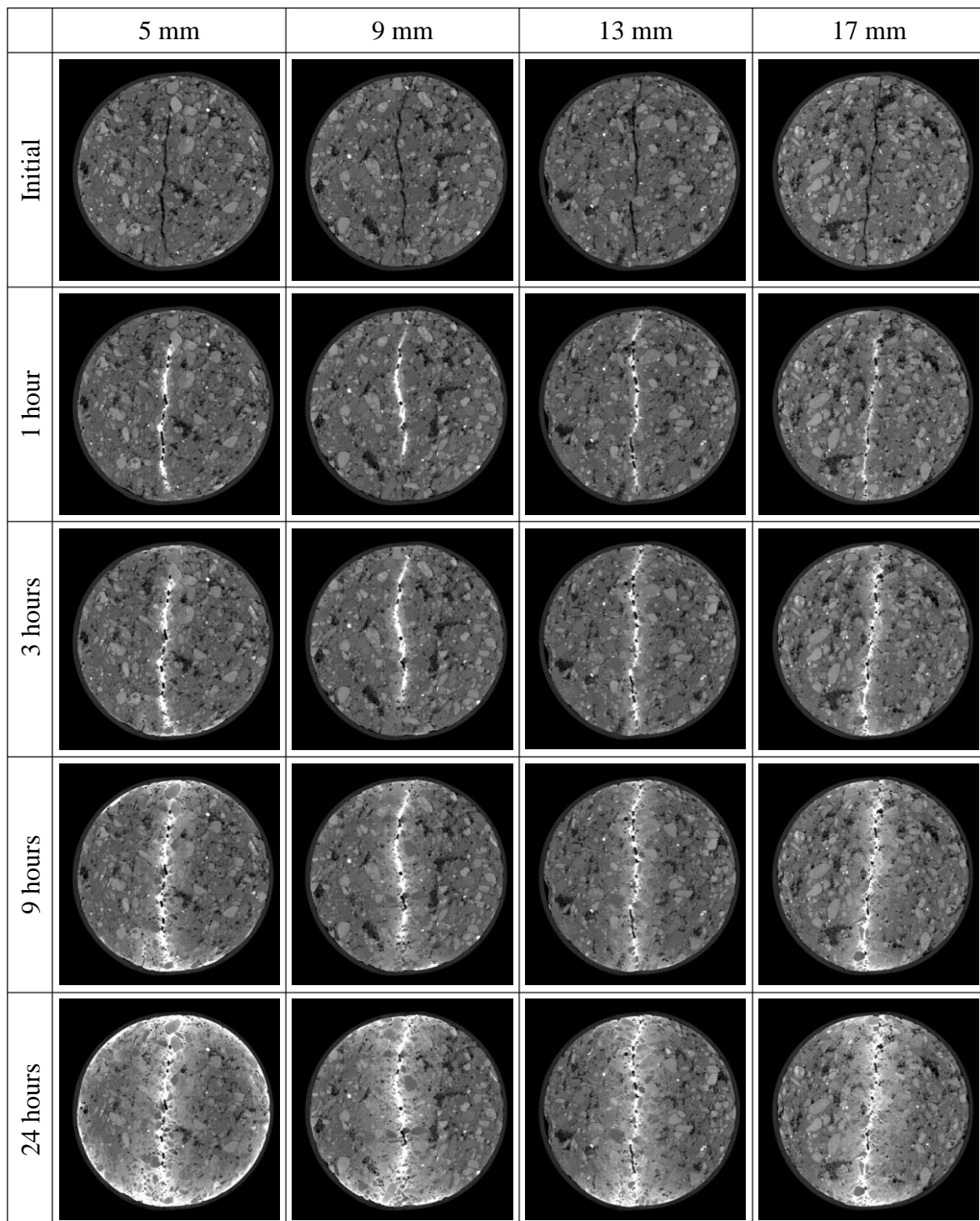|	5 mm	9 mm	13 mm	17 mm
Initial				
1 hour				
3 hours				
9 hours				
24 hours				

Figure 6.5 Visualization of cesium tracer diffused in OPC-MR-60-152 specimen.

tracer in the uncracked matrix based on visual observation of its microtomographic images. In this way, it was estimated that the transport distance of cesium tracer toward the uncracked matrix after 1 hour diffusion test was small. Furthermore, visual observation that was perfomed on the microtomographic images after 3 hours of diffusion test showed that there was no addition of crack space filled by cesium tracer, and even after 24 hours of diffusion similar result was observed. In this way, the diffusion of cesium tracer only followed the path that formed in the short period of exposure time. However, the area of the uncracked matrix

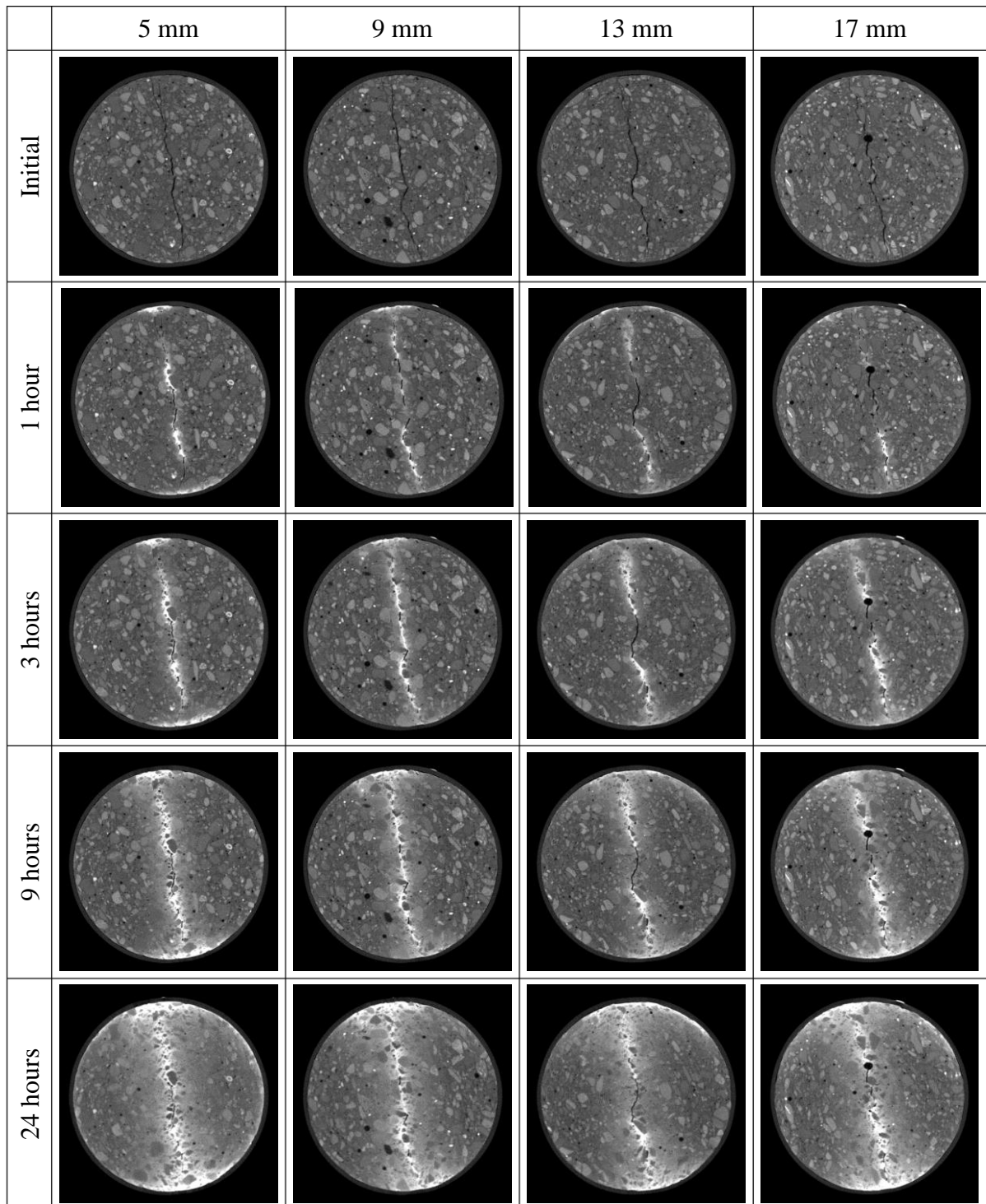|	5 mm	9 mm	13 mm	17 mm
Initial				
1 hour				
3 hours				
9 hours				
24 hours				

Figure 6.6 Visualization of cesium tracer diffused in FA-MR-60-127 specimen.

that was filled by cesium tracer increased with increasing exposure time. In addition, it also can be seen that during the diffusion process of cesium tracer toward the uncracked matrix, cesium did not diffuse both in air void and the aggregate.

Similar with that of OPC-MR-60-152 specimen, the presence of cesium tracer in the crack of FA-MR-60-127 specimen was detected after 1 hour exposure time based on the visual observation of the microtomographic images as shown in Figure 6.6. However, the amount of crack space that was not filled by cesium tracer was higher than that of

OPC-MR-60-152 specimen. In this way, the crack opening width has an effect on the amount of crack space filled by cesium tracer. Furthermore, for the next exposure time, FA-MR-60-127 specimen showed similar trend to that of OPC-MR-60-152 in which there was no addition of crack space filled by tracer and the transport distance of cesium tracer toward the uncracked matrix increased with increasing exposure time.

On the other hand, it is difficult to predict why there are some of crack spaces which are hardly filled by cesium tracer through visual observation alone. Therefore, on the basis of CT number we try to observe those region in more details. Figures 6.7(a) to (d) show the
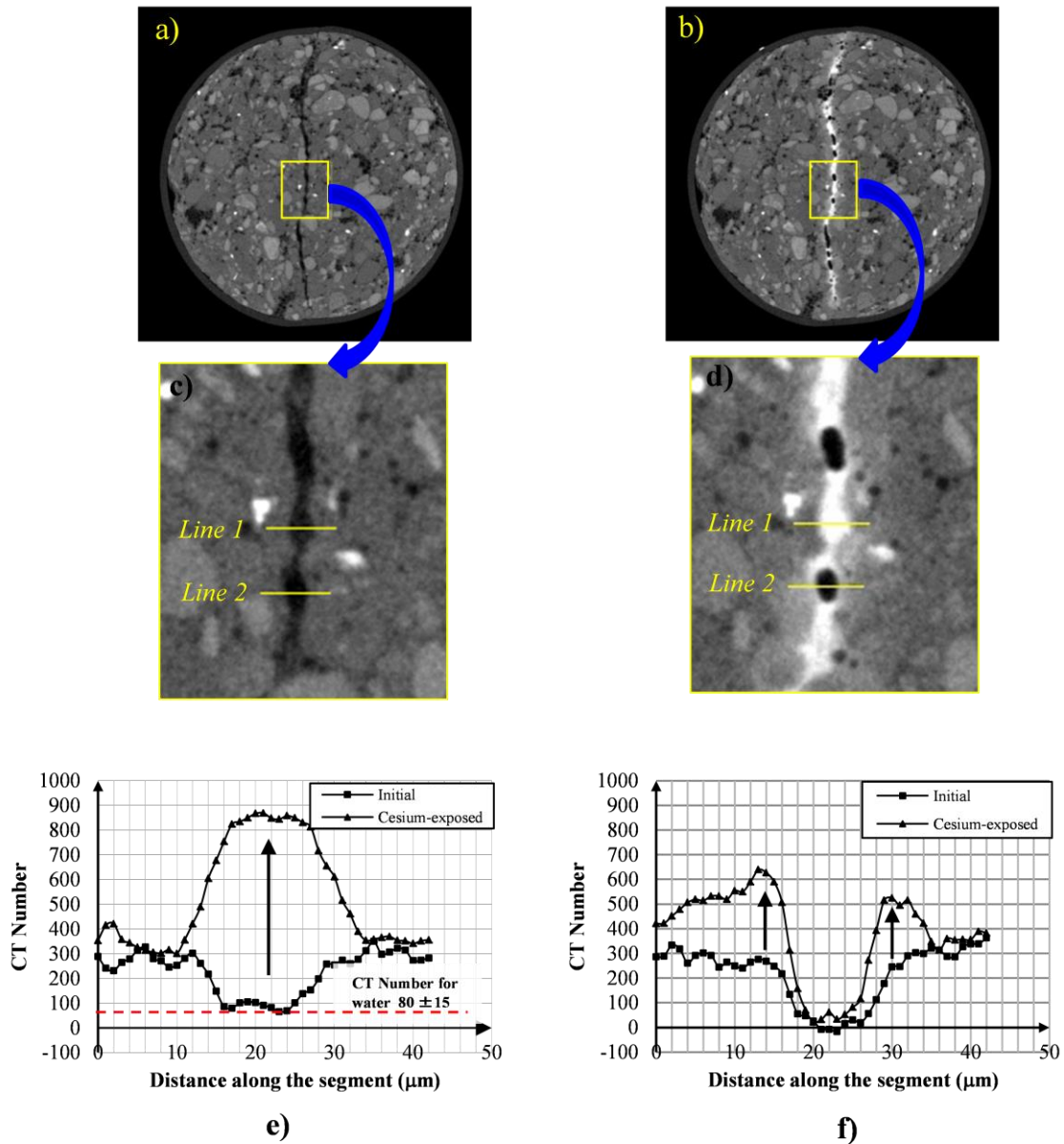

Figure 6.7 Diffusion of cesium tracer in the crack (a) Representative microtomographic image of OPC-MR-60-152 in initial condition (13 mm from solution-exposed surface), (b) After 1 hour exposure time, (c) Line section applied to obtain CT number profile in initial condition and solution-exposed condition as shown in (d),(e) CT number profile of saturated crack in initial and exposed condition in **line 1**,(f) CT number profile of unsaturated crack in initial and exposed condition in **line 2**.

representative microtomographic image of cross section of OPC-MR-60-152 specimen in intial condition and after 1 hour exposure time in the diffusion test. In Figure 6.7(b) and (d) the presence of tracer in the crack is shown in white because of its large CT numbers led to higher grey scale value. It has been described that the images produced in short periods of exposure time show that the tracer did not fill the entire cavity of cracks.

Further observation with the line profile of the CT number (Figure 6.7(e) and (f)) provides the finding that the tracer only fills the crack occupied by water. It was thought that the water absorption phenomena in crack during 24 hours pre-soaking periods did not produce fully saturated crack, and leaving behind air pockets.The presence of air in the crack could be
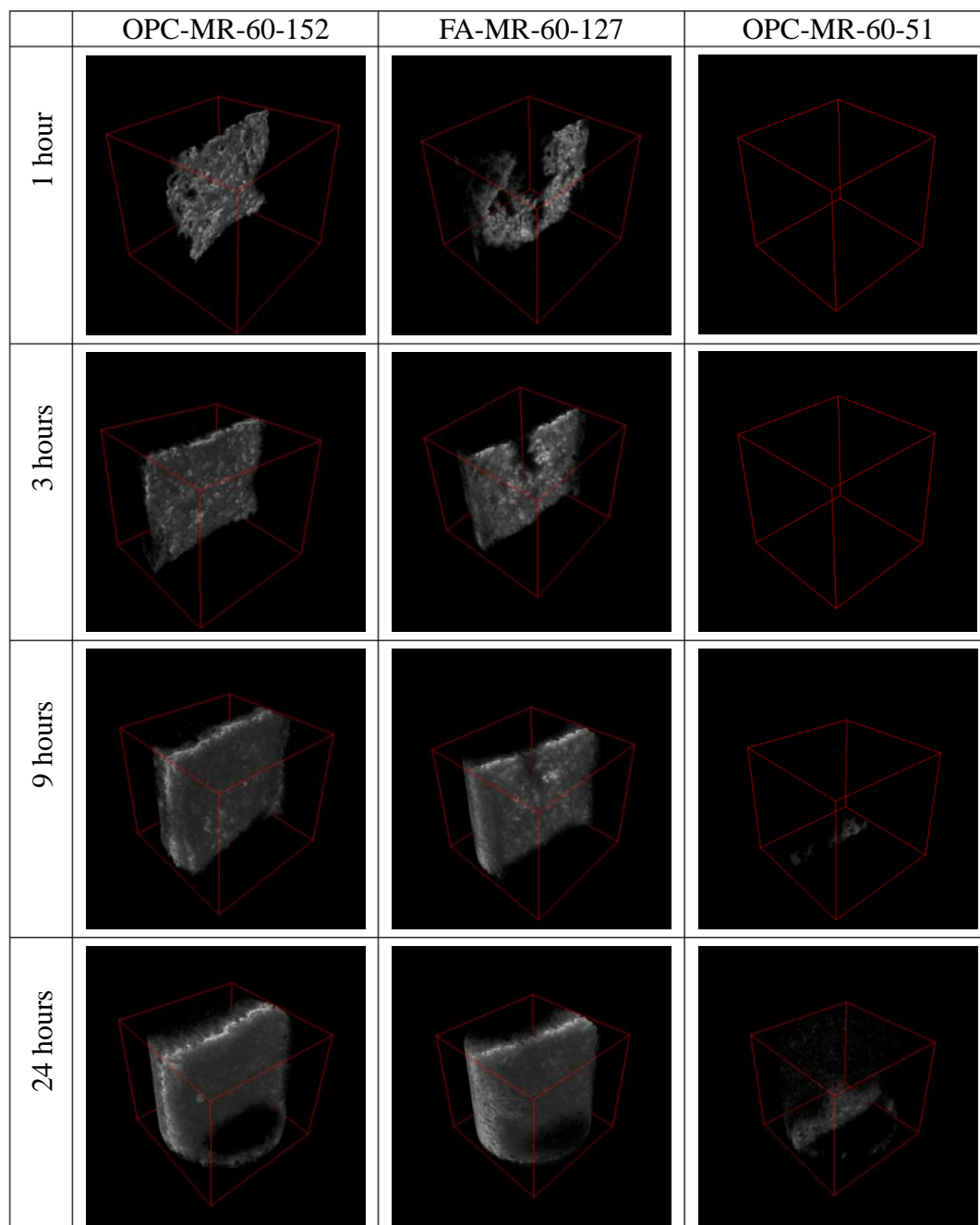

Figure 6.8 Three-dimensional images of cesium tracer by specimen and exposure time (2 mm to 18 mm from surface exposed to the solution).

an obstacle in the water uptake process as well as the diffusion of tracer. The same phenomenon in which tracer diffuses in water-filled cracks occur in all specimens. In the next exposure time, the results showed that there was no addition of crack space filled by tracer. In this way, the diffusion of tracer only followed the path that formed on the short period of exposure time. This finding implies that for concrete structure in salt-laden environments, the diffusive transport substances such as chloride and magnesium ions in sea water is controlled by the initial condition with regard to the water saturation level inside the crack space.

Figure 6.8 shows the comparison of the rate of diffusive tracer in the specimens according to the exposure time in 3D. However, it should be noted that such 3D image of diffusive cesium tracer in the crack can only be obtained if the position and size of the cross section of the specimen in reconstructed slices are the same in both initial condition and solution-exposed condition. Such condition in the experiment was achieved as there was no change in the position of the specimen on the rotating stage at both initial condition and solution-exposed condition. As shown in Figure 6.8, the diffusive tracers move quickly deep in the crack and gradually expand to the lateral direction through the wall of the cracks. This is especially true for OPC-MR-60-152 and FA-MR-60-127. Meanwhile, no or less diffusive tracer in OPC-MR-60-51 was observed for the exposure times of 1 and 3 hours. As compared to the case with OPC-MR-60-152 and FA-MR-60-127, the diffusive transport in the crack was reduced due to small crack opening width for OPC-MR-60-51.

Furthermore, as shown in Figure 6.8, it is clear that OPC-MR-60-152 has more diffusion path compared with other specimens characterized by the large volume of cracks filled by tracer. The higher amount of diffusion path formed on the OPC-MR-60-152 specimen is appeared to cause by higher amount of water filled the crack. This resulted from faster displacement process between the air and water in the crack. In contrast, pre-soaking for the OPC-MR-60-51 specimen for 24 hours produced the least diffusion path of tracer. Given the same process of pre-soaking, the diffusion path in the crack is significantly influenced by crack opening width. Such finding indicates the effect of crack opening width on the diffusive transport in cracked concrete.

6.2.1. Diffusion coefficient along the crack

Figures 6.9(a) to (f) show the concentration profiles and rate of tracer transport of all specimens. In Figures 6.9(a), (c) and (e), the tracer concentration profiles were obtained. The cesium concentration profiles shown in the Figure 6.9 were actually obtained from the analysis of microtomographic images on the basis of CT number. Furthermore, these CT numbers were converted into cesium tracer concentration by using the curve of CT number and cesium tracer relationship as shown in Figure 3.20.

As shown in Figure 6.9, it is obvious that the concentration decreased along the crack depth while increased with exposure times. In addition, from Figures 6.9(b) and (d), it can be seen that the rate of tracer was rapid in the first one hour for both OPC-MR-60-152 and FA-MR-60-127. Afterwards, there is a decrease in the rate of tracer drastically and it tends to be constant for the succeeding exposure time. For OPC-MR-60-51 specimen, it was found that there was no significant change in CT numbers between initial conditions and the solution-exposed conditions up to 3 hours exposure time (Figure. 6.9(f)). During those exposure times that the rate of tracer in OPC-MR-60-51 was very slow and difficult to observe. This finding is supported by the results of subtraction images where there is no imprint of tracer left in the crack as shown in Figure 6.8.

In addition, as shown in Figure 6.9, it can be seen that cesium tracer concentration of OPC-MR-60-152 was higher than that of FA-MR-60-127 specimen at the same height from surface exposed to the solution. In this regard, cesium tracer content in the cracked zone was found to be depending on the crack width, which governs the supply of the solute to the crack.
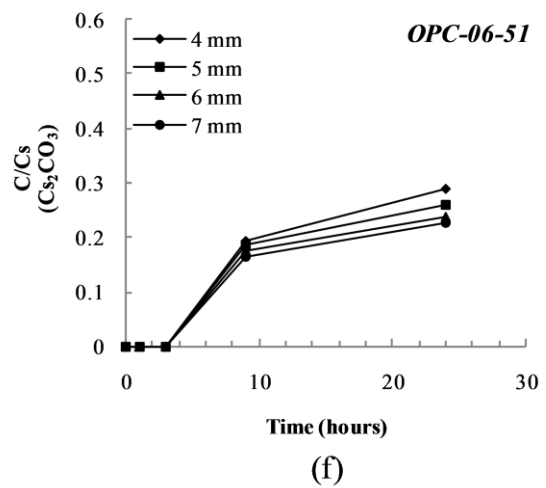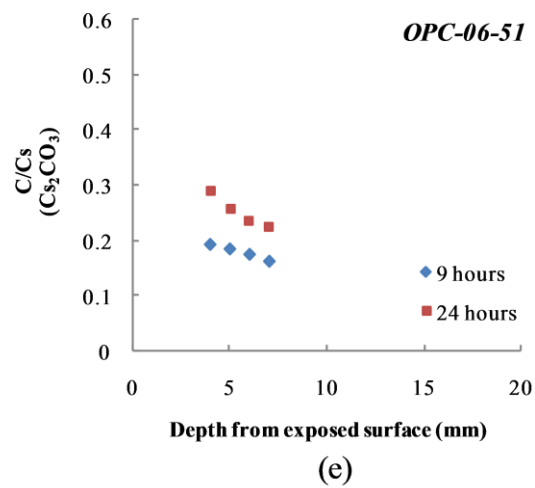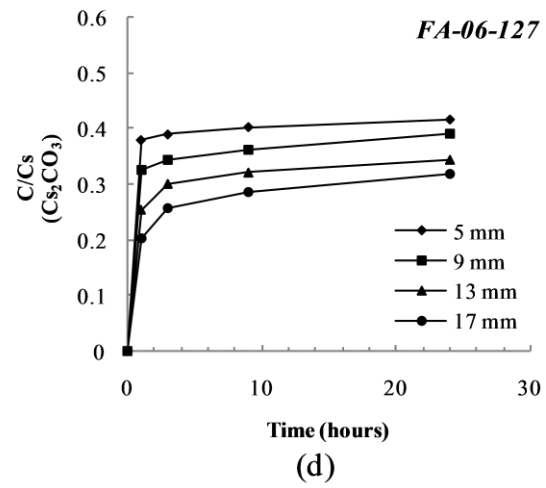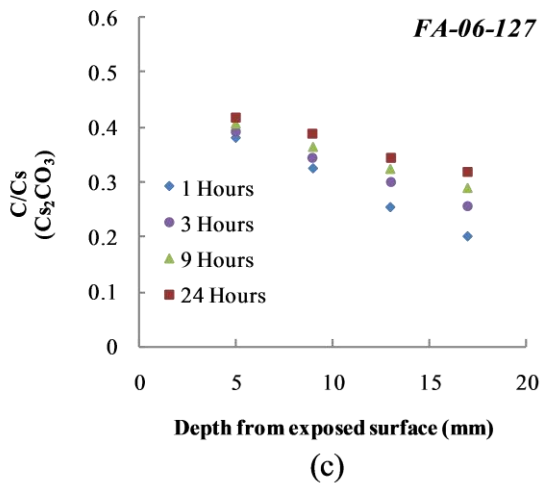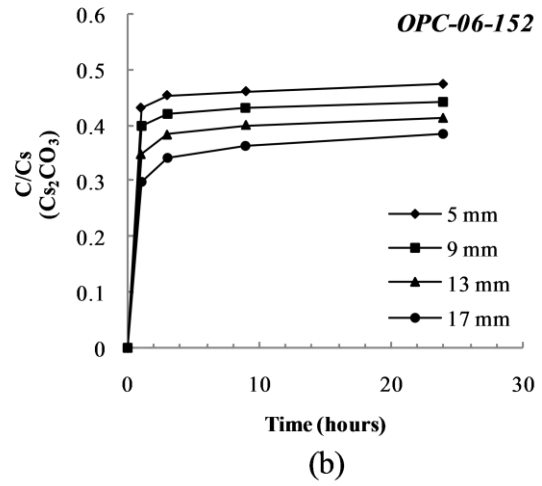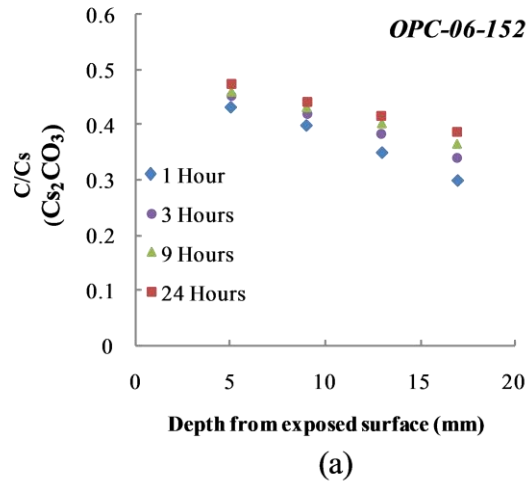
Figure 6.9 Concentration profiles and rate of tracer transport of OPC-06-152 (a) (b), FA-06-127 (c) (d), and OPC-06-51 (e) (f).

Tabel 6.2 Diffusion coefficients along the crack for partially saturated cracked specimens

Specimen	Diffusion Coefficient (m^2/s)			
	initial to 1 hr	1 hrs to 3 hrs	3 hrs to 9 hrs	9 hrs to 24 hrs
OPC-MR-60-51	-*	-*	-*	7.5×10^{-11}
OPC-MR-60-152	4.4×10^{-8}	8.2×10^{-10}	2.5×10^{-10}	9.5×10^{-11}
FA-MR-60-127	3.0×10^{-8}	8.0×10^{-10}	2.4×10^{-10}	9.3×10^{-11}

*Not calculated because there is no change in CT number up to 9 (nine) hours exposure time

The diffusion coefficients along the crack for all specimens are shown in Table 6.2. The diffusion coefficients were calculated using the concentration profile after the first one hour exposure period and then compared with those calculated for later exposure periods in both OPC-MR-60-152 and FA-MR-60-127. As given in Table 6.2, the diffusion coefficients are greater than the diffusion coefficient of cesium in free water (2.06×10^{-9} m^2/s [119,120]) in the first one hour. This result implies that in the partially saturated cracked cementitious materials during short period of exposure time, the mobility of tracer along the crack may involve transport mechanism other than molecular diffusion. However, for the succeeding exposure time the diffusion coefficient decreased drastically up to the level where the diffusion coefficient is lower than the diffusion in the free water. This suggests that at this stage, the mobility of tracer along the crack is restricted but controlled by diffusion.

The crack opening width of FA-MR-60-127, that is slightly smaller, could be considered roughly equivalent to that of OPC-MR-60-152 whereas the constrictivity of FA-MR-60-127 was larger than that of OPC-MR-60-152 as shown in Table 4.3. We suggest that in the region of diffusion the constrictivity factor influence the mobility of ions in the crack. This larger constrictivity could compensate the effect of smaller crack opening width on the diffusion process along the crack for FA-MR-60-127.

Meanwhile, for the specimen OPC-MR-60-51, the average diffusion coefficient that were calculated from 9 and 24 hours exposure times was smaller when compared to that of OPC-MR-60-152 with the larger crack opening width. Since the presence of water in the crack space provide the preferential path for tracer to diffuse, a growing number of crack filled with water would lead to many paths that can be traversed by tracer resulting to easier diffusion for tracers in larger crack space.

In addition, it can be seen that under similar both crack opening width and exposure time, the diffusion coefficient along the crack of cracked specimen in oven-dried condition was rougly similar to the average diffusion coefficient of partially saturated condition. However, in over-dried cracked specimen the capillary suction can be more dominant transport mechanism.
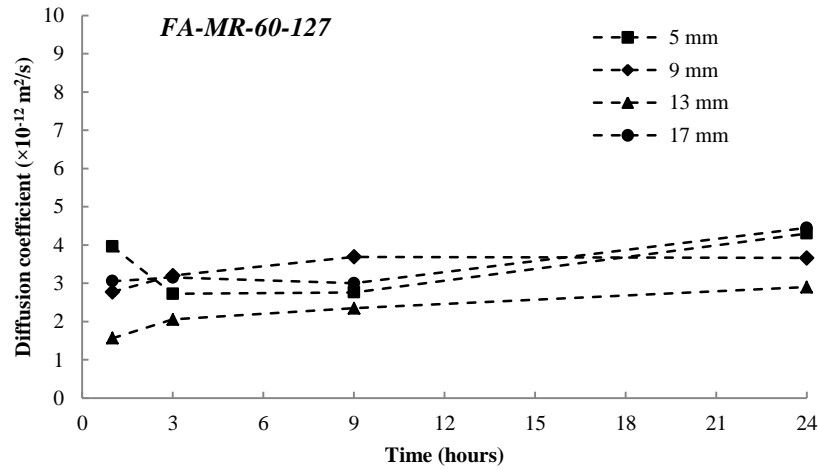
6.2.2. Diffusion coefficient perpendicular to the crack wall (through the uncracked matrix)

Figure 6.10 shows the variation of apparent diffusion coefficient of cesium perpendicular to the crack wall according to the distance from the surface exposed to the solution. Although the diffusion coefficients are neither uniform in depth nor constant with time, FA-MR-60-127 generally exhibits lower diffusion coefficients. Porosity and pore connectivity are among the important factors to control the diffusive transport. In addition the presence of aggregate and air void play an important role in the uncracked matrix.
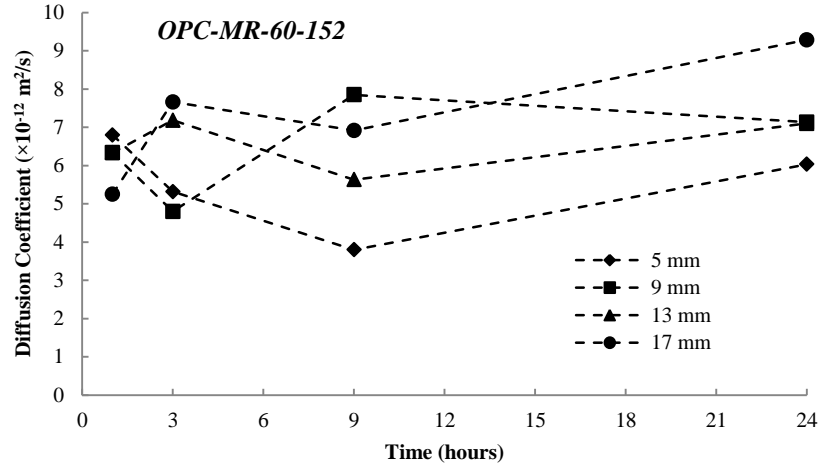
(a)

(b)

Figure 6.10 Variation in the apparent diffusion coefficients perpendicular to the crack wall (a) OPC-MR-60-152 specimen, (b) FA-MR-60-127 specimen.

The average value of the apparent diffusion coefficient variation of the uncracked matrix for OPC-MR-60-152, FA-MR-60-127 and OPC-MR-60-51 are 6.46×10^{-12}, 2.88×10^{-12}, 5.18×10^{-13} m^2/s, respectively. The apparent diffusion coefficients of cesium ion obtained in this study are considered reasonable and lay within reported ranges by previous research [71,72].

For the specimen of OPC-06, the diffusion coefficient was increased with the increasing crack width opening. As described previously, the specimen with larger crack width opening has a higher diffusion rate and hence higher concentration of solute occurred in the crack. Furthermore, higher concentration of solute in the crack increased the penetration of solute towards the uncracked matrix. However, this mechanism is also affected by the level of diffusivity resistance of the uncracked matrix. These results suggest that solute content in the crack space actually governs the supply of the diffusive cesium at the surface area perpendicular to the diffusion in the uncracked body.

Similar to the results obtained from previous study, the addition of fly ash with longer curing period led to a reduction of the diffusion coefficient in its uncracked body as compared

with that of OPC specimen, although those diffusion coefficients along the crack were almost the same as given in Table 6.2. Fly ash concrete can normally exhibit increased resistance to diffusivity due to its dense microstructure caused by pozzolanic reaction. Kumar et al [71] found the reduction of the effective diffusion coefficients of cesium ion in cement pastes blended with blast-furnace slag and silica fume. Likewise, it can be said that this observed effect of reduced cesium diffusion can be explained by the fly ash addition to the specimen.

In addition, this study points out that the diffusion coefficient in the crack is 100 times higher than that of the uncracked matrix. On the other hand, the JSCE Standard Specification for Concrete Structures specifically mentions that the diffusion coefficient of chloride ion in cracked concrete with crack opening width larger than 100 μm is 1000 times than that of in the uncracked matrix. The result obtained from this study is slightly lower than that of the JSCE. However, it must be underlined that the JSCE takes into consideration the diffusion coefficient in whole cracked concrete instead of the diffusion coefficient in the crack. In this way conventional experimental testing method used to evaluate the diffusivity in the cracked concrete could not separate the diffusivity in the crack and uncracked matrix in the cracked concrete.

6.2.3. Modeling diffusive transport along the crack

In order to assess a quantitative relationship between crack geometry and its diffusivity, diffusion coefficient of crack analogous to that of porous medium is defined as follows:

$$D_{cr} = \frac{\delta}{\tau^2} D_0 \qquad (6.1)$$

where δ and τ are tortuosity and constrictivity of the crack path, and D_{cr} and D_0 are the diffusion coefficients at the crack and free solution (m²/s), respectively. However, indication from the result suggests that there is another factor controlling the diffusion in the crack which we referred to as *diffusion-accessible path, ξ. Diffusion-accessible path* factor arises since not all cracks can be traversed by solute during diffusion process due to partially saturated of crack space. So, Eq. (6.1) may be modified as

$$D_{cr} = \frac{\delta}{\tau^2} D_0 \, \xi \qquad (6.2)$$

In this study, the diffusion coefficients used to determined diffusion-accessible path factor were the average diffusion coefficient values from 1 hour to 24 hours exposure period. It is based on an assumption that in those periods, the mobility of tracer along the crack was controlled by diffusion. The diffusion-accessible path factors, ξ, obtained from this study for OPC-MR-60-152, FA-MR-60-127, and OPC-MR-60-51 were 0.50, 0.40 and 0.11, respectively. These values show the percentage of crack space that can be traversed by solute during diffusion process. They are controlled indirectly by saturation degree of crack due to the natural immersion process without any external factors. Higher diffusion-accessible path factor would result from larger crack opening width and would imply less air-filled cavity in the crack and for fully saturated crack condition the diffusion-accessible path factor is 1. Considering the diffusion-accessible path factor is strongly related to the saturation degree of crack, then the values of diffusion-accessible path factor obtained in this study is reasonable and appropriate with the visual observation results. For the example, OPC-MR-60-152 which has the highest saturation degree indicated by large volume of cracks filled by tracer has the highest diffusion-accessible path factor. In addition, the quantitative evaluation of diffusion accessible-path factor for the other cases need to be carried out based on a careful design of

experiment using predetermined the crack opening width and immersion condition.

6.3. SUMMARY

Cesium tracer diffusion tests were conducted in the different type of cracked mortar specimens and the diffusivity was evaluated by using micro-focus X-ray CT on the basis of the change of the CT number. The crack in the beam specimen with size of 10 x 20 x 60 mm was induced by flexural test and the crack in the cylinder specimens with size of 20 mm in diameter and 40 mm in height was induced by splitting tensile test. As for flexural crack specimens, the specimens were oven dried before cesium tracer diffusion test. Meanwhile, for splitting tensile crack specimens, the specimens were immersed in the water for 24 hours before cesium tracer diffusion test and the observation was made in-situ inside X-ray CT machine.

The diffusion coefficient of cesium tracer along the crack in the oven-dried flexural crack specimen with crack opening width less than 50 µm was almost reached the diffusion coefficient of cesium in the free water. Considering the initial condition of flexural crack specimens was oven-dried, thus, that mobility of cesium tracer along the crack may involve more than one transport mechanisms but not only diffusion. The apparent diffusion coefficient of cesium tracer in the uncracked matrix of FA specimen was smaller than that of OPC specimen. The drying process before diffusion test may enhance the pozzolanic reaction resulting in the increased resistance to diffusivity.

The observation of cross sectional image of splitting tensile crack specimen in the cesium expose condition shows that the tracer only fills the crack occupied by water. Thus, the immersion process for 24 hours before cesium tracer diffusion test did not produce fully saturated crack, and leaving behind air pockets. In the next exposure time, the results showed that there was no addition of crack space filled by tracer. In this way, the diffusion of tracer only followed the path that formed on the short period of exposure time.

The diffusion coefficients along the crack for partially saturated OPC and FA specimens with roughly equivalent crack opening width are greater than the diffusion coefficient of cesium in free water in the first one hour. However, for the succeeding exposure time the diffusion coefficient decreased drastically up to the level where the diffusion coefficient is lower than the diffusion in the free water. Although the diffusion coefficients along the crack were almost the same for OPC and FA, the diffusion coefficient in the uncracked matrix of FA specimen was smaller than that of OPC specimen. The addition of fly ash followed by longer curing period can normally exhibit increased resistance to diffusivity due to its dense microstructure caused by pozzolanic reaction.

CHAPTER 7
CONCLUSION

1. Low alkali cement paste specimen with a composition of 40% OPC, 20% silica fume and 40% fly ash and water to binder ratio of 0.5 was observed by using synchrotron X-ray CT with resolution of 0.5 μm/voxel at SPring-8, Japan. The evolution of the microstructure with increased curing periods and its alteration due to leaching were investigated. As a comparison, normal cement paste specimen was also observed in similar manner. The following conclusions can be drawn:

    1.1. During curing period, the porosity of low alkali cement paste specimen is slightly larger than that of normal cement paste specimen at the same curing periods. In this regard, larger porosity creates less tortuous of pore structure in the low alkali cement paste specimen as compared with that of normal cement paste specimen.

    1.2. The rate in the reduction of volume of pore with larger size in normal cement paste specimen was higher than that of low alkali cement paste specimen up to 28 days. However, from 28 days to 146 days, low alkali cement paste specimen shows more significant in the reduction of volume of pore with larger size as compared with that of normal cement paste specimen.

    1.3. After leaching test, the porosity of normal cement paste specimen increased significantly as compared with that of low alkali cement paste specimen. The total porosity in normal cement paste specimen increased from 12% to 33%, meanwhile, low alkali cement paste specimen increased from 16% to 20%.

    1.4. In addition, the transport process through percolated porosity is considered to be far more facile in normal cement paste specimen after leaching test as compared with that of low alkali cement paste specimen which indicated by diffusion tortuosity obtained from random walk simulation.

2. Micro-focus X-ray CT was employed to observe cracked mortar specimens due to mechanical loading. The cracks in beam specimens of the size of 10 x 20 x 60 mm and cylinder specimens of the size of 20 mm in diameter and 40 mm in height were induced by flexural test and splitting tensile test, respectively. Subsequently, the 3D crack geometry was obtained from microtomographic images. The following conclusions can be drawn:

    2.1 The tortuosity of splitting tensile crack in the mortar specimen with the maximum aggregate size of 1.7 mm and compressive strength ranged from 21 to 29 MPa was found to be around 1.25 to 1.26. Meanwhile, it ranged from 1.13 to 1.14 for the flexural crack in the mortar specimen with maximum aggregate size of 1.7 mm and compressive strength ranged from 31 to 46 MPa.

    2.2 The presence of voids and type of cracks plays an important role on the constrictivity of the crack. The addition of fly ash could reduce the effect of constrictivity in the crack as presence of fly ash decrease the number of voids in the mortar.

3. The transport mechanism in cracked mortar specimen was clarified by employing micro-focus X-ray CT coupled with in-situ tracer diffusion test. The following conclusions can be drawn:

    3.1 Diffusivity in the crack was controlled by following factors: the crack opening width, as well as, by its constrictivity. The diffusive transport was also restricted due to the presence of air pockets in the crack. In this regard, a diffusion-accessible path factor was proposed to account for the degree of water saturation within the crack space.

3.2 The rate of solute in the crack space was rapid in the first one hour for partially saturated specimen with equivalent crack opening. The diffusion in the early period in partially saturated specimen exposed to the solution strongly influenced the rate of solute transport for the succeeding exposure time.

3.3 The diffusivity in the cracked mortar was evaluated in both along the crack and perpendicular to the crack wall (through the uncracked matrix). It is found that the diffusivity along the crack ranges from 10^{-8} to 10^{-10} m^2/s as compared with 10^{-12} m^2/s for the uncracked matrix.

3.4 It was confirmed that the addition of fly ash could reduce the diffusivity through the uncracked matrix as compared with normal OPC mortar of equivalent diffusion coefficient along the crack.

4. In the study of deteriorated cementitious materials due to mechanical loading, synchrotron X-ray CT was combined with micro-tensile instrument and the observation during the application of load was conducted in-situ inside synchrotron X-ray CT chamber. Although there was no definite result of this experiment, however, this experiment shows us that the application of synchrotron X-ray CT can be combined with other mechanical test. Furthermore, by improving the quality both sample preparation and loading instrument, the behavior of microstructure under external load could be observed.

5. Using micro-focus X-ray CT, the change of pore structure in high strength concrete due to high temperature exposure followed by different re-curing method namely water re-curing and air re-curing was examined. The following conclusions can be drawn:

5.1 It was observed that cracks occurred in the concrete specimen due to high temperature exposure can be categorized into three types of cracks, namely interfacial cracks between mortar and coarse aggregates, bridging cracks between aggregates and bridging cracks between aggregates and air voids.

5.2 Water re-curing is more effective in the recovery of microstructure of concrete after high temperature exposure. The total pore volume reduced from 9.4% to 5.6 % after 28 days of re-curing. On the other hand, air re-curing did not lead to significant recovery of the microstructure. Only a small decrease in the total pore volume was observed over the 28-day re-curing period.

6. In this research the versatility of the application of X-ray CT has been presented while several new findings were also provided. It is highly expected that by using X-ray CT, the microstructure in cementitious materials will be more explored in the near future. X-ray CT technique can also be combined with other testing methods. Using X-ray CT technique coupled with in-situ tracer diffusion test would allow further understanding of the transport mechanism of diffusion in cracked cementitious materials.

REFERENCES

[1]   G.N. Hounsfield. Computerized transverse axial scanning (tomography): Part I. Description of system. *British Journal of Radiology*, 46, 1016-1022, 1973.

[2]   G. Wang, H. Yu and B. De Man. An outlook on X-ray CT research and development. *Medical Physics*, 35(3), 1051-1064, 2007.

[3]   I.L. Morgan, H. Ellinger, R. Klinksiek and J.N. Thompson. Examination of concrete by computerized tomography. *Journal of the American Concrete Institute*, 77(1), 23-27, 1980.

[4]   D.P. Bentz, D.A. Quenard, H.M. Kunzel, J. Baruchel, F. Peyrin, N.S. Martys and E.J. Garboczi. Microstrcuture and transport properties of porous building material. II: Three-dimensional X-ray tomographic studies. *Materials and Structures*, 33, 147-153, 2000.

[5]   E. Galluci, K. Scrivener, A. Groso, M. Stampanoni and G. Margaritondo. 3D experimental investigation of the microstructure of cement paste using synchrotron X-ray microtomography. *Cement and Concrete Research*, 37, 360-368, 2007.

[6]   L. Helfen, F. Dehn, P. Mikulik and T Baumbach. Three-dimensional imaging of cement microstructure evolution during hydration. *Advances in Cement Research*, 17(3), 103-111, 2005.

[7]   T. Hitomi, Y. Mita, H. Saito and N. Takeda. Observation of fine structure of mortar using X-ray CT images at SPring-8. *Proceeding of the Japan Concrete Institute*, 26(1), 645-650, 2004. (in Japanese)

[8]   M. Koster, J. Hannawald and W. Brameshuber. Simulation of water permeability and water vapor diffusion through hardened cement paste. *Computational Mechanics*, 37(2), 163-172, 2006.

[9]   S. Lu, E.N. Landis and D.T. Keane. X-ray microtomographic studies of pore structure and permeability in Portland cement concrete. *Materials and Structures*, 36, 11-20, 2006.

[10]   M.A.B. Promentilla, T. Sugiyama, T. Hitomi and N. Takeda. Characterizing the 3D pore structure of hardened cement paste with synchrotron microtomography. *Journal of Advanced Concrete Technology*, 6(2), 273-286, 2008.

[11]   M.A.B. Promentilla, T. Sugiyama, T. Hitomi and N. Takeda. Quantification of tortuosity in hardened cement paste using synchrotron-based X-ray computed microtomography. *Cement and Concrete Research*, 39, 548-557, 2009.

[12]   N. Burlion, D. Bernard and D. Chen. X-ray microtomography: Application to microstructure analysis of cementitious material during leaching process. *Cement and Concrete Research*, 36, 346-357, 2006.

[13]   T. Sugiyama, M.A.B. Promentilla T. Hitomi and N. Takeda. Application of synchrotron microtomography for pore structure characterization of deteriorated cementitious materials due to leaching. *Cement and Concrete Research*, 40, 1265-1270, 2010.

[14]   N.N. Naik, A.C. Jupe, S.R. Stock, A.P. Wilkinson, P.L. Lee and K.E. Kurtis. Sulfate attack monitored by microCT and EDXRD: Influence of cement type, water-to cement ratio, and aggregate. *Cement and Concrete Research*, 36, 144-159, 2006.

[15]   H. Elaqra, N. Godin, G. Peix, M.R. Mili and G. Fantozzi. Damage evolution analysis in mortar during compressive loading using acoustic emission and X-ray tomography: Effect of the sand/cement ratio. *Cement and Concrete Research*, 37(5), 703-713, 2007.

[16]   M.A.B. Promentilla and T. Sugiyama. X-ray microtomography of mortars exposed to

freezing-thawing action. *Journal of Advanced Concrete Technology*, 8(2), 97-111, 2010.

[17] T. Kikkawa, T. Sugiyama, I.S. Darma and K. Shimura. Observation of flexural cracking and cesium carbonate transport using X-ray CT. Proceeding of Annual Conference of Japan Concrete Institute, 34(1), 1810-1815, 2012. (in Japanese)

[18] H.F.W. Taylor. *Cement Chemistry*. London: Tomas Telford Publishing, 1997.

[19] R.B Williamson. Solidification of Portland cement. *Progress in Material Science*, 15(3), 189-286, 1972.

[20] S. Diamond. Cement paste microstructure-an overview at several levels. *Proceeding of Conference on Hydraulic Cement Pastes: Their Structure and Properties, Cement and Concrete Association*, 2, 1976.

[21] B.J. Dalgleish and P.L. Pratt. Fractographic studies of microstructural development in hydrated Portland cement. *Journal of Materials Science*, 17, 2199-2207, 1982.

[22] K.L. Scrivener and P.L. Pratt. Backscattered electron images of polished cement section in the scanning electron microscope. *Proceeding of the International Conference on Cement Microscopy*, 145-155, 1984.

[23] E.K. Attiogbe and D. Darwin. Submicrocracking in cement paste and mortar. *ACI Materials Journal*, 84(6), 491-500. 1987.

[24] K.L. Scrivener and E.M. Gartner. *Materials Research Society Symposium Proceeding*, 114, 77, 1988.

[25] K.L. Scrivener and P.L. Pratt. The characterization and quantification of cement and concrete microstructure. *Proceeding of 1ˢᵗ International Congress RILEM/AFREM*, 61-68, 1987.

[26] K.O. Kjellsen, J. Rachel, Detwiler, and O.E. Gjørv. Backscatered electron imaging of cement pastes hydrated at different temperatures. *Cement and Concrete Research*, 20, 308-311, 1990.

[27] T. Matsusima, J. Katagiri, K. Uesugi, T. Nakano and A. Tsuchiyama. Micro X-ray CT at SPring-8 for granular mechanics. *Proceeding of Geotechnical Symposium, Soil Stress-Strain Behaviour: Measurement, Modeling and Analysis*, 225-234, 2006.

[28] T. Sugiyama, W. Ritthichauy and Y. Tsuji. Simultaneous transport of chloride and calcium ions in hydrated cement system. *Journal of Advanced Concrete Technology*, 1(2), 127-138, 2003.

[29] T. Sugiyama, W. Ritthichauy and Y. Tsuji. Experimental investigation and numerical modeling of chloride penetration and calcium dissolution in saturated concrete. *Cement and Concrete Research*, 38, 49-67, 2008.

[30] K.L Scrivener. The use of backscattered electron microscopy and image analysis to study the porosity of cement paste. *Proceeding of Materials Research Society Symposium*, 137, 129-140, 1989.

[31] C.A. Léony Léon. New perspectives in mercury porosimetry. *Advanced Colloid Interface Science*, 76-77, 341-372, 1998.

[32] S. Diamond. Mercury porosimetry: an inappropriate method for measurement of pore size distribution in cement-based materials. *Cement and Concrete Research*, 30, 1517-1525, 2000.

[33] G. Helbet. Mercury porosimetry: a general (practical) overview. *Particle & Particle Systems Characterization*, 23, 9-19, 2006.

[34] Q. Zeng, K. Li, T. Fen-chong and P. Dangla. Pore structure characterization of cement paste blended with high volume fly ash. *Cement and Concrete Research*, 42, 194-204, 2012.

[35] R.A Cook and K.C. Hover. Mercury porosimetry of hardened cement paste. *Cement and Concrete Research*, 29, 933-943, 1999.

[36]   S. Diamond and D. Bonen. Microstructure of hardened cement paste – A new interpolation. *Journal of the American Ceramic Society*. 76(12), 2993-2999, 1993.

[37]   E.P. Barrett, L.G. Joyner and P.P. Halenda. The determination of pore volume and area distributions in porous substances. I. Computations from nitrogen isotherms. *Journal of the American Ceramic Society*, 73, 373-380, 1951.

[38]   T.C. Powers and T.L. Brownyard, Studies of the physical properties of hardened Portland cement paste, *ACI J. Proc*. 43, 845–880, 1947.

[39]   M.C.G. Juenger and H.M. Jennings, The use of nitrogen adsorption to assess the microstructure of cement paste. *Cement and Concrete Research*, 31, 883–892, 2001.

[40]   R.S. Mikhail, E. Copeland, S. Brunauer, Pore structure and surface areas of hardened Portland cement pastes by nitrogen adsorption. *Canadian Journal of Chemistry*, 42, 426–438, 1964.

[41]   S. Lu, E.N. Landis and D.T Keane. X-ray microtomographic studies of pore structure and permeability in Portland cement concrete. *Materials and Structures*, 36, 11-20, 2006.

[42]   R.W Burrows. The visible and invisible cracking of concrete. A*CI Monograph No.11. American Concrete Institute*, 1998.

[43]   Z.P. Bazant and J. Planas. Fracture and size effect in concrete and other quasibritle materials. *CRC press*, 1998.

[44]   Z. Chunseng, L. Kafei and P. Xiaoyun. Geometry of crack network and its impact on transport properties of concrete. *Cement and Concrete Research*, 42, 1261-1272, 2012.

[45]   H.W. Reinhardt (Ed). Penetration and permeability of concrete: Barriers to organic and contaminating liquids. *RILEM Report*, 16, 1997.

[46]   K. Wang, D.C. Jansen and S.P Shah. Permeability study of cracked concrete. *Cement and Concrete Research*, 27(3), 381-393, 1997.

[47]   E. Kato, Y. Kato and T. Uomoto. Development of simulation model of chloride ion transportation in crack concrete. *Journal of Advanced Concrete Technology*, 3(1), 85-94, 2005.

[48]   L. Wang, M. Soda and T. Ueda. Simulation of chloride diffusivity for cracked concrete based on RSBM and truss network model. *Journal of Advanced Concrete Technology*, 6(1), 143-155, 2008.

[49]   L. Wang and T. Ueda. Mesoscopic simulation of chloride ion diffusion in frost-damaged concrete. *International Journal of Modeling, Identification and Control*, 7(2), 148-154, 2009.

[50]   L. Wang and T. Ueda. Mesoscale Medoling of chloride diffusion in cracks and cracked concrete. *Journal of Advanced Concrete Technology*, 9(3), 241-249, 2008.

[51]   K.M. Nemati. Fracture analysis of concrete using scanning electron microscopy. *Scanning*, 19, 426-430, 1970.

[52]   H. Le Chatelier and J.L. Mack. Experimental researches on the constitution of hydraulic mortars. *McGraw Publishing Company*, New York, 1905.

[53]   B. Tavasci. Structure of hydrated Portland cement. *Zement*, 30, 43-48, 1941.

[54]   A. Akhavan, S.M.H. Shafaatin and F. Rajabipour. Quantification the effect of crack width, tortuosity, and roughness on water permeability of cracked mortars. *Cement and Concrete Research*, 42, 313-320, 2012.

[55]   D. Darwin, K.W Ketcham, F.A. Romero and S. Gong. Experimental techniques to study the microstructure of cement-based materials," *Proceedings of ASCE Engineering Mechanics Specialty Conference*, 2, 1082-1086, 1991.

[56]   D. Darwin, K.W Ketcham, F.A. Romero and J.L. Martin. Automated Identification of Compression-Induced Cracking in Cement Paste, *Proceedings of ASCE Engineering*

Mechanics Conference, 494-497, 1992.

[57] A. Ammouche, J. Riss, D. Breysse and J. Marchand. Image analysis for the automated study of microcracks in concrete, *Cement and Concrete Composite*, 23, 267-278, 2001.

[58] M. Elzafraney and Soroushian. Assessment of microcracks development in concrete materials of different strength. *Materials and Structures*, 274, 724-731, 2004.

[59] M.A Glanicki and A. Litorowicz. Crack system evaluation in concrete elements at mesoscale. *Bulletin of Polish Academy of Science*, 54(4), 371-379, 2006.

[60] D. Fukuda, Y. Nara, Y. Kobayashi, M. Maruyama, M. Koketsu, D. Hayashi, H. Ogawa and K. Kaneko. Investigation of self-healing in high-strength and ultra-low permeability concrete in water using micro-focus X-ray CT. *Cement and Concrete Research*, 42, 1494-1500, 2012.

[61] C.M. Aldea, S.P. Shah and A. Karr. Effect of cracking on water and chloride permeability of concrete. *Journal of Materials and Civil Engineering*, 181-197, 1999.

[62] D. Witting. Rapid measurement of chloride permeability of concrete. *Public Roads*, 45(3), 101-112, 1981.

[63] A. Djerbi, S. Bonnet, A. Khelidj and V. Baroghel-bouny. Influence of traversing crack on chloride diffusion into concrete. *Cement and Concrete Research*, 38, 877-883, 2008.

[64] C. Andrade. Calculation of chloride diffusion coefficient in concrete from ionique diffusion measurements. *Cement and Concrete Research*, 23(3), 724-742, 1993.

[65] O. Truc. A new way for determining the chloride diffusion coefficient in concrete from steady state diffusion test. *Cement and Concrete Research*, 30, 217-226, 2000.

[66] M. Ismail, A. Toumi , R. Francois and R. Gagne. Effect of crack opening on the local diffusion of chloride in cracked mortar samples. *Cement and Concrete Research*, 38, 1106-1111, 2008.

[67] A. Polak, A. Grader, R. Wallach, and R. Nativ, R. Chemical diffusion between a fracture and the surrounding matrix: measurement by computed tomography and modeling. *Water Resource Research*, 39(4), 1106, 2003.

[68] T. Al, H.M.D. Agbogun, and E.M.A. Hussein. Three dimensional imaging of porosity and tracer concentration distribution in a dolostone sample during diffusion experiments using X-ray micro-CT. *Journal of Contaminant Hydrology*, 145(1), 44-53, 2013.

[69] L. Cavé, T. Al, Y. Xiang, and D. Loomer. Investigation of diffusive transport process in sedimentary rock. *Report of Nuclear Waste Management Organization*, NWMO TR-2010-04, 2010.

[70] S. Ikeda, T. Sugiyama, T. Kikkawa, and K. Shimura. Study on transport phenomenon in crack using the cesium carbonate as a tracer by X-ray CT. *Proceedings of the Concrete Structure Scenarios of JSMS*, 12, 207-212, 2012. (in Japanese).

[71] A. Kumar, and D.M Roy. Retardation of Cs^+ and Cl^- diffusion using blended cement admixtures. *Journal of American Ceramic Society*, 69(4), 356-360, 1986.

[72] C. Bucur, M. Olteanu, C. Cristache, and M. Pavelescu. Radionuclide transport through cement matrices. *Revista De Chimie*, 61 (5), 458-461, 2010.

[73] L.W. Goldman. Principle of CT and CT Technology. Journal of Nuclear Medicine Technology, 35, 115-128, 2007.

[74] J. Bursch, R. Josh, and P.H. Heintz. *Roentgen-, Cine-, and Videodensitometry*, 81-84, 1971.

[75] R.A. Robb. X-ray computed tomography. *Ann. Rev. Biophys. Bioeng*, 11, 177-201, 1982.

[76] S.W. Smith. The scientist and engineer's guide to digital signal processing, *California*

Technical Publishing, Chapter 25, 1997.

[77] P.P. Bruyant. Analitic and iterative reconstruction algorithms in SPECT. *The Journal of Nuclear Medicine*, 43(10), 1343-1358, 2002.

[78] K. Uesugi, Y. Suzuki, N. Yagi and A. Tsuchiyama. Development of high spatial resolution X-ray CT system at BL47XU in SPring-8. *Nuclear Instruments and Methods I Physisc Research*, A 467-468, 853-856, 2001.

[79] H. Saito, S. Nakane, S. Ikari and A. Fujiwara. Preliminary experimental study on the deterioration of cementitious materials by an acceleration method. *Nuclear Engineering and Design*, 138, 151-155, 1992.

[80] H. Saito and S. Nakane. Comparison between diffusion test and electrochemical acceleration test for leaching degradation of cement hydration products, ACI Material Journal, 96, 208, 212, 1999.

[81] C.S. Poon, S. Azhar, M. Anson and Y.K. Wong. Strength and durability recovery of fire-damaged concrete after post-fire curing. *Cement and Concrete Research*, 31(9), 1307-1318, 2001.

[82] H. Uchikawa. Similarities and discrepancies of hardened cement paste, mortar, and concrete from the standpoint of composition and structure. *Journal of Research of the Onoda Cement Co*, 40(2), 119, 87-121, 1988.

[83] H. Uchikawa. Similarities and discrepancies of hardened cement paste, mortar, and concrete from the standpoint of composition and structure. *Advances in Cement Manufacture and Use, Engineering Foundation*, 271-294, 1989.

[84] T. Nakano, A. Tsuchiyama, K. Uesugi, M. Uesugi and K. Shinohara. SLICE – Software for basic 3-D image analysis [online]. *Japan Synchrotron Radiation Research Institute (JASRI)*, 2006. <http://www-bl20.spring8.or.jp/slice/>

[85] J. Hoshen and R. Kopelman. Percolation and cluster distribution. I. Cluster multiple labeling technique and critical concentration algorithm. *Physical Review B*, 14, 34-38, 1976.

[86] D. Stauffer. Introduction to percolation theory. Taylor & Francis, Philadelphia, PA, USA, 1985.

[87] S. Ikeda, N. Nakano and Y. Nakashima. Three-dimensional study on the interconnection and shape of crystals in a graphic granite by X-ray CT and image analysis. *Mineralogical Megazine*, 64(5), 945-959, 2000.

[88] A. Tsuchiyama, K. Uesugi, T. Nakano and S. Ikeda. Quantitative evaluation of attenuation contrast of X-ray computed tomography images using monochromatized beams. *American Mineralogy*, 90, 132-142, 2005.

[89] E.C McCullough. Photon attenuation in computed tomography. *Medical Physics,* 2, 307-320, 1975.

[90] J.H. Hubbel and S.M. Seltzer. Tables of X-ray mass attenuation coefficient (version 1.4) (online). National Institute of Standard and Technology, Gaitherburg, MD. <http://physic.nist.gov/xaamdi/>

[91] Mineralogy data base. <http://webmineral.com>

[92] D.P Bentz, P.V, Coveney, E.J. Garboczi, M.F Kleyn and P.E. Stutzman. Cellular automaton simulations of cement hydration and microstructure development. *Modell. Simul. Mater. Sci. Eng*, 2, 783-808, 1994.

[93] I.G. Richardson. The calcium silicate hydrates. *Cement and Concrete Research*, 38, 137-158, 2008.

[94] H. Justnes, L. Elfgren and V. Ronin. Mechanism for performance of eneegetically modified cement versus corresponding blended cement. *Cement and Concrete Research*, 35(2), 315-323, 2005.

[95] M. Doube, M.M. Klosowski, I. Argenda-Carreras, F.P. Cordelières, R.P. Dougherty,

J.S. Jackson, B. Schmid, J.R. Hutchinson, and S.J. Shefelbine. BoneJ: Free and extensible bone image analysis in ImageJ. *Bone*, 47, 1076-1079, 2010.

[96]   M. Doube. BoneJ, 2009. < http://bonej.org>

[97]   T. Hildebrand and P. Rűegsegger. A new method for the model-independent assessment of thickness in three-dimensional images. *J Microsc*, 185, 67-75, 1997.

[98]   R. Dougherty, and K. Kunzelmann. Computing local thickness of 3D structures with ImageJ. *MicroscMicroanal*, 13, 1678-9, 2007.

[99]   I. Arganda-Carreras, R. Fernández-Gonzáles, A. Muñoz-Barrutia, and C. Ortiz-De-Solorzano. 3D reconstruction of histological sections: application to mammary gland tissue. *Microsc Res Tech*, 73(11), 1019-1029, 2010.

[100] J.A. Currie. Gaseous diffusion in porous media. Parts1 and 2, Br. *J. Appl. Phys*, 11, 314-324,1960.

[101] H. Takahashi, Y. Seida, and M. Yiu. 3D X-ray CT and diffusion measurements to assess tortuosity and constrictivity in a sedimentary rock. *diffusion-fundamentals.org* 11(89), 1-11, 2009.

[102] Y. Nakashima and S. Kamiya. Mathematica programs for the analysis of three-dimensional pore connectivity and anisotropic tortuosity of porous rocks using X-ray microtomography. *Journal of Nuclear Science and Technology*, 44(9), 1233-1247, 2007.

[103] J. Rho, M. Hobatho and R. Ashman. Relations of mechanical properties to density and CT numbers in human bone. *Medical Engineering & Physics*, Vol.17, 347-355, 1995.

[104] B. Couteau, M. Hobatho, R. Darmana, J. Brignola and J. Arlaud. Finite element modeling of the vibrational behavior of the human femur using CT-based individualized geometrical and material properties. *Journal of Biomechanics*, Vol.31, 383-386, 1998.

[105] J.L Provis, R.J. Myers, C.E. White, V. Rose and J.S.J. van deventer. X-ray microtomography shows pore structure and tortuosity in alkali-activated binders. Cement and Concrete Research, 42, 855-864, 2012.

[106] M. Daimon, S.A.Abo-El-Enein, G. Hosaka, S. Goto and R, Kondo. Pore structure of calcium silicate hydrate in hydrated tricalcium silicate. J. Am. Ceram. Soc, 60(3-4), 110-114, 1977.

[107] W.M. Lin, T.D. Lin, and L.J. Powers-Couche. Microstructures of fire-damaged concrete. *ACI Materials Journal*, 93(3), 199-205, 1996.

[108] R. Sarshar and G.A. Khoury. Material and environmental factors influencing the compressive strength of unsealed cement paste and concrete at high temperatures. *Magazine of Concrete Research*, 45(162), 51-61, 1993.

[109] T. Harada, J. Takeda, S. Yamane and F. Furumura. Strength, elasticity and thermal properties of concrete subjected to elevated temperatures. *In: ACI Special Publication SP-34 Concrete for Nuclear Reactors, Detroit: American Concrete Institute,* 377-406, 1972.

[110] I.G Richardson. The nature of C-S-H in hardened cements. *Cement and Concrete Research*, 29, 1131-1147, 1999.

[111] J.L Garcia Calvo, A. Hidalgo, C. Alonso and L.F. Luco. Development of low-pH cementitious materials for HLRW repositories resistance against ground water aggression. *Cement and Concrete Research*, 40, 1290-1297, 2010.

[112] G. Constantinedes and F.J. Ulm. The effect of two types of C-S-H on the elasticity of cement-based materials: Result from nanoindentation and micromechanical modeling. *Cement and Concrete Research*, 34, 67-80, 2004.

[113] P. Faucon, F. Adenot, R.Cabrilac and M. Jorda. Deterioration mechanism of cement

paste under water attack, concrete under severe condition 2. P*roceeding of Second International Conference on Concrete Under Severe Conditions CONSEC'98*, 1, 123-132, 1998.

[114]   K. Haga, S. Sutou, M. Hironaga, S. Tanaka and S. Nagasaki. Effect of porosity on leaching of Ca from hardened ordinary Portland cement paste. *Cement and Concrete Research*, 35, 1764-1775, 2005.

[115]   T. Hitomi, N. Takeda and K. Iriya. Evaluation of cement hydrate leaching of highly fly ash containing silica fume cement. Proceeding of 4th International Conference on Construction Materials: Performance, Innovations and Structural Implications, S7-3-2, 785-792, 2009.

[116]   F. Adenot and M. Buil. Modelling of the corrosion of the cement paste by deionizedwater, *Cement and Concrete Research*. 22, 489–496, 1992.

[117]   F.P. Glasser and M. Atkins. Cements in radioactive waste disposal, *Mater. Res. Soc*. Bull.12, 33–39, 1994.

[118]   P. Lovera, F. Adenot, M. Jorda and R. Cabrillac. Physico-chemical transformation of sulfated compounds during the leaching of highly sulfated cemented wastes, *Cement and Concrete Research*. 57 (27), 1523–1532, 1997.

[119]   Y.H. Li, and S. Gregory. Diffusion of ions in sea water and in deep-sea sediment. *GeochimicaetCosmochimicaActa*, 38, 703-714, 1974.

[120]   M. Flury and T. Gimmi. Solute diffusion.   In: J.H. Dane, G.C. Topp Eds. Methods of Soil Analysis, Part 4, *Physical Methods, Soil Science Society of America*, Madison, WI, 1323-1351, 2002.

APPENDIX A
3D PORE STRUCTURE OF OPC-CP-50 AND HFSC-CP-50
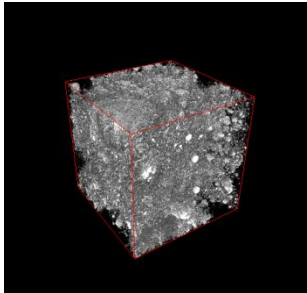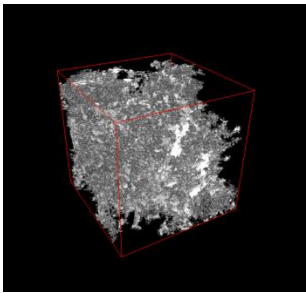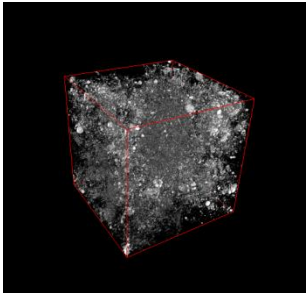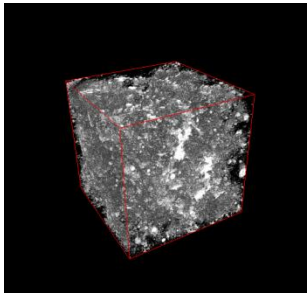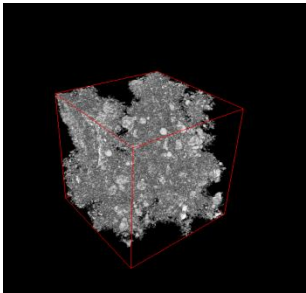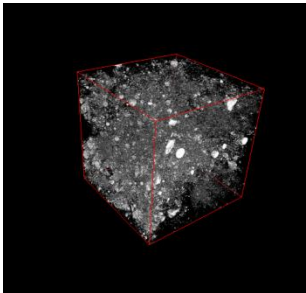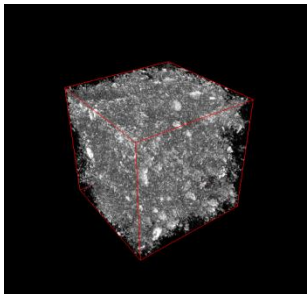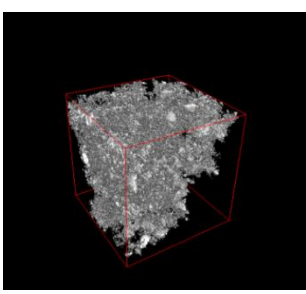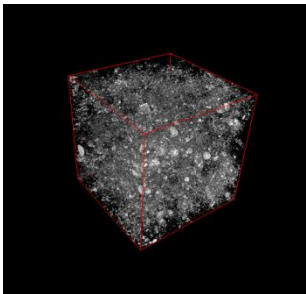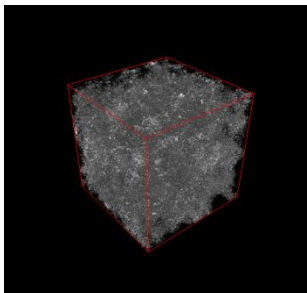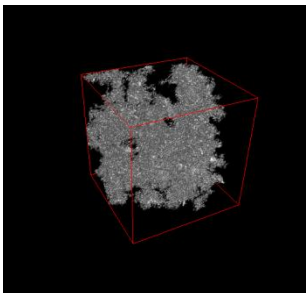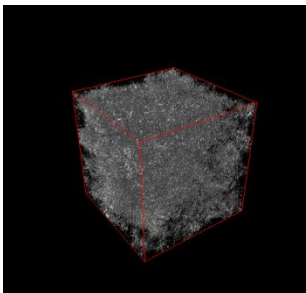
	Segmented Porosity	Percolated Porosity	Isolated Porosity
2 days			
7 days			
28 days			
146 days			

Figure A.1 Visualization of three-dimensional of pore structure from microtomographic images of OPC-CP-50 specimens.
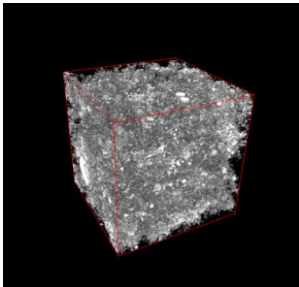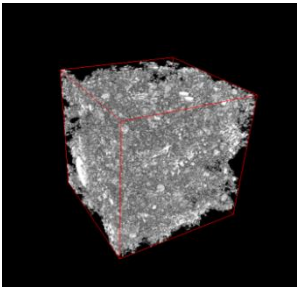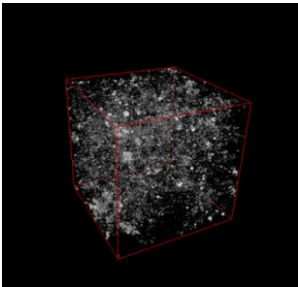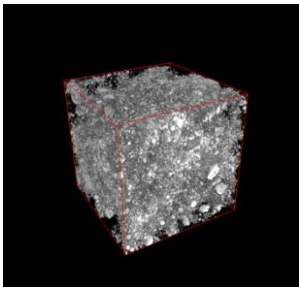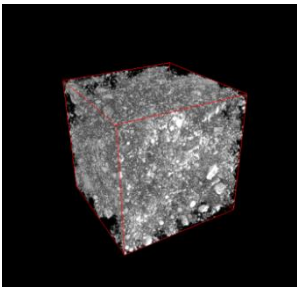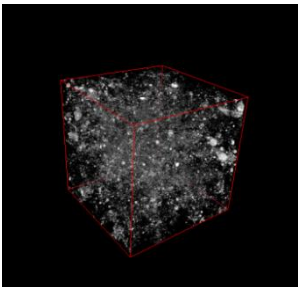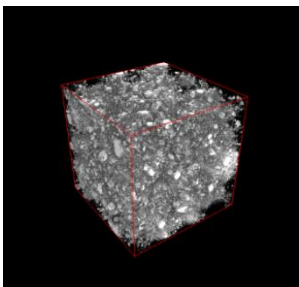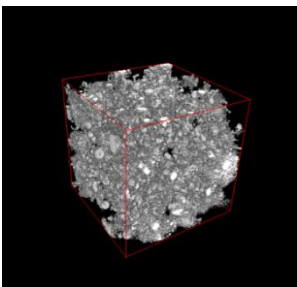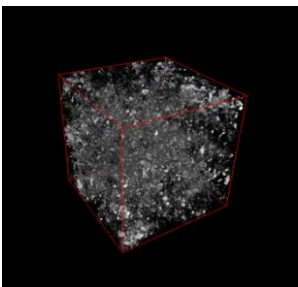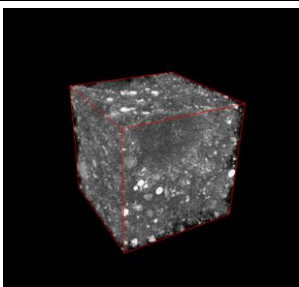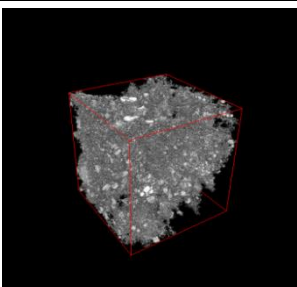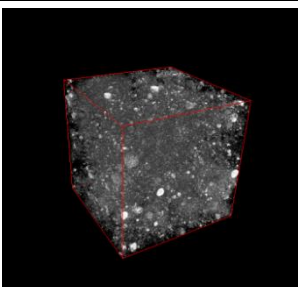
	Segmented Porosity	Percolated Porosity	Isolated Porosity
2 days			
7 days			
28 days			
146 days			

Figure A.2 Visualization of three-dimensional of pore structure from microtomographic images of HFSC-CP-50 specimens.

APPENDIX B
THREE-DIMENSIONAL OF PORE SIZE DISTRIBUTION OF
OPC-CP-50 AND HFSC-CP-50
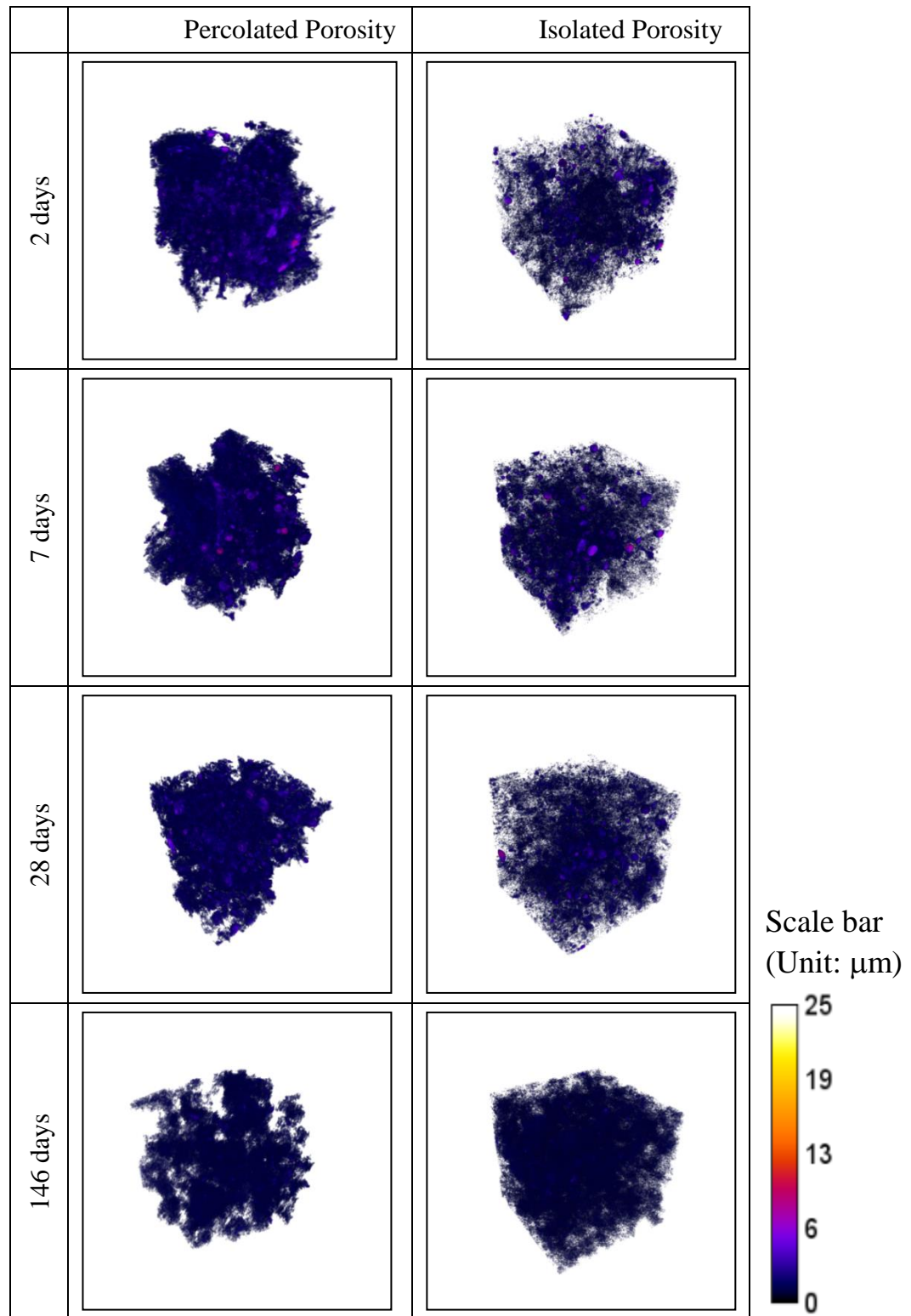
Figure B.1 Visualization of three-dimensional of pore size distribution of OPC-CP-50 specimens.

	Percolated Porosity	Isolated Porosity
2 days		
7 days		
28 days		
146 days		

Scale bar
(Unit: μm)
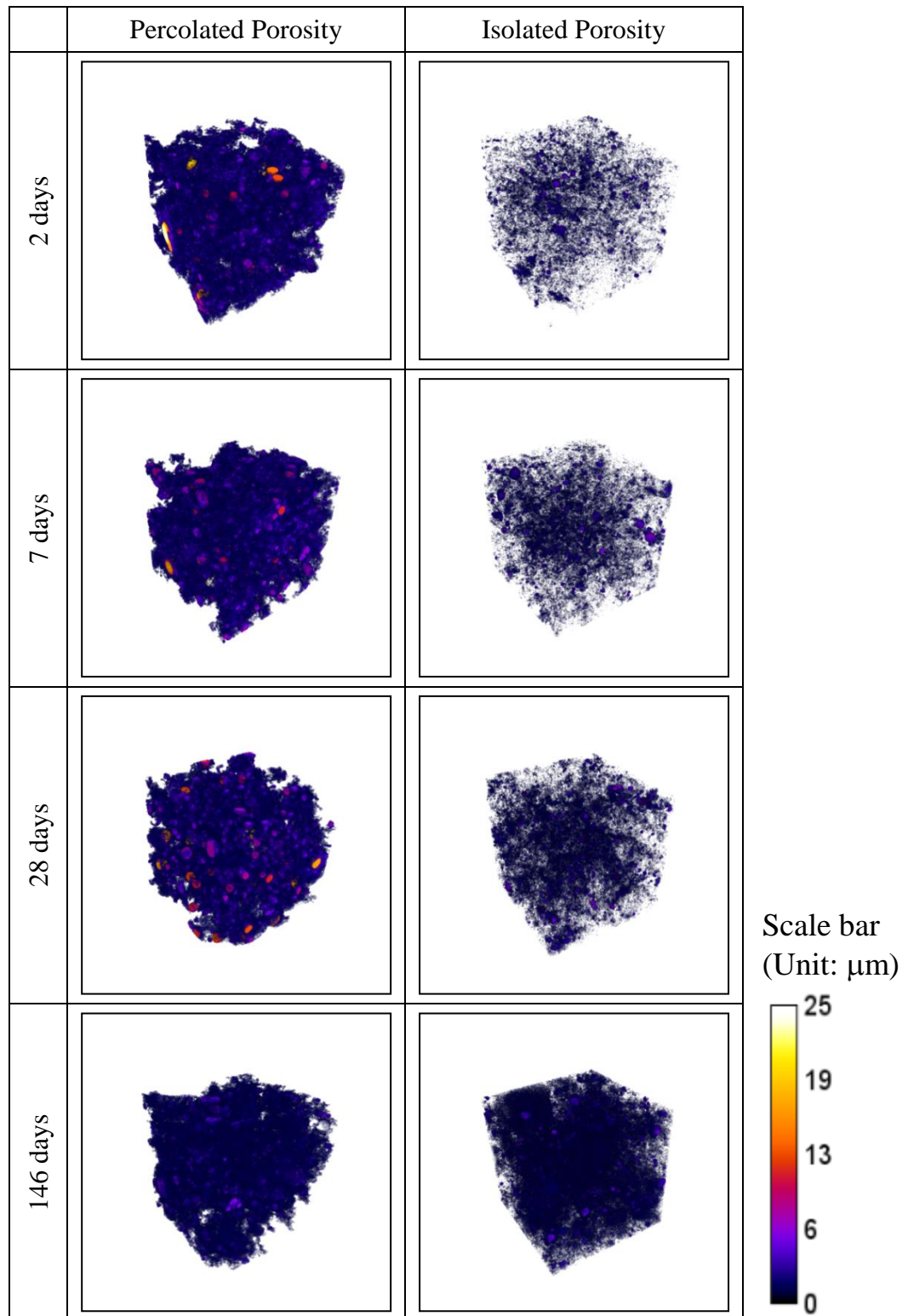
Figure B.2 Visualization of three-dimensional of pore size distribution of HFSC-CP-50 specimens.

APPENDIX C
3D PORE STRUCTURE OF OPC-CP-50 AND HFSC-CP-50
BEFORE AND AFTER LEACHING

Figure C.1 Visualization of 3D pore structure derived from microtomographic images of OPC-CP-50 and HFSC-CP-50 specimen before leaching test (146 days curing periods) and after leaching test for 13 weeks.

APPENDIX D
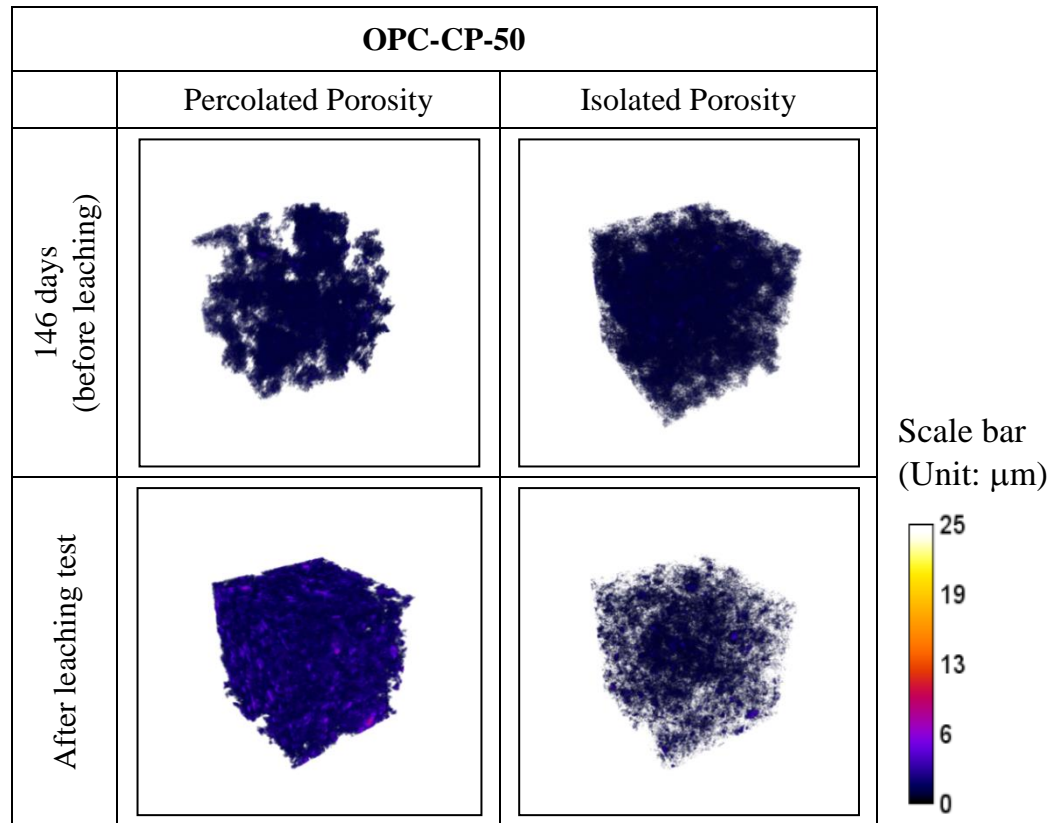# THREE-DIMENSIONAL OF PORE SIZE DISTRIBUTION OF OPC-CP-50 AND HFSC-CP-50 BEFORE AND AFTER LEACHING

Figure D.1 Visualization of three-dimensional of pore size distribution of OPC-CP-50 specimen before and after leaching test.
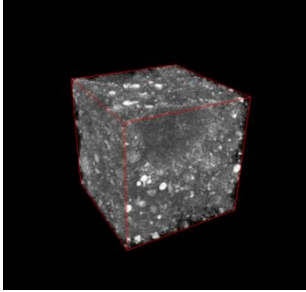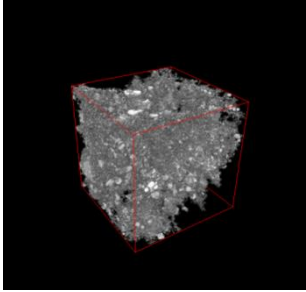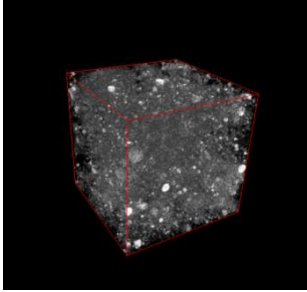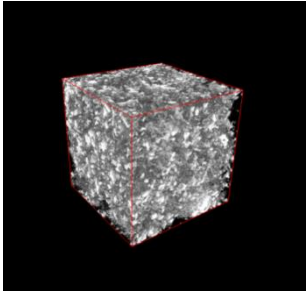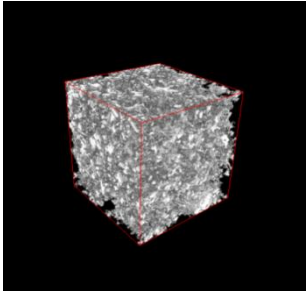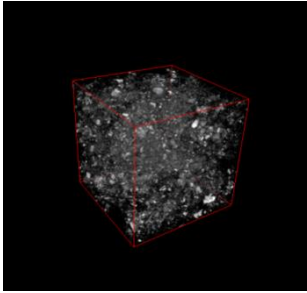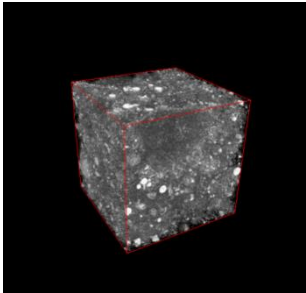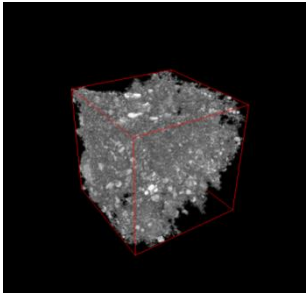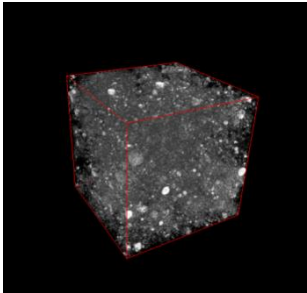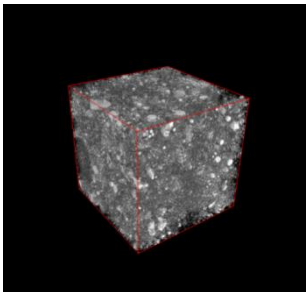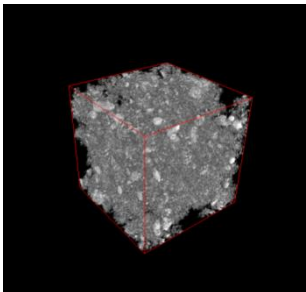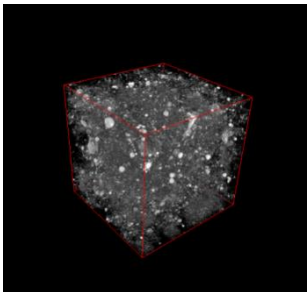
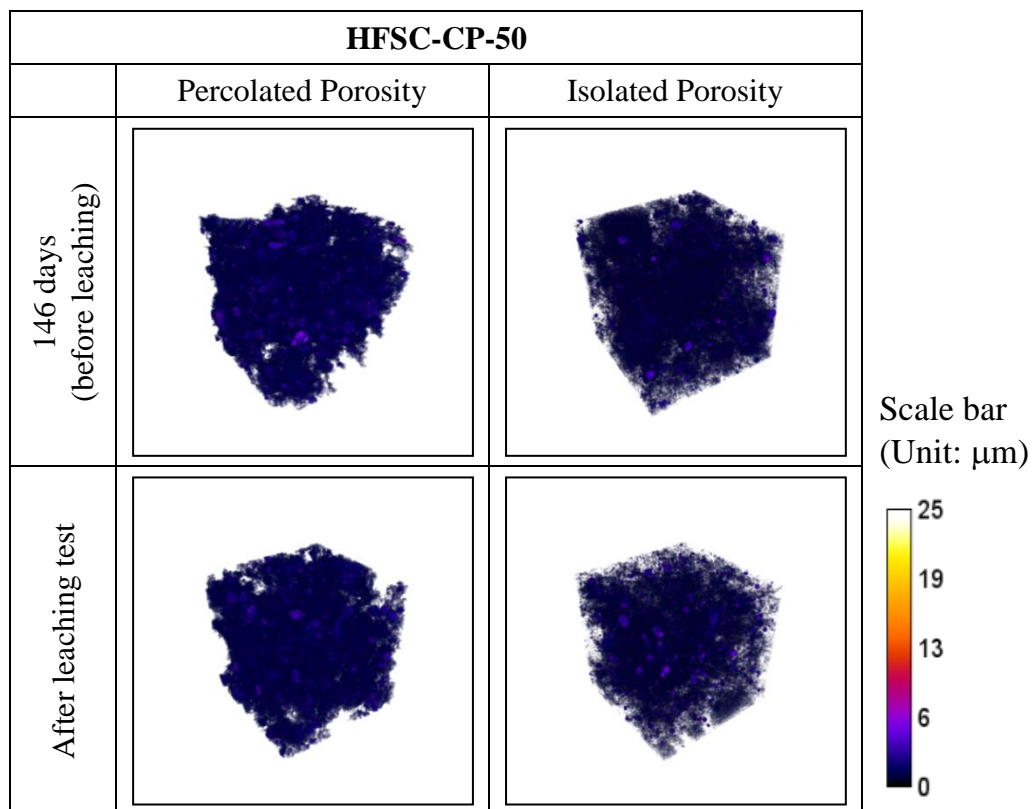| HFSC-CP-50		
	Percolated Porosity	Isolated Porosity
146 days (before leaching)		
After leaching test		

Scale bar (Unit: µm)

25
19
13
6
0

Figure D.2 Visualization of three-dimensional of pore size distribution of HFSC-CP-50 specimen before and after leaching test.